Reference
NBS Publi-cations

NAT'L INST. OF STAND & TECH R.I.C.
A11105 037094

NBSIR 80-1633

A11101 729047

MATERIALS STUDIES FOR SUPERCONDUCTING MACHINERY COIL COMPOSITES

J. W. Ekin
M. B. Kasen
D. T. Read
R. E. Schramm
R. L. Tobler
A. F. Clark

Thermophysical Properties Division
National Engineering Laboratory
National Bureau of Standards
Boulder, Colorado 80303

Prepared for:
Annapolis Laboratory
David W. Taylor Naval Ship Research and
Development Center
Annapolis, Maryland 21402

November 1979
Interim Report

QC
100
.U56
80-1633
1979

QC100
.U56
NO.80-1633
1979

NBSIR 80-1633

MATERIALS STUDIES FOR SUPERCONDUCTING MACHINERY COIL COMPOSITES

J. W. Ekin
M. B. Kasen
D. T. Read
R. E. Schramm
R. L. Tobler
A. F. Clark

Thermophysical Properties Division
National Engineering Laboratory
National Bureau of Standards
Boulder, Colorado 80303

Prepared for:
Annapolis Laboratory
David W. Taylor Naval Ship Research and
Development Center
Annapolis, Maryland 21402

November 1979
Interim Report

U.S. DEPARTMENT OF COMMERCE, Philip M. Klutznick, Secretary

Luther H. Hodges, Jr., Deputy Secretary
Jordan J. Baruch, Assistant Secretary for Productivity, Technology and Innovation

NATIONAL BUREAU OF STANDARDS, Ernest Ambler, Director

TABLE OF CONTENTS

Page

LIST OF TABLES..... v

LIST OF FIGURES..... vi

ABSTRACT..... xi

1. INTRODUCTION..... 1
   1.1 SUMMARY OF PRIOR WORK by A. F. Clark..... 3
   1.2 SUMMARY OF PRESENT WORK by A. F. Clark..... 16
2. MATERIALS FOR SUPPORT STRUCTURES..... 21
   2.1 FIBERGLASS EPOXY IN A CONICAL SUPERCONDUCTING MOTOR SUPPORT by R. E. Schramm and M. B. Kasen..... 21
   2.2 FATIGUE RESISTANCE OF A UNIAXIAL S-GLASS EPOXY COMPOSITE by R. L. Tobler and D. T. Read..... 34
3. COMPOSITE COIL MATERIALS..... 55
   3.1 EFFECT OF STRAIN ON EPOXY-IMPREGNATED SUPERCONDUCTING COMPOSITES by J. W. Ekin, R. E. Schramm, and A. F. Clark..... 55
   3.2 YOUNG'S MODULI OF COMPOSITE COIL MATERIALS by D. T. Read and A. F. Clark..... 67
4. CONDUCTORS..... 71
   4.1 LOW TEMPERATURE TENSILE BEHAVIOR OF COPPER-STABILIZED NIOBIUM-TITANIUM SUPERCONDUCTING WIRE by R. P. Reed, R. P. Mikesell, and A. F. Clark..... 71
   4.2 EFFECT OF STRAIN ON THE CRITICAL CURRENT OF COPPER-STABILIZED AND ALUMINUM-STABILIZED NbTi MULTIFILAMENTARY COMPOSITES by J. W. Ekin..... 89
   4.3 MECHANISMS FOR CRITICAL-CURRENT DEGRADATION IN NbTi AND Nb_3Sn MULTIFILAMENTARY WIRES by J. W. Ekin..... 116

Appendices

Page

A1 Current Transfer in Multifilamentary Superconductors..... 131

I. Theory by J. W. Ekin

A2 Current Transfer in Multifilamentary Superconductors..... 135

II. Experimental Results by J. W. Ekin, A. F. Clark, and J. C. Ho.

A3 Defining Critical Current by A. F. Clark and J. W. Ekin..... 138

A4 Orthorhombic Elastic Constants of an NbTi/Cu Composite Superconductor by H. M. Ledbetter and D. T. Read..... 141

A5 Temperature Dependence of the Elastic Constants of an NbTi/Cu Superconducting Composites by D. T. Read and H. M. Ledbetter..... 147

LIST OF TABLES

		Page
1-1-1	Comparison of Static and Acoustic Measurements of Elastic Moduli	5
2-1-1	Mechanical Property Data Summary	25
2-2-1	Static Tensile Properties of S-901 Glass/Epoxy Specimens	40
2-2-2a	Fatigue Results for S-901 Glass/Epoxy at 295 K	45
2-2-2b	Fatigue Results for S-901 Glass/Epoxy at 4 K	46
3-1-1	Epoxy Properties	58
3-2-1	Acoustic Modulus Specimen Characterizations	68
4-2-1	Sample Characteristics	95

LIST OF FIGURES

		Page
1-1-1	Young's moduli of coil materials as a function of temperature for different directions.	7
1-1-2	Shear modulus versus temperature as measured acoustically in the superconducting coil composite.	7
1-1-3	Tensile properties of the Nb-Ti filaments, the superconducting wire composite, and copper wire.	10
1-1-4	Thermal conductivity of the superconducting coil composite materials.	10
1-1-5	Thermal contraction of the superconducting coil composite materials.	12
1-1-6	Thermal contraction of the Cu/Nb-Ti superconducting wire and its constituents.	12
1-1-7	Specific heat of the superconducting coil composite materials.	14
1-1-8	Cumulative circumferential stresses in the superconducting wire for constant and programmed winding tension.	14
2-1-1	Fixture for measurement of cone stiffness as a function of axial compressive force. Strain gages were bonded directly to the cone surface.	23
2-1-2	Porosity lying on the interlaminar shear planes of 10 ply NASA Resin 2 and E 787 composites tested in this program. Transmitted light. a) 1581 S-glass/NASA Resin 2; b) 1581 S-glass/E-787 (Lot 1); c) 1581 S-glass/E-787 (Lot 2).	27
2-1-3	Deflection of the Resin 2 cone as a function of axial compressive force. Calculated stiffnesses are noted.	29
2-1-4	Localized strain variations in the Resin 2 cone as a function of axial compressive force. Numbers refer to strain gages positioned as illustrated on Figure 2-1-1.	30
2-2-1	S-901 glass/epoxy test specimen.	36
2-2-2	Liquid helium fatigue cryostat.	37
2-2-3a	Static test records; ordinary failure.	41
2-2-3b	Static test records; premature failure.	42
2-2-4	Room temperature fatigue data, with stresses normalized to the static strength, showing the agreement between present results and those of Reference [5].	44

Page

2-2-5 4 K fatigue results, demonstrating a superior low temperature fatigue resistance, as compared to room temperature results. 47

2-2-6 Tensile (lower) and fatigue (upper) failures of specimens tested at 4 K. 49

2-2-7 Deflection-versus-cycles for specimens tested at 295 K, showing the increase in compliance preceding failure 51

3-1-1 Cross-sectional view of a superconducting composite ring showing its components. 60

3-1-2 Schematic of the ring test setup showing the configuration of force, F, applied to the D's, current I, applied to the superconducting ring, and the resulting self-field B, calculated to be about 3 T at maximum current 61

3-1-3 Training behavior of each ring type as a function of applied strain. 63

3-1-4 Critical-current degradation of each ring type as a function of applied strain. 65

4-1-1 Photomicrograph of the multifilamentary superconducting wire containing 180 filaments and a copper to conductor (Nb-Ti) ratio of 1.8 to 1.0. 74

4-1-2 Loading assembly for the wire specimens 77

4-1-3 Tensile and yield strengths as a function of temperature. Yield strength for Nb-Ti twisted filaments was unobtainable due to their small amount of plastic deformation ($0.689 - 10^4$ psi = N/m^2). 81

4-1-4 Stress-strain curves at 298, 76, and 4 K (0.689×10^4 psi = N/m^2). 82

4-1-5 The effect of strain rate on tensile properties. All data were obtained at 4 K. Brackets represent spread of data presented in Fig. 4-1-4 85

4-1-6 Anelastic recovery of multifilamentary superconducting wire as a function of maximum applied stress. 86

4-2-1 Schematic diagram of the stress-I_c apparatus for testing hairpin samples 91

4-2-2 Schematic diagram of the strain-I_c apparatus for testing straight samples. 93

Page

4-2-3a Crossectional view of sample 1 (NSRDC 4-2, NbTi:Cu = 1:1.8)..... 96

4-2-3b Crossectional view of sample 3..... 96

4-2-4 Voltage-current characteristics for NbTi multifilamentary wire (sample 1) as a function of stress and strain. Also shown are 3 dashed lines corresponding to several critical-current criteria: an electric field along the wire of 3 μV/cm, and resistivities of 10^{-10} and 10^{-11} Ωcm, normalized to the cross sectional area of NbTi in the conductor..... 97

4-2-5 Critical current as a function of stress at various applied magnetic fields. Solid curves correspond to the critical current measured while the wire is under stress; dashed curves represent the critical current measured after load is applied and reduced to the prestress value. (Sample 1)..... 99

4-2-6 Critical current as a function of stress at various applied magnetic fields. Solid curves correspond to the critical current measured while the wire is under stress; dashed curves represent the critical current measured after load is applied and reduced to the prestress value. (Sample 2)..... 100

4-2-7 Critical current as a function of stress at various applied magnetic fields. Solid curves correspond to the critical current measured while the wire is under stress; dashed curves represent the critical current measured after load is applied and reduced to the prestress value. (Sample 3)..... 101

4-2-8 Critical-current degradation in several multifilamentary NbTi:Cu composites (samples 1, 4, and 5) as a function of strain. Critical current, I_c, is expressed as a fraction of the initial unstrained critical current, I_{co}..... 103

4-2-9 Critical-current degradation in a multifilamentary NbTi:Cu composite (sample 1) as a function of strain at three applied magnetic fields. Critical current, I_c, is expressed as a function of the initial unstrained critical current, I_{co}..... 104

4-2-10 Critical current vs. magnetic field at various applied stress levels..... 105

4-2-11a Crossectional view of sample 4..... 107

4-2-11b Crossectional view of sample 5..... 107

Page

4-2-12 Crossectional view of sample 6..... 108

4-2-13 Crossectional view of sample 7..... 109

4-2-14 Voltage-current characteristics for sample 4, at several values of magnetic field. Characteristics labeled by upward-pointing arrows indicate the field was increased to the value shown; downward-pointing arrows indicate the field was decreased to the value shown..... 111

4-2-15 Comparison of critical current vs. strain characteristics for aluminum- and copper-stabilized NbTi superconductors (samples 4 and 5)..... 112

4-3-1 Summary of critical current degradation in multifilamentary NbTi and Nb_3Sn wires. Results were obtained at comparable magnetic fields (0.45 H_{c2}) for the two materials. Dashed lines for each case indicate the critical-current recovery value after unloading..... 118

4-3-2 Time invariance of the critical-current degradation. Voltage-current plot shows the extent of degradation in a NbTi wire at a stress of 8×10^8 Pa. Voltage-time insert indicates the constancy of the flux-flow voltage during the 2 hour test when the wire was biased at a current of 208 A..... 121

4-3-3 Invariance of the critical current degradation with residual resistivity ratio (RRR) of the matrix. Under stress, the RRR for the Cu-stabilizer decreased to 19, while RRR for the Al-stabilizer decreased to 191. The stabilization material for each conductor was contained within NbTi tubes (69 μm O.D., 39 μm I.D.) embedded in a 5056 aluminum alloy matrix..... 123

4-3-4 Magnetic-field dependence of the critical-current degradation. Voltage-current insert shows the large resistivity (10^{-7} Ω cm) of a highly strained superconductor at high magnetic fields, compared with the very low resistivity ($<10^{-13}$ Ω cm) of the same wire at zero applied field. Dashed lines show the retrace curves as the wire returned to the superconducting state after being driven normal..... 124

Material Studies for Superconducting Machinery Coil Composites

J. W. Ekin, M. B. Kasen, D. T. Read, R. E. Schramm,
R. L. Tobler, and A. F. Clark

The physical properties of a superconducting coil composite are studied to accurately predict the coil behavior under operating conditions. Emphasized in this third interim report are studies on the effect of stress and strain on the critical current of superconducting wires. The report also includes data on several fiberglass/epoxy support structures for the coil and its dewar. Preliminary results are also given for the effect of stress on small superconducting composite rings used to model the full sized coil behavior. A summary of the program results to date is included.

Keywords: Critical current; fiberglass/epoxy composite; mechanical properties; niobium-tin; niobium-titanium; strain; superconducting coil composite; superconducting wire.

1. INTRODUCTION

The distinct advantages of lighter weight, smaller size, and higher magnetic fields for superconducting magnets have led to their successful application in electrical motors and generators. This superconducting electrical machinery, especially for propulsion applications, must operate in a variety of conditions. The objective of the research reported here is to determine the physical and mechanical properties of such a magnetic field coil and the effect of operating environments on its superconducting behavior. Thus, not only must the properties of the coil components be known and understood, but their interaction with the stress and magnetic field environments as well. With this understanding will come the ability to predict the operating behavior of the superconducting coil and the assurance to design for long term reliability.

This report is the third in a series of interim reports summarizing the research which has principally been published in the open literature. The first report[1*] presented some of the mechanical properties and the thermal expansion of the coil structure and established the micromechanical constitutive relationships for comparison with constituent properties. The second report[2] completed most of the mechanical and thermal properties of the coil material and compared them with values predicted from its constituent properties. The properties measured included Young's modulus, Poisson's ratio, shear modulus, tensile strength, elastic constants, thermal conductivity, thermal expansion, and specific heat. The report also included a stress analysis for a transversely isotropic coil for the stresses induced by fabrication, cool-down, and the magnetic field.

*References are numbered independently in each section.

This third report includes: a summary of past and present work (Sec. 1); reports on two different structures for dewar support, fiberglass epoxy bands and cones (Sec. 2); some preliminary data on a small coil simulation for testing coil materials under stress and in a magnetic field (Sec. 3); the mechanical properties of NbTi superconducting wires and the effect of stress, strain, and magnetic field on the critical current in these conductors (Sec. 4); and, as appendices, some related publications on superconductors which were direct outgrowths of sponsored work. A fourth report is in preparation and will include strain effect studies on Nb_3Sn and other developmental superconductors, fatigue effects in conductors, and scaling laws for these effects on the critical properties.

New work is in progress in two principle areas: 1) further studies on the effects of strain, fatigue, magnetic field, and temperature on the critical behavior of wires, both those used in present electrical machinery and developmental wires, and 2) a complete study of the superconducting composite ring (SCCR) as a simulation of the electrical machinery environment (stress and field) on the superconducting behavior of various different combinations of wires and epoxies for the coil material.

1.1 SUMMARY OF PRIOR WORK

by A. F. Clark

The superconducting coil composite is not a simple structure. It contains solenoidal layers of superconducting wires (which are composites themselves) separated by layers of fiberglass cloth, the whole of which is potted in an epoxy. It is highly anisotropic and is subject to highly anisotropic thermal, magnetic, and mechanical stresses. Just how anisotropic and the basic property values can best be described by a brief summary of the properties measurement program to date. A specific coil description and a table of all the coil and constituent properties measured is in the second report[2] and a progress report at the 6th International Conference on Magnet Technology.[3] For this discussion the coil composite is assumed to be transversely isotropic with the longitudinal, 1, direction along the wires, the radial, 2, direction perpendicular to the wires and glass cloth, and the axial, 3, direction perpendicular to the wires in the plane of the glass cloth.

1.1.1 Mechanical Properties

Several of the mechanical properties of the coil composite and a similarly constituted fiberglass epoxy were measured: the Young's modulus in all three principal directions, two shear moduli, several Poisson's ratios, some acoustic measurements of the same properties, and the tensile properties of the superconducting wire.

Young's Moduli. The specimen preparation and experimental arrangement are described in the first report.[1] Briefly, the specimens were machined from actual coil material, strain gauges applied, and measurements performed at the three temperatures, 293, 76 and 4 K, in a normal low temperature tensile arrangement.

Because of the relatively weak fracture properties of the epoxy bond between wires, the load for the axial specimen was limited to

$\sim$7.0 MN/m^2 ($\sim$1000 psi). The resultant strains were quite small and yielded an estimated uncertainty of about 5%. The data for all of the Young's moduli are tabulated in Table 1-1-1 and Young's moduli are shown in Fig. 1-1-1.

The Young's moduli all increase slightly with decreasing temperature with the longitudinal specimens having a higher modulus more appropriate to that of the wire. The behavior of the axial Young's modulus, E_{33}, is, as expected, very similar to that of the radial specimen, E_{22} and is probably due almost entirely to the epoxy. The less accurate Poisson's ratios also show a slight increase with decreasing temperature,[1] however the acoustic measurements described below show a decrease.[4]

Acoustic Measurements. Composite materials are usually highly anisotropic and the determination of their elastic constants is much more difficult than for the more usual quasi-isotropic engineering materials. Conventional methods of measuring the elastic properties of solids have been applied to composites with only limited success because these methods usually require relatively large specimens and considerable time and effort. The new application[4] of an acoustic resonance technique to this superconducting coil composite has permitted rapid determination of the coil's elastic constants. It also has the advantage of giving data continuous with temperature.

The technique consists of bonding quartz-driver and quartz-guage piezoelectric crystals to a specimen to produce and to detect a standing longitudinal (or torsional) wave. Each component's length is adjusted so that it's resonant frequency is closely matched to that of the other components. The elastic constants and thus the moduli are obtained from

Table 1-1-1. Comparison of static and acoustic measurements of elastic moduli.

Elastic Moduli (10^{10} N/m^2)		Temperature (K)		
		293	76	4
E_{11}	acoustic	8.14	8.77	8.96
	static	7.58	8.08	8.53
E_{22}	acoustic	3.14	4.07	4.17
	static	2.76	3.79	4.12
G_{13}	acoustic	0.76	1.09	1.12
	static	0.74	1.16	1.22
$E_{\text{fiberglass-epoxy}}$	acoustic	3.14	3.47	3.42
	static	2.80	3.33	3.56

the resonant frequency (about 60 kHz) and the length and density of the specimen.

An example of the continuous and accurate data for one of the shear moduli is shown in Fig. 1-1-2. A comparison of the static and acoustic data for several of the moduli is shown in Table 1-1-1. (The static shear moduli were obtained by a torsional technique.[2]) The comparison is very favorable and well within the large quoted accuracies for the static data. The acoustic resonance technique should prove quite useful.

Mechanical Properties of the Superconducting Wire. The tensile properties of the multifilamentary superconducting wire and its base components, Cu and Nb-Ti, were measured at 298, 76 and 4 K.[5] Conventional tensile properties yield strength, tensile strength, elongation and Young's modulus were obtained. Additionally, the influence of strain rate on tensile behavior and the stress-strain hysteresis effects of the superconducting wire were studied.

The Young's moduli of the wires were found to be lower than the bulk values but were predictable from those values for copper and NbTi using a law of mixtures. The tensile properties of the twisted Nb-Ti filaments, the drawn copper wire, and the superconducting wire composite are summarized in Fig. 1-1-3. The tensile and yield strengths (0.2% offset) have no abnormalities as a function of temperature. The yield strength of Nb-Ti could not be determined since the filaments did not deform plastically 0.2%. Predicted values of the composite tensile strength, based on the mixture law, fall about 25% below the actual composite values; this discrepancy is thought to result from the harder

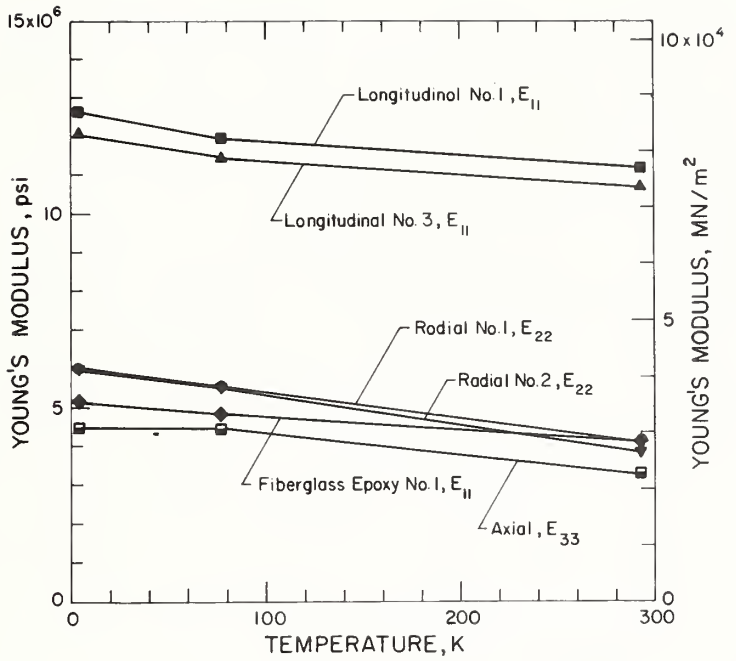

Fig. 1-1-1 Young's moduli of coil materials as a function of temperature for different directions.

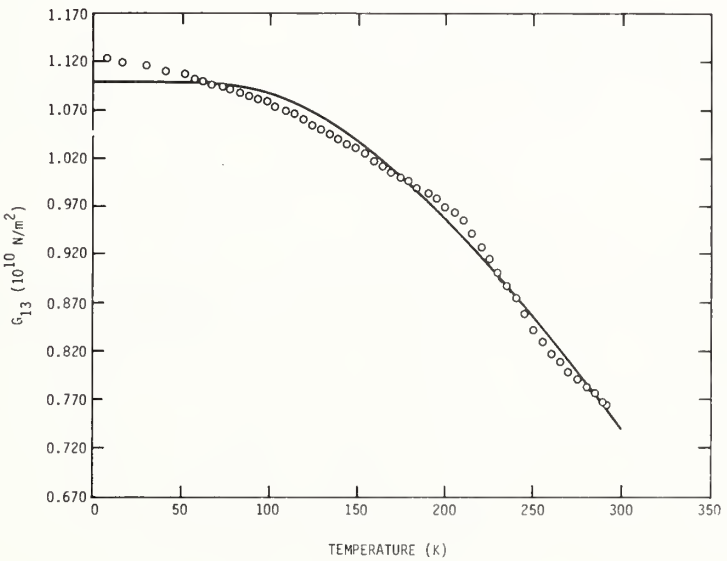

Fig. 1-1-2 Shear modulus versus temperature as measured acoustically in the superconducting coil composite.

condition of the copper in the composite, compared to the copper wire. This harder condition may have resulted from cold working in manufacture and is indicated by hardness and residual resistivity measurements. There is little dependence of the yield strength of the wire composite on temperature.

Compressibility of Glass Cloth. The compressibility of the glass cloth which separates succeeding magnet layers is an important factor in the stress analysis for determining internal magnet stresses. A brief literature survey disclosed no information on this topic so room temperature compressive modulus tests on the glass cloth were performed.[2]

1.1.2 Thermal Properties

The thermal conductivity and thermal expansion of the composite coil material and the thermal expansion of one of its constituents, the Cu-NbTi superconducting wire were measured. The thermal conductivity is highly anisotropic, and contributes significantly to coil stresses. The thermal expansion of the coil composite and the wire behave more or less as expected. The specific heat is also reported for the low temperature region.

Thermal Conductivity of the Coil Composite. Thermal conductivity measurements were performed on longitudinal and transverse sections of the superconducting coil composite.[6] The longitudinal specimen was measured in direction 1, and the transverse specimen was measured in direction 2 (radial). No measurements were performed in the transverse-axial direction but the thermal conductivity in this direction was calculated.

The results of the measurements on the longitudinal and transverse coil composite specimens are given in Fig. 1-1-4. The interpolated curve given for the longitudinal specimen in Fig. 1-1-4 is based on the typical temperature dependence of OFHC copper. The measured data were compared to values calculated from the properties of the constituents of the coil by summing the area-weighted conductivities of each of the parts. Because of the reasonable agreement obtained it was useful to estimate values for the transverse-axial case by the same technique. These values are also shown in Fig. 1-1-4.

The thermal conductivity is the most highly anisotropic of all the properties measured on the coil composite, the longitudinal value being a factor of about 1000 times greater than the poorest conducting transverse value in the radial direction. Even the axial and radial thermal conductivities differ by a factor of 10. These differences are not unexpected because of the high thermal conductivity of copper compared to epoxy and the obvious anisotropy in conducting paths. These differences will be of no consequence in steady state operation but will have a significant effect on any transient behavior such as cooldown or the propagation of a normal conducting zone in the wire.

Thermal Expansion of the Coil Composite. The thermal expansion of several radial and longitudinal specimens as well as one of the fiberglass-epoxy were measured with a quartz tube dilatometer.[1] The results are shown in Fig. 1-1-5. The radial specimens have nearly twice the total thermal contraction to 4 K as both the longitudinal and fiberglass epoxy specimens. This is consistent with the large known thermal contraction of pure epoxy. The approximate equality of the contractions of the longitudinal and fiberglass specimens shows that the fiberglass,

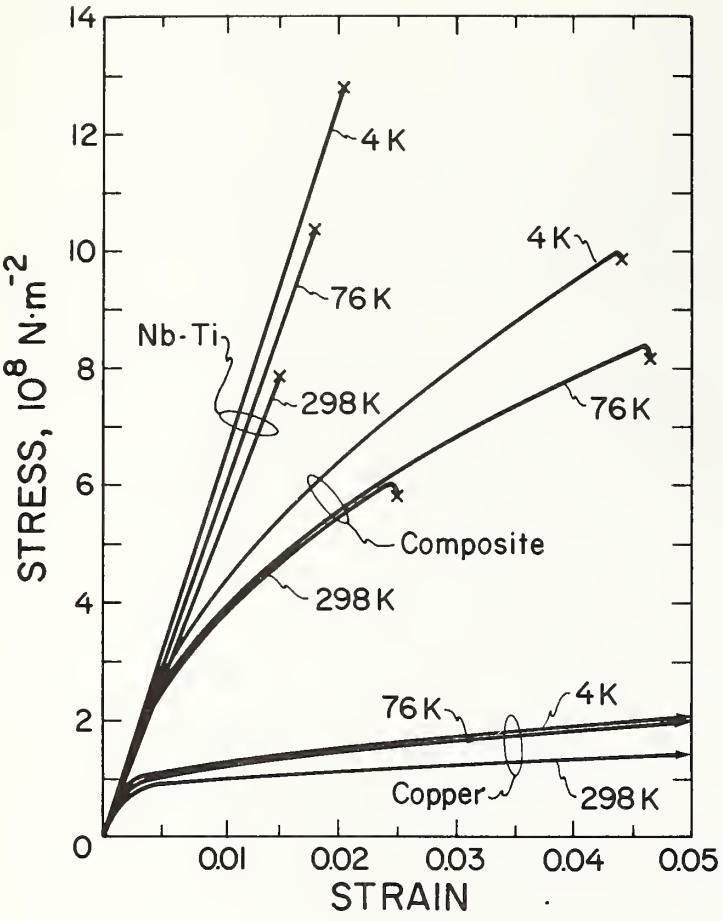

Fig. 1-1-3 Tensile properties of the NbTi filaments, the superconducting wire composite, and copper wire.

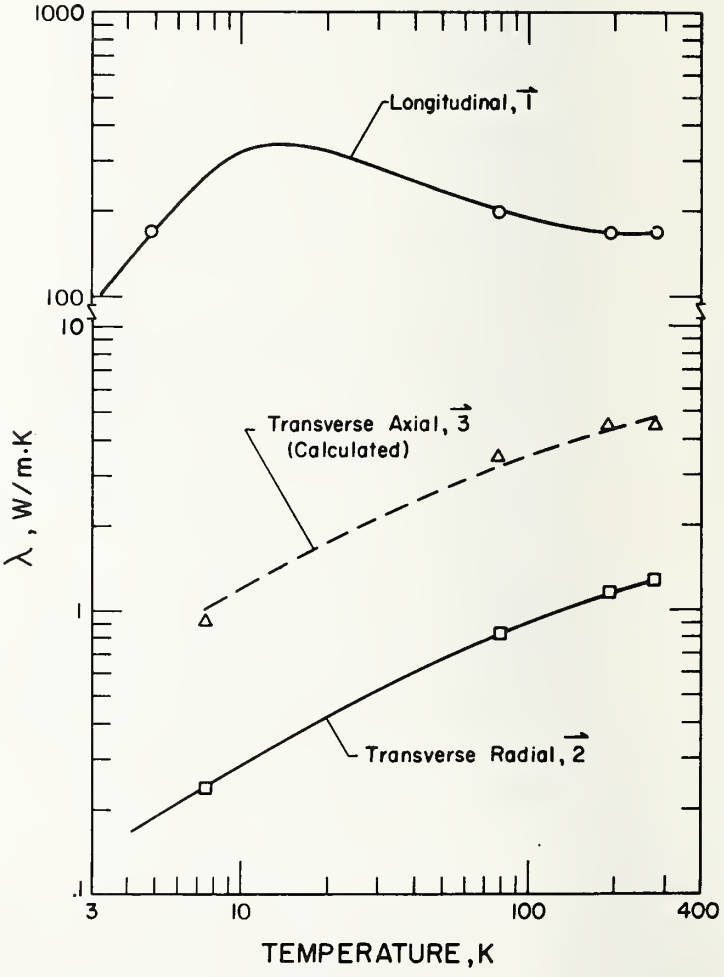

Fig. 1-1-4 Thermal conductivity of the superconducting coil composite materials.

which is in both, inhibits the contraction of the epoxy and dominates the composite behavior.

Thermal Expansion of the Superconducting Wire. The superconducting wire properties are essential components of the composite analysis and thermal contraction of the wire during cooldown is one of the major sources of stress. Toward this end the low-temperature thermal expansion of the Cu-NbTi wire was measured using the quartz tube dilatometer from room temperature to 4 K. The results can be compared with previous measurements of the coil composite[1] and with measurements of the constituents of the wire in Fig. 1-1-6. The thermal expansion curve of the coil composite in the direction parallel to the wires is shown also in Fig. 1-1-6 and is just slightly larger than that of the wires. This would be expected since the coil expansion should be dominated by the wires but slightly enlarged by the weaker epoxy whose thermal expansion coefficient is significantly larger.

Specific Heat of the Coil Composite and Fiberglass Epoxy. The specific heat at low temperatures was measured for both the superconducting coil composite and the fiberglass-epoxy composite.[7] Both specimens were portions of the same material used for the thermal expansion measurements. The measurements were taken by adiabatic calorimetry and only from 4 K to about 25 K, and either further measurements or extrapolations will be done to extend the data to room temperature. The results are shown in Fig. 1-1-7. One can readily see the similar behavior except for the small discontinuity in the coil composite due to the superconducting-to-normal transition of the superconductor. This discontinuity reveals a broad critical temperature transition centered about 9.3 K. That the transition is several tenths of a degree wide

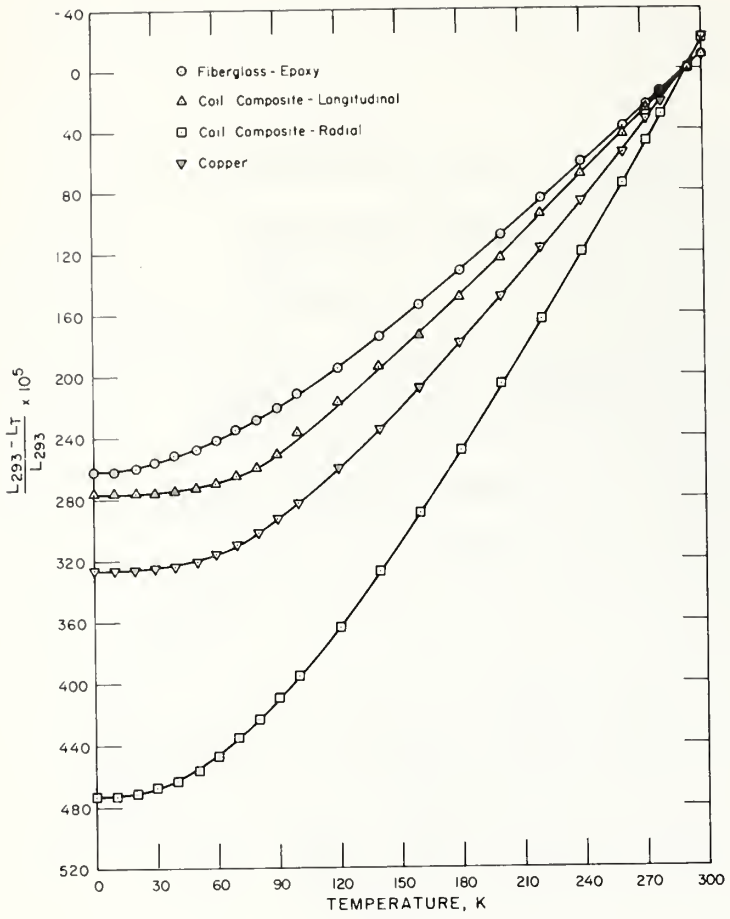

Fig. 1-1-5

Thermal contraction of the superconducting coil composite materials.

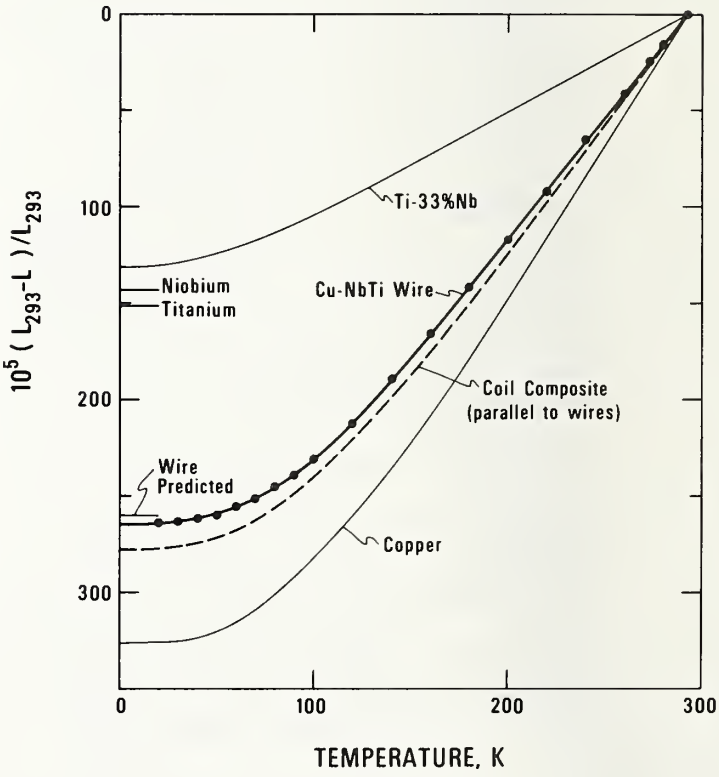

Fig. 1-1-6 Thermal contraction of the Cu/Nb-Ti superconducting wire and its constituents.

implies that there are regions of different T_c due to cold working or diffusion of the superconductor itself. The presence of a dominant quadratic term in a polynomial fit of the data indicates the presence of two-dimensional, rather than three-dimensional, arrays of atomic oscillators. Whether the two dimensionality is due to the long, chain-like polymer molecules or to the reinforcement by the fiberglass is uncertain and could be the subject of further study.

1.1.3 Stress Analysis of Transversely Isotropic Magnet Coils

A simple, two dimensional analytical model was developed[8] to evaluate the stresses generated for the characterized coil when in use. The model assumes cylindrical symmetry for the coil and a transverse isotropy in the coil composite in order to make the calculation viable without going to a long, finite element, three dimensional calculation. The material properties used were those generated in the complete study. Material properties calculated using composite techniques proved to be quite accurate for values not actually measured.[2] The stresses accounted for included those due to (1) winding tension, (2) removal of the support bobbin after epoxy impregnation, (3) cooldown to 4 K, and (4) activation of the magnetic field.

Typical results for one of the calculations of stresses along the wire as a function of radius is shown in Fig. 1-1-8. The effects of the four sources of stress are readily observable, and it also shows that programming the winding tension can result in a much more uniform final stress distribution. Other parameterization also graphically demonstrated the importance of anisotropic moduli, anisotropic contraction, the stiffness of the winding bobbin, the compressibility of the glass cloth, the role of external support, and several others, all of which can be optimized.

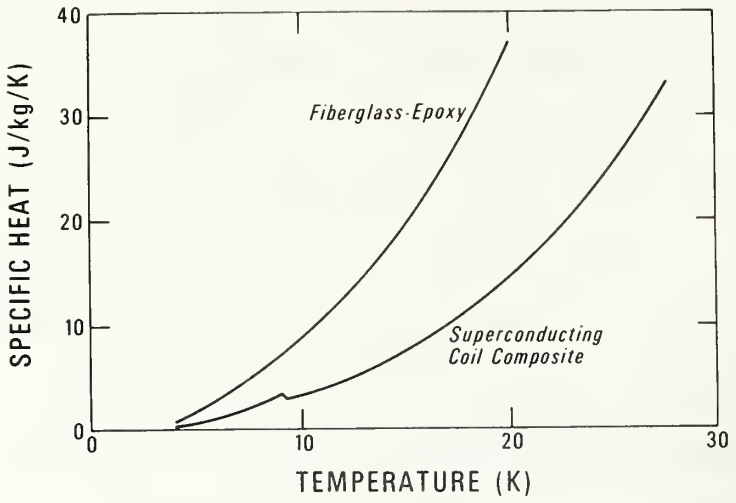

Fig. 1-1-7 Specific heat of the superconducting coil composite materials.

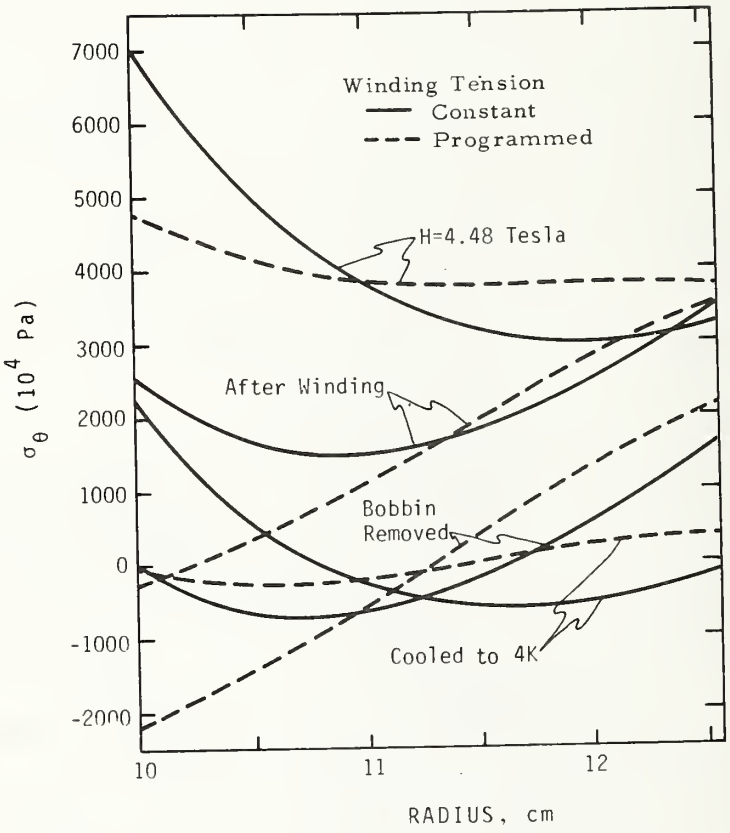

Fig. 1-1-8 Cumulative circumferential stresses in the superconducting wire for constant and programmed winding tension.

1.1.4 Comparison with Predicted Values

Finally, the coil properties as measured were compared with predicted values from the properties of the constituents. In most cases the predicted values were well within 10%, with the exception of the shear related moduli. Thus, a set of constitutive relationships was generated for the coil material and should be reliably predictable for any changes of a component.

1.2 SUMMARY OF PRESENT WORK

by A. F. Clark

The research covered in this third report is varied and complex. Only a brief summary is given here because the details and results are given later. The work is divided roughly into three categories. In section 2 the results of studies on dewar support structures is given, in section 3 some preliminary work on composite coil materials in the form of the superconducting composite rings is reported, and in section 4, the research on a variety of niobium-titanium conductors is presented. The appendices also include several reprints of related work which were direct outgrowths of sponsored work.

1.2.1 Support Structures

Fiberglass-epoxy cones, designed as a thermal standoff and mechanical support at either end of the rotor in the 2.2 MW (3000 hp) superconducting motor, were made of type 1581 S-glass cloth/NASA Resin 2. While in operation, the cones experience a temperature gradient from room temperature to 4 K, but shipping and storage temperatures may reach 350 K. Accordingly, tensile, compressive, and interlaminar shear properties were measured on flat sheets of the glass cloth/Resin 2 composite at 350, 295, 76, and 4 K. For comparison, similar tests were performed on a composite of the same cloth in E-787 epoxy resin. Mechanically, the composite made with flexibilized NASA Resin 2 seriously degrades above room temperature. Furthermore, low shear strengths resulted from voids on the interlaminar planes of both composite types. Comparison confirms greatly differing values obtained with guillotine and short-beam methods. Also tested was a full scale support cone for axial stiffness under compressive loading at 350, 295, and 76 K.

Similarly, filament wound-epoxy bands are used as support structures in the 2.2 MW generator. Tensile strength is not as much a concern as fatigue in these materials. Accordingly, tension-tension axial fatigue tests of a uniaxial glass filament-reinforced epoxy were conducted at 295 K and 4 K. The fatigue life was found to be an order of magnitude greater at 4 K than at 295 K. These results are believed to be the first 4 K fatigue data reported for a composite material.

1.2.2 Composite Coil Materials

Mechanical property data are reported for three epoxy materials commonly used to impregnate superconducting solenoids, a filled epoxy, a flexibilized epoxy, and a low-viscosity epoxy suitable for vacuum impregnation. Impregnated superconducting test rings were also constructed using each type of epoxy. The critical current and training behavior of each composite ring was then measured as a function of hoop stress applied to the ring and correlated with the tensile properties of the corresponding epoxy. The ultimate strain, ε_u, of the epoxy impregnate was a primary controlling factor in the superconducting performance of each composite ring. At strains below ε_u, both critical-current degradation and training were negligible. At strains near ε_u, however, training became a serious problem with 5 to 10 quenches required to reach full critical current. These data would indicate that the training behavior of potted superdonducting magnets is associated with a process involving relief of stress concentration within the epoxy impregnant. In addition, the vacuum impregnated composites show less training required than the wet layup composites.

The Young's modulus of the composite coil materials was also measured by an acoustic resonance technique. All three of the coil materials described above were compared at room temperature and the vacuum impregnated composite was measured at 77 and 4 K as well. The values compare well with calculated values from a law of mixtures and values from conventional static tests.

1.2.3 Conductors

The tensile behavior of superconducting wire composed of twisted filamentary niobium-titanium stabilized with copper was determined at 4, 76, and 300 K. Continuous stress-strain measurements were recorded to fracture, allowing Young's modulus, yield strength, breaking strength, elongation, and stress-strain curves to be determined. Hardness measurements along with the length of wire were also obtained. Various strain-rates over three orders of magnitude were used.

The tensile and yield strengths of the Nb-Ti, copper, and wire composite appear well behaved from 4 to 300 K. The Nb-Ti has very little plastic deformation, signifying that little adiabatic heating can take place in the superconducting filaments prior to fracture. No discontinuous yielding was observed at 4 K. The yield strength was found to increase slightly with increasing strain rate and the elongation to decrease with increasing strain rate, both measured at 4 K. Anelastic unloading behavior was observed by the wire composite at 4 K. The degree of recovery was dependent on the maximum applied stress.

The first measurements of the effect of strain on the critical current of NbTi multifilamentary wires are reported. The results show a definite degradation of I_c with applied uniaxial strain, starting at about a strain of 0.5%. The effect amounts to about 5% at an applied

strain of 1%, rapidly increasing at still higher strain. The initial 20 to 30% decrease in critical current is almost totally reversible upon strain removal. The data are used to generate strain-dependent J_c-H characteristics for magnet design.

A number of possible explanations of the observed degradation in both NbTi and Nb_3Sn superconductors were hypothesized. The experimental evidence would suggest that the source of I_c degradation is associated with the superconductor itself, rather than with peripheral effects such as matrix degradation, heat generated by plastic deformation, area reduction, etc. At high strains in Nb_3Sn where the degradation is irreversible, the effect is well accounted for by $\gtrsim$ 100 nm cracks observed in the Nb_3Sn reaction layer. Where the degradation is mostly reversible (at lower strains in Nb_3Sn and at all strains in NbTi), the effect is most likely brought about either by a shift in the intrinsic critical temperature and field due to strain, or by an alteration of the vortex-pinning structure.

References

1. Fowlkes, C. W., Angerhofer, P. E., Newton, R. N., and Clark, A. F., "Characterization of a Superconducting Coil Composite," NBSIR 73-349, National Bureau of Standards, Boulder, CO (1973).
2. Clark, A. F., Weston, W. F., Arp, V. D., Hust, J. G., and Trapani, R. J., "Characterization of a Superconducting Coil Composite and Its Components," NBSIR 76-837, National Bureau of Standards, Boulder, CO (1976).
3. Clark, A. F., Arp, V. D., and Ekin, J. W., "Properties of a Superconducting Coil Composite and Its Components," 6th International Conference on Magnet Technology-MT6, Alpha, Bratislava (1978), p. 673.

4. Weston, W. F., "Low-Temperature Elastic Constants of a Superconducting Coil Composite," J. Appl. Phys. 46, 4458 (1975).

5. Clark, A. F., Mikesell, R. P., and Reed, R. P., "The Low-Temperature Tensile Behavior of Copper-Stabilized NbTi Superconducting Wire," Proc. Int. Cry. Mat. Conf., Kingston, Ontario, 1975, Adv. in Cry. Eng., Vol. 22, Plenum, New York (1976).

6. Hust, J. G., "Low-Temperature Thermal Conductivity Measurements on Longitudinal and Transverse Sections of a Superconducting Coil," Cryogenics 15, 8 (1975).

7. Jelinek, F. J., and Collings, E. W., "Low Temperature Thermal Expansion and Specific Heat Properties of Structural Materials," in: Materials Research for Superconducting Machinery - III and V, Clark, A. F., Reed, R. P., and van Reuth, E. C., Editors, DAD004586 (October 1974) and ADA030170 (April 1976).

8. Arp, V. D., "Stresses in Superconducting Solenoids, J. Appl. Phys. 48, 2026 (1977).

2. MATERIALS FOR SUPPORT STRUCTURES

2.1 FIBERGLASS-EPOXY IN A CONICAL SUPERCONDUCTING MOTOR SUPPORT

by R. E. Schramm and M. B. Kasen

2.1.1 Introduction

A conical fiberglass-epoxy field magnet support was designed for use in a 2.2 MW (3000 hp) model superconducting motor. Cone design was based upon cryogenic static mechanical property data published by Toth, et al.[1] for a type 1581 S-glass/E-787 epoxy resin composite. However, the cone tested in this program was fabricated with type 1581 S-glass cloth in an epoxy resin system known as NASA Resin 2. To check the material properties against design criteria, we tested flat panels of composites of the glass cloth with both types of resin. All tests were to failure in tension, compression, and shear at 350, 295, 76 and 4 K. The parameters measured were moduli, strengths, failure strains, and Poisson's ratios. Another objective was measurement of the cone's axial spring constant at 295 K and 76 K as a function of axial compressive force up to 89 KN (20,000 lb). However, as the flexibilizer in the NASA Resin 2 formulation was known to decrease the composite strength above room temperature, the cone was also tested at a temperature of 350 K.

2.1.2 Materials and Test Methods

Type 1581 glass cloth has an unbalanced 57 x 54 warp and fill, with an eight harness satin weave, i.e., the filling thread floats over seven warp threads and under one. This weave is especially adaptable for forming compound curves. Specially developed for cryogenic service[2], NASA Resin 2 consists of Epon 828/DSA/EMPOL 1040/BDMA* in proportions 100/115.9/20/1

*DSA = dodecenyl succinic anhydride
BDMA = benzyldimethylamine
NMA = nadic methyl anhydride
The use of trade names in no way implies endorsement or approval by NBS and is included only to assure complete identification of specimen materials.

by weight. Addition of EMPOL 1040 increases the flexibility of the resin, reducing the tendency of the resin to crack when cooled to cryogenic temperatures. The E-787 resin (also designated 58-68R or the Polaris formulation) consists of Epon 828/Epon 1031/NMA/BDMA in proportions 50/50/90/0.55 by weight. Lot 1 of the E-787 composite had 52.2 and 55.6 fiber volume percent respectively in 10 and 15 ply panels.

Apparatus and procedures for tension and compression testing were similar to those used in a prior program.[3,4] For the tensile tests, the flat panels had 10 plies, and for the compression and shear tests they had 15 plies. Tensile coupons were tapered similar to the MIL-HDBK 17A specification (width = 1.3 cm (0.5 in); gage length = 5.40 cm (2.13 in); thickness = 0.26 cm (0.10 in); and compression specimens were unsupported columns 0.38 cm (0.15 in) square, gage length = 1.3 cm (0.5 in)). Interlaminar shear strength (shear strength of the interface between layers in a layered composite) was evaluated by the unsupported guillotine method (ASTM D 2733-70) and the short-beam shear test (ASTM D 2344-72). All strain measurements came from strain gages bonded directly to the specimen surface.

Figure 2-1-1 shows the fixture used for measuring the axial stiffness of the fiberglass epoxy cone at 350, 295, and 76 K. As illustrated the cone skirt was seated in a recess on a 5 cm (2 in) thick cloth-reinforced phenolic base, machined to conform to the mating flange of the motor assembly. A stainless steel support ring clamped the skirt to the base. A 5 cm (2 in) thick cloth-reinforced phenolic plate, machined to mate with the lip of the small diameter of the cone, served as a pressure plate on the upper cone surface. Deflection was monitored by a linear variable differential transformer (LVDT) mounted axially between

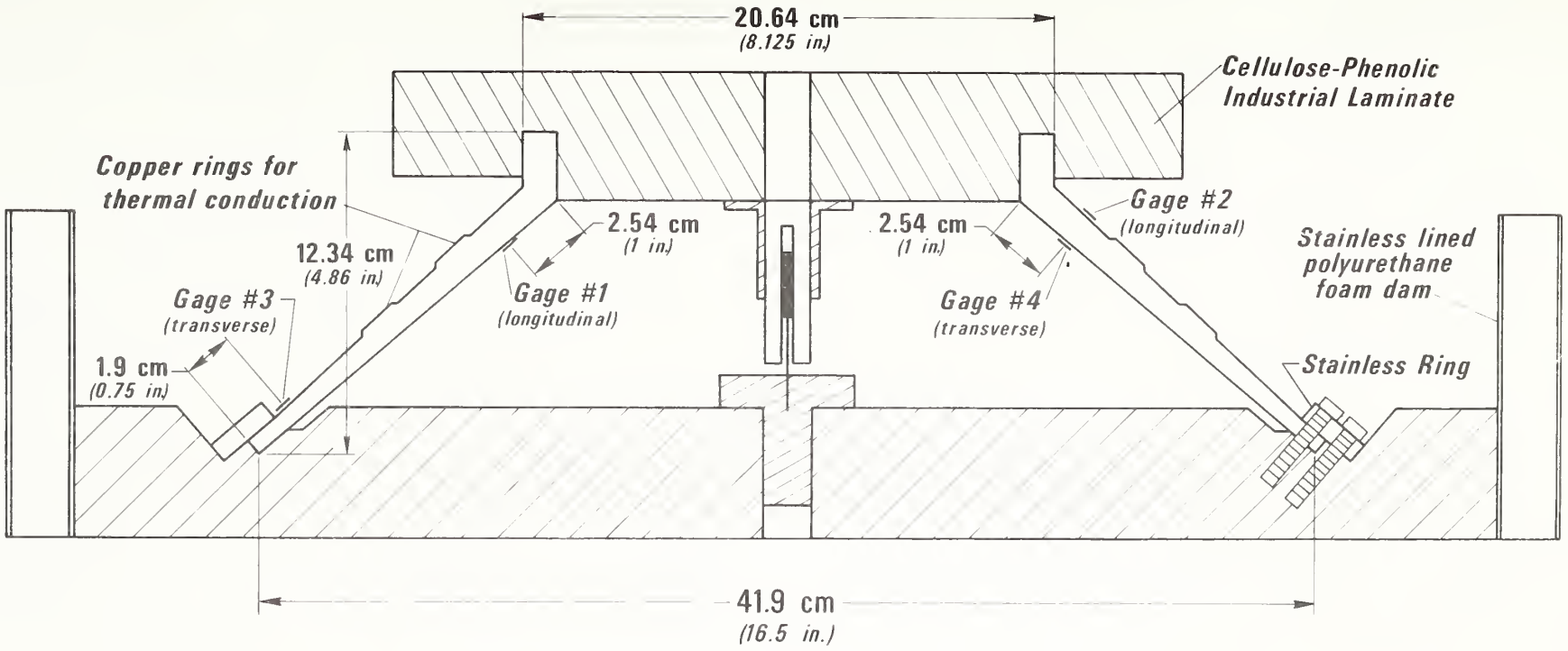

Fig. 2-1-1 Fixture for measurement of cone stiffness as a function of axial compressive force. Strain gages were bonded directly to the cone surface.

the upper and lower phenolic plates. Four strain gages at the locations indicated on Figure 2-1-1 provided localized strain data. Load was applied by a hydraulic testing machine. Estimated inaccuracy of the axial force was $\pm$ 3%; that of the LVDT was $\pm$ 0.00254 mm ($\pm$ 10^{-4} in). The LVDT was calibrated at 295 K and 76 K.

Liquid nitrogen was contained within a polyurethane foam ring, sandwiched between sheets of stainless steel and bonded to the phenolic base plate. The liquid level on both sides of the cone wall was midway between the two copper conduction rings in the cone for most tests (about halfway up the cone) as a simulation of the thermal gradient in service. The cone was slowly cooled over a 20- to 30-min interval to reduce thermal stresses between the copper conduction rings and the composite.

2.1.3 Results

Materials Characterization. The data in Table 2-1-1 are the results of the destructive tests of the flat panels and represent the averages of one to three tests; in general, the specimen-to-specimen variability was about 10 to 15%. In most instances, the stress-strain curve displayed the usual initial straight-line behavior (giving the primary modulus) followed by a second straight line of slightly lower slope (giving the secondary modulus) before going into plastic yield. The secondary strength is the point between primary and secondary moduli.

The tensile Resin 2 strength increases from 4.8 to 8.6 x 10^8 N/m^2 as the temperature drops from 350 to 4 K. The increase in compressive strength with temperature change is much more dramatic, going from 1.0 to 7.1 x 10^8 N/m^2. Interlaminar shear values from the guillotine test

Table 2-1-1 Mechanical Property Data Summary

Test	T(K)	Ultimate Strength 10^3 psi	Ultimate Strength 10^8 N/m^2	Secondary Strength 10^3 psi	Secondary Strength 10^8 N/m^2	Primary Modulus 10^6 psi	Primary Modulus 10^9 N/m^2	Secondary Modulus 10^6 psi	Secondary Modulus 10^9 N/m^2	Poisson's Ratio	Failure Strain %
1581 S-glass/NASA Resin 2											
Tensile	350	69	4.80	---	---	2.85	19.75	----	----	0.068	---
	295	83	5.48	---	---	3.82	26.30	3.37	23.2	0.135	---
	76	137	9.44	---	---	----	-----	----	----	-----	---
	4	124	8.58	≈18	≈1.26	4.59	31.60	3.53	23.7	0.184	---
Compressive	350	14	0.95	4.6	0.32	3.37	23.3	2.07	13.1	-----	0.5
	295	42	2.90	17.3	1.19	3.42	23.6	2.85	19.7	-----	1.4
	76	101	6.95	28.9	1.99	4.31	29.7	3.56	24.6	-----	2.6
	4	103	7.10	---	---	4.14	28.6	----	----	-----	2.6
Interlaminar Shear (Guillotine)	350	1.30	0.09	---	---	----	----	----	----	-----	---
	295	3.05	0.21	---	---	----	----	----	----	-----	---
	4	2.61	0.18	---	---	----	----	----	----	-----	---
1581 S-glass/E-787 (lot 1)											
Tensile	295	92.8	6.40	26.2	1.81	4.06	28.0	3.26	22.5	0.137	2.6
Compressive	295	73.2	5.04	28.1	1.94	4.52	31.2	3.79	26.2	-----	2.0
	4	113	7.76	33.5	2.31	5.58	40.3	4.42	30.5	-----	2.3
Interlaminar Shear (Guillotine)	295	1.34	0.092	---	---	----	----	----	----	-----	---
Interlaminar Shear (Short Beam)	295	8.91	0.615	---	---	----	----	----	----	-----	---
1581 S-glass/E-787 (lot 2)											
Compressive	350	56.4	3.89	31.2	2.16	4.25	29.3	3.37	23.2	-----	1.6
	295	66.4	4.58	25.8	1.78	3.96	27.3	3.00	20.7	-----	2.0
	4	106	7.25	28.5	1.96	4.83	33.3	4.17	28.8	-----	2.3
Interlaminar Shear (Guillotine)	350	2.16	0.149	---	---	----	----	----	----	-----	---
	295	1.99	0.137	---	---	----	----	----	----	-----	---
	4	2.15	0.149	---	---	----	----	----	----	-----	---

are disappointingly low at 0.1 - 0.2 x 10^8 N/m^2. All strengths of the E-787 composites are quite comparable to the Resin 2 composites at cryogenic temperatures but are considerably higher at room temperature and above.

In the course of testing, we noted that the panels contained large voids visible to the naked eye. Further examination under a low-powered microscope (Fig. 2-1-2) showed the porosity to be uniformly distributed. A check of void content (ASTM D 2734-70) in two labs indicated less than 1% total voids; however, an analysis of the porosity on the shear surface of failed interlaminar shear specimens showed in excess of 3.5% voids lying on the interlaminar shear planes. The interlaminar shear strength of the composite (Table 2-1-1) was significantly degraded by the porosity, an average value of 0.9 MN/m^2 reported for the same composite type by Toth, et al.[1] The manufacturer was informed of the problem and requested to supply a second lot of panels. Unfortunately, the porosity problem continued. As shown on Table 2-1-1, the interlaminar shear strengths of the second lot of E-787 panels remained low. Interlaminar porosity was also present in the Resin 2 composite, although to a lesser extent than in the E-787 material. The Resin 2 cone used in the stiffness study was found to contain the same amount and distribution of porosity as did the Resin 2 panels.

Axial Cone Stiffness. The first runs to a given axial force level were made with liquid nitrogen covering half the cone height so as to take advantage of the increased composite strength. Subsequent runs were made at 295 K. Initial cycling was to 49 KN during which no problems developed at either temperature. Subsequent cycling was to 89 KN. The

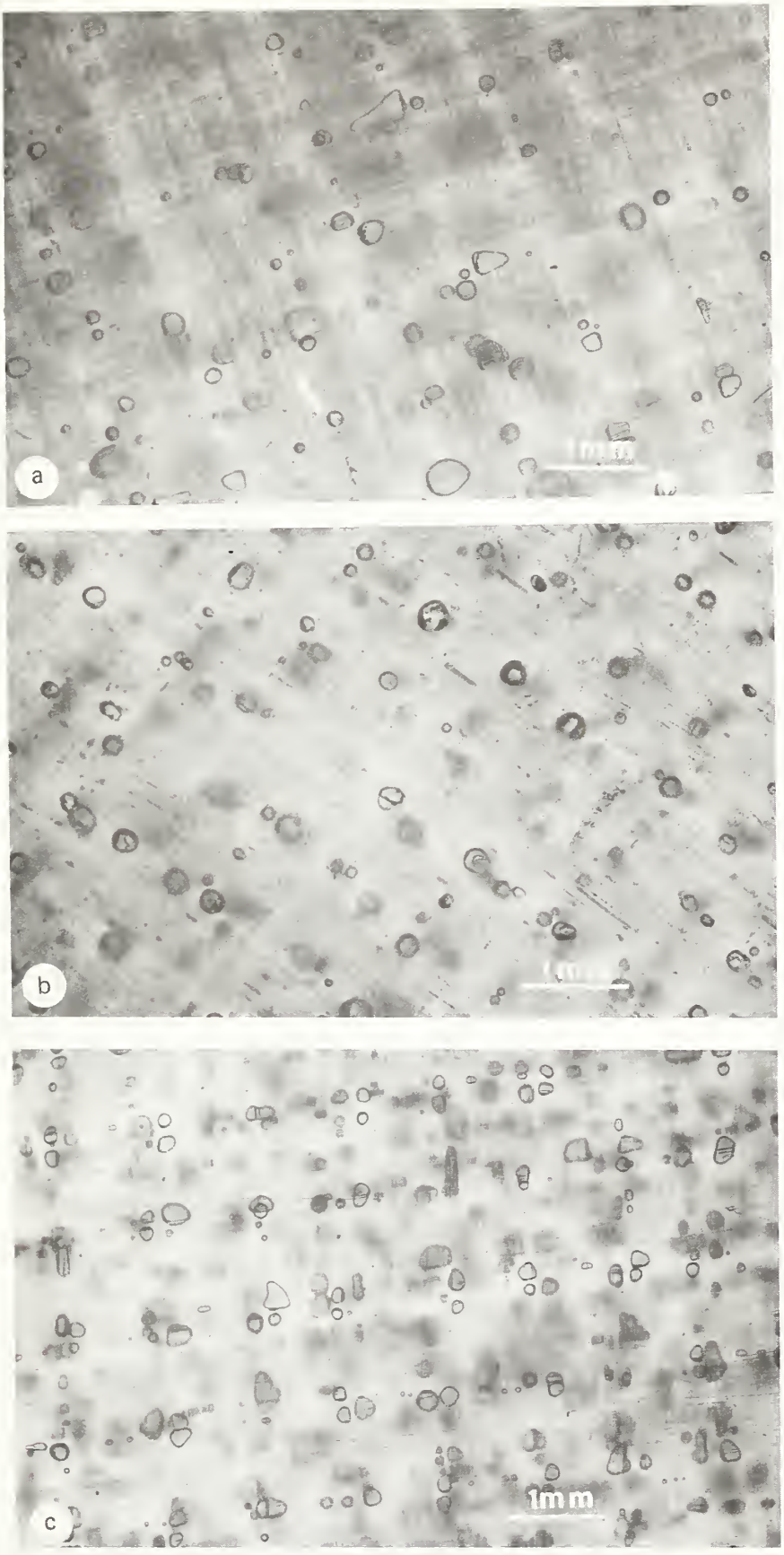

Fig. 2-1-2 Porosity lying on the interlaminar shear planes of 10 ply NASA Resin 2 and E 787 composites tested in this program. Transmitted light. a) 1581 S-glass/NASA Resin 2; b) 1581 S-glass/E-787 (Lot 1); c) 1581 S-glass/E-787 (Lot 2).

cone generated considerable noise during the first few cycles to this level at 76 K, sharp cracking noises being accompanied by load drops of 220-440 N. Loading to 89 KN at 295 K was uneventful. The cone survived these tests without visible evidence of damage. Cone stiffness was the same whether half covered or fully covered with liquid nitrogen.

The elevated-temperature runs (350 K $\pm$ 5 K) were limited to 49 KN. A commercial heat gun gradually heated the cone, allowing time for the temperature to equilibrate. The surface temperature was 360 K at the start of the test sequence, falling to 345 K after seven load cycles.

Cone stiffness data are summarized on Figure 2-1-3. The much lower cone stiffness at 76 K compared to that at 295 K is almost certainly due to restraint of the test fixture rather than to a changing material property, as the compressive modulus of the composite increases by about 25% on cooling to 76 K (cf. Table 2-1-1). Restraint of the cone skirt during cooling may distort the cone walls, permitting column bending under load. Alternatively, thermal contraction may be causing the skirt to pull away from its seat, in which case full cone stiffness would not be achieved until the applied load is sufficient to force the skirt tightly against the base. The increasing slope of the 76 K curve of Figure 2-1-3 is consistent with the latter interpretation.

Strains measured by the four gages at the locations given in Figure 2-1-1 are plotted as functions of axial compressive force to 49 KN on Figure 2-1-4 for temperatures of 350 K, 295 K, and 76 K. Only the output of gage #3 could be monitored at 76 K, as the remaining gages could not be stabilized. The observed strain at 49 KN was about 0.04% (gage #3) at all three test temperatures. Gage #2 indicated compressive

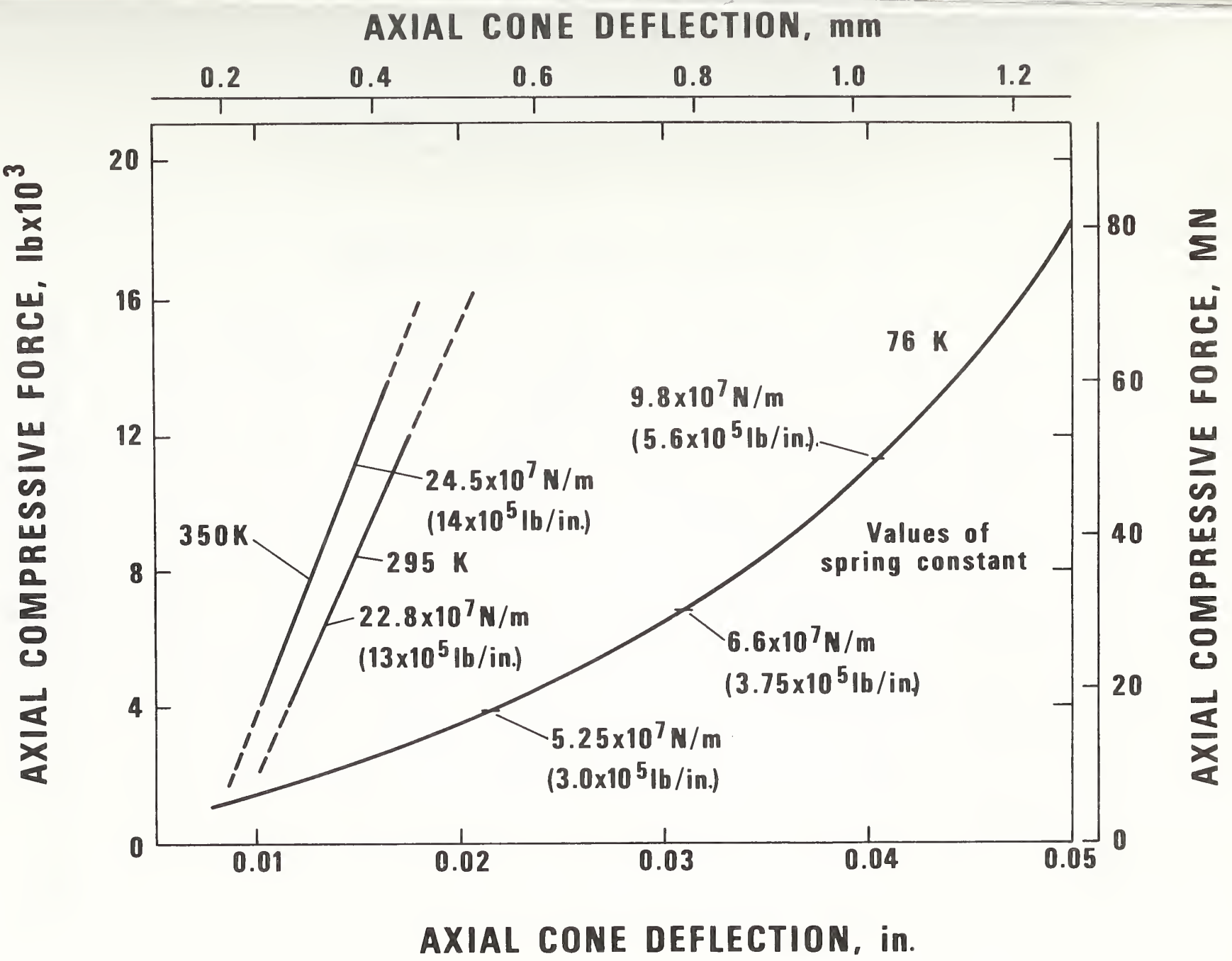

Fig. 2-1-3 Deflection of the Resin 2 cone as a function of axial compressive force. Calculated stiffnesses are noted.

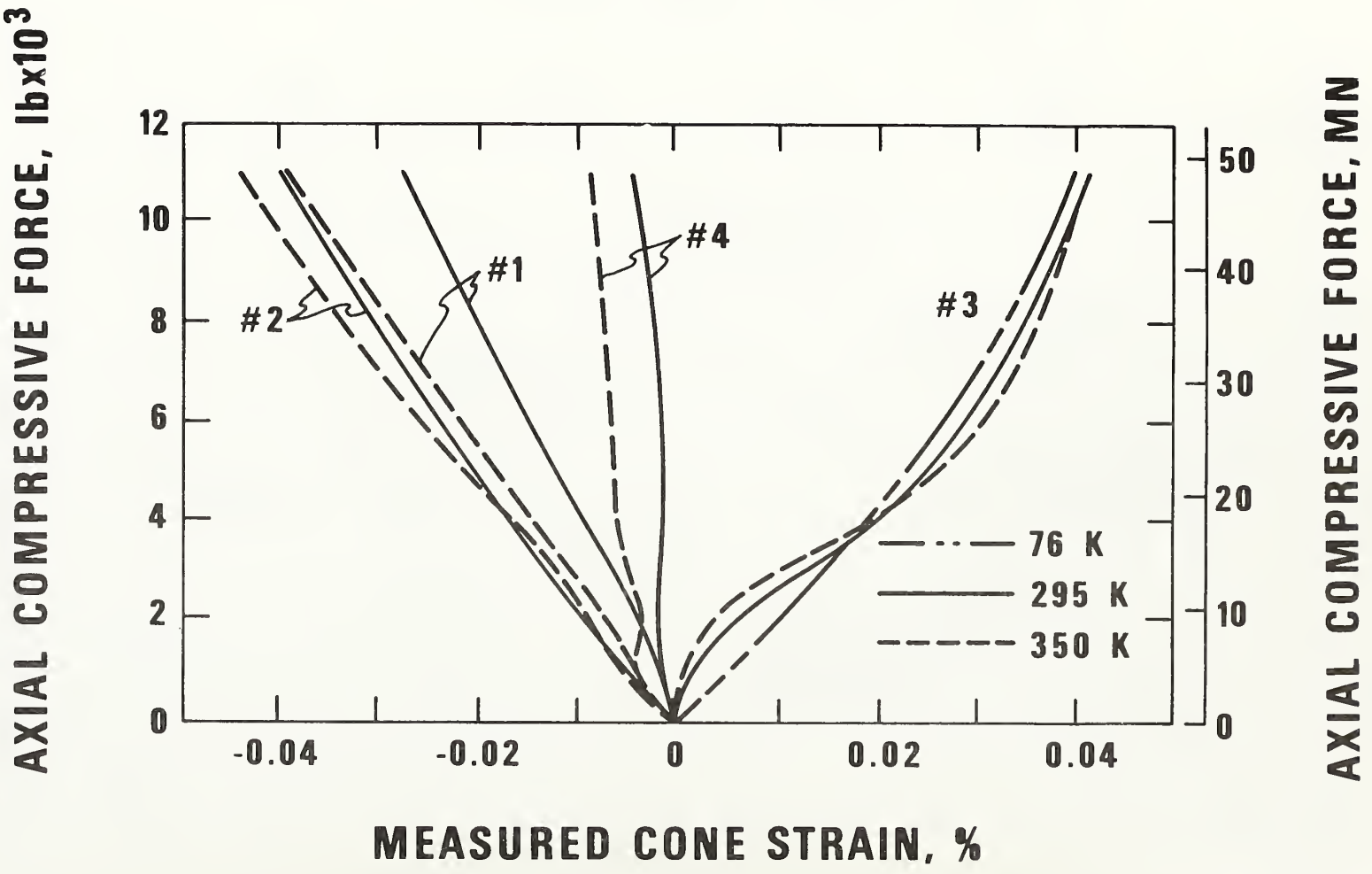

Fig. 2-1-4 Localized strain variations in the Resin 2 cone as a function of axial compressive force. Numbers refer to strain gages positioned as illustrated on Figure 2-1-1.

strains of similar magnitude. Compressive strains from gage #4 were much smaller (about 0.005%). Strain at gage #1 reached about 0.03%. The strain in the cone skirt (gage #3) shows little effect of temperature, but heating to 350 K did increase the output of all three gages near the cone apex. The hoop strain at the top (gage #4) may be very small due to the constraint of the test fixture. Comparison of gages #1 and #2 indicate a greater strain on the exterior than on the interior.

2.1.4 Discussion

The large amount of visual interlaminar porosity in the composite test panels reflects manufacturing problems. Since there is a considerable discrepancy between the results of the ASTM D 2734-70 test for void content and visual observation, it appears prudent to heed the caveat written into the test method, i.e., accuracy depends on an assumption that resin density is the same in bulk as in the composite but small differences in formulation or curing could render this invalid. The usual change between the two conditions make the void content appear lower than it really is.

The presence of porosity is clearly reflected in the very low interlaminar shear strengths measured in this program. Considerable controversy surrounds the subject of interlaminar shear testing of composites. We make no claim that the unsupported guillotine method used in the present work is ideal; however, this method is considered the best presently available for generating allowable strength data.[5] Our ultimate strengths from the guillotine shear tests are much lower than those for 1581 S-Glass/E-787 reported by Toth, et al.[1], while the present values from the tensile, compressive, and short-beam shear tests agree very well with theirs. Apparently, only the guillotine test

method is sensitive to interlaminar porosity. This may be an important factor to consider when using the relatively simple short beam method as a quality control or screening test.

Despite the low shear strength, we observed no degradation in strength or stiffness of the Resin 2 cone as the result of repeated axial loading to 89 KN at 76 K, 295 K, and 350 K. The noise generated during the 76 K loading undoubtedly reflected the onset of some "damage" to the composite. However, it most likely reflected a shakedown of the composite, not seriously affecting the strength and stiffness properties.

The axial stiffness of the Resin 2 cone was a constant at 295 K and at 350 K for loads in excess of about 9 KN with a spring constant of 22.8-24.5 x 10^7 N/m. At 76 K, the stiffness was a monotonically increasing function of load, attaining a stiffness of about 14 x 10^7 N/m at 89 K. We interpret this as a geometric effect due to restraint on the cone skirt during cooling. The unrestrained cone, tested at 76 K, should have a stiffness exceeding that at the elevated temperatures, consistent with the significant (25%) increase in the compressive modulus observed in the Resin 2 composite test materials upon cooling.

Acknowledgment

We wish to thank Michael J. Superczynski of the Naval Ship Research and Development Center and Robert A. Ackerman of Intermagnetics General Corporation for their cooperation in this program.

References

1. L. W. Toth, T. J. Boller, I. R. Butcher, A. H. Kariotis and F. D. Yoder, NASA CR-80061 (1966) N67-12051.

2. L. M. Soffer and R. Molho, NASA CR-72114 (1967) N67-25076.

3. M. B. Kasen and R. E. Schramm in: Materials Research in Support of Superconducting Machinery-I; R. P. Reed, A. F. Clark, E. C. van Reuth (Eds.); Nat. Bur. Stds., Boulder, CO; (March 1974) AD 780 596. See also: V. II (Oct. 1974) ADA 004 586, V. III (April 1975) ADA 012 365, V. IV (Oct. 1975) ADA 019 230.

4. R. E. Schramm and M. B. Kasen, Materials Science and Engineering, 30 (1977) 197.

5. Advanced Composites Design Guide, third Ed., V. IV, Materials, Wright-Patterson AFB, Ohio (1973) AD 916 6821.

2.2 FATIGUE RESISTANCE OF A UNIAXIAL S-GLASS/EPOXY COMPOSITE AT ROOM TEMPERATURES

by Ralph L. Tobler and David T. Read

2.2.1 Introduction

Glass-reinforced epoxy composites are prospective structural materials at cryogenic temperatures where high strength-to-density and strength-to-thermal-conductivity ratios are required and where relatively low elastic moduli can be tolerated. At temperatures from 295 to 4 K, these composites offer a combination of physical and mechanical properties unmatched by structural metals. Unfortunately, structural design data for composites at low temperatures are scarce, a fact which hinders the utility of these materials.

The advent of superconducting machinery prompted the need for mechanical property data for materials in a liquid helium environment at 4 K. Accordingly, programs were instituted to establish a data base.[1] Kasen's review[1,2] of the mechanical behavior of glass-reinforced composites concludes that tensile and fatigue strengths generally increase between 295 and 76 K; but, on further cooling to 20 K, there is a high probability that strengths will decrease. According to Kasen[1,2], below 20 K, tensile behavior has rarely been investigated, and fatigue data are non-existent.

In this study, fatigue tests of a filamentary-reinforced composite at room temperature and 4 K are described. Cycle life as a function of applied stress is evaluated to provide baseline fatigue data for a specific primary load carrying component of a superconducting motor. Some experimental aspects of fatigue testing at 4 K are discussed.

2.2.2 Experimental Procedure

The material tested was a unidirectional composite of Owens-Corning S-901 glass roving and an epoxy resin, SCI REZ 80[1].* Specimens were fabricated in the form of 12.38 cm long bands, as shown in Figure 2-2-1, using a single material lot and constant fabrication procedure. The specimen is a scaled down version of 68.5 cm long support bands designed for suspension of superconducting motor components in liquid helium. All specimen dimensions, except length, are equal to those of the service component. As specified by the manufacturer, the specimen fiber content is 82% by weight, 69% by volume; the void content is less than 1% by volume, and the density is 2.1 $g \cdot cm^{-3}$ at room temperature.

Using flanged bushings, the specimens were pinned to the grips of a cryostat enabling fatigue tests in a liquid helium environment, as shown in Figure 2-2-2. The cryostat frame has a load carrying capability of 100 kN; it consists of two tubular compression members which are bridged at the bottom. The lower halves of these members are AISI 304 stainless steel having a wall thickness of 3.18 mm. The upper sections, which experience a thermal gradient during testing, were fabricated from fiberglass-reinforced plastic tubes, 6.35 mm thick. This lightweight construction provides high specific strength and low thermal conductivity, with some sacrifice of rigidity; the stiffness of the frame and load train at 4 K is approximately 23 kN/mm. Details of this cryostat design were described by Fowlkes and Tobler.[3]

*Certain materials are identified in this paper in order to adequately specify the experimental procedure. In no case does such identification imply recommendation or endorsement by the National Bureau of Standards, nor does it imply that the material identified is necessarily the best available for the purpose.

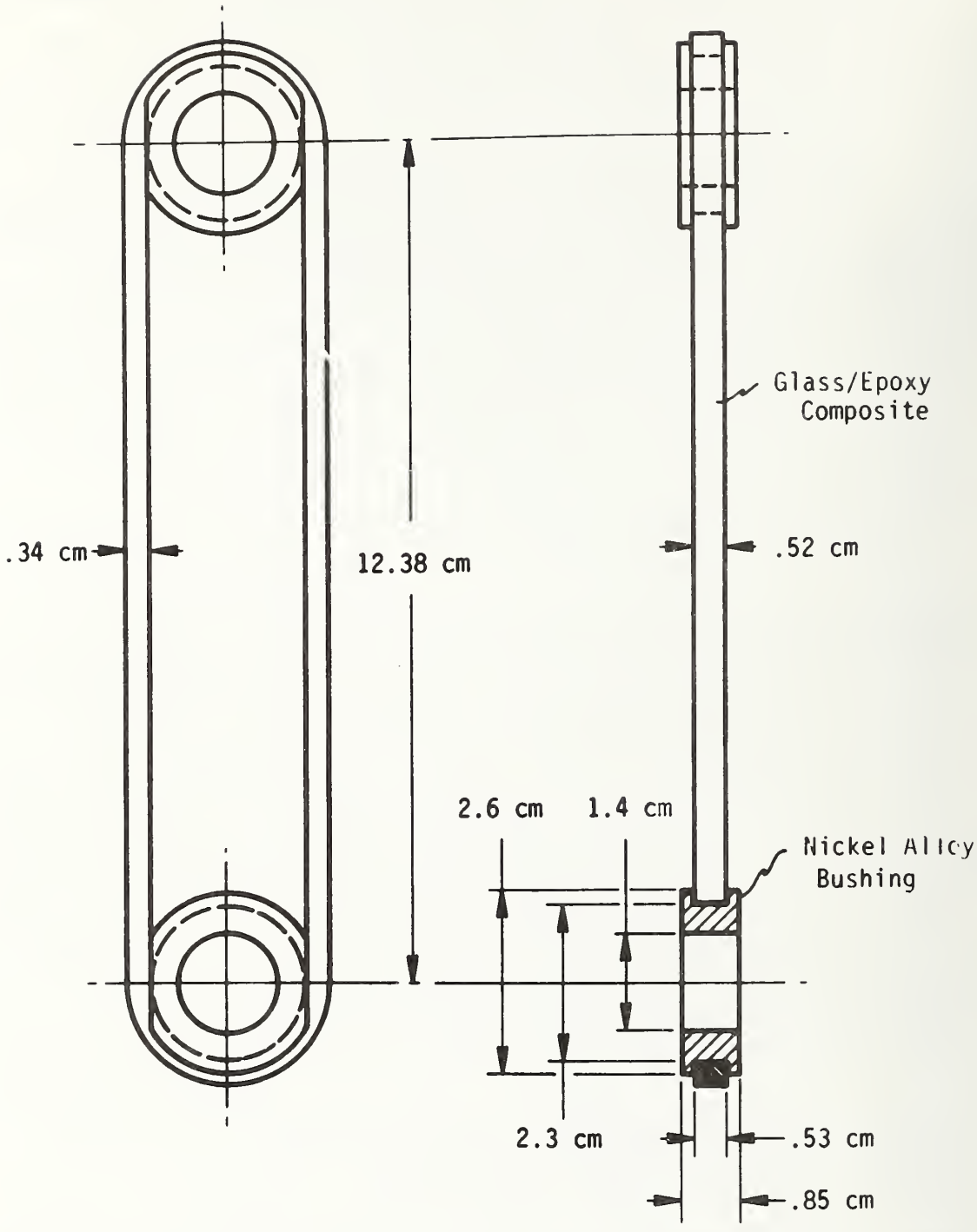

Fig. 2-2-1 S-901 glass/epoxy test specimen.

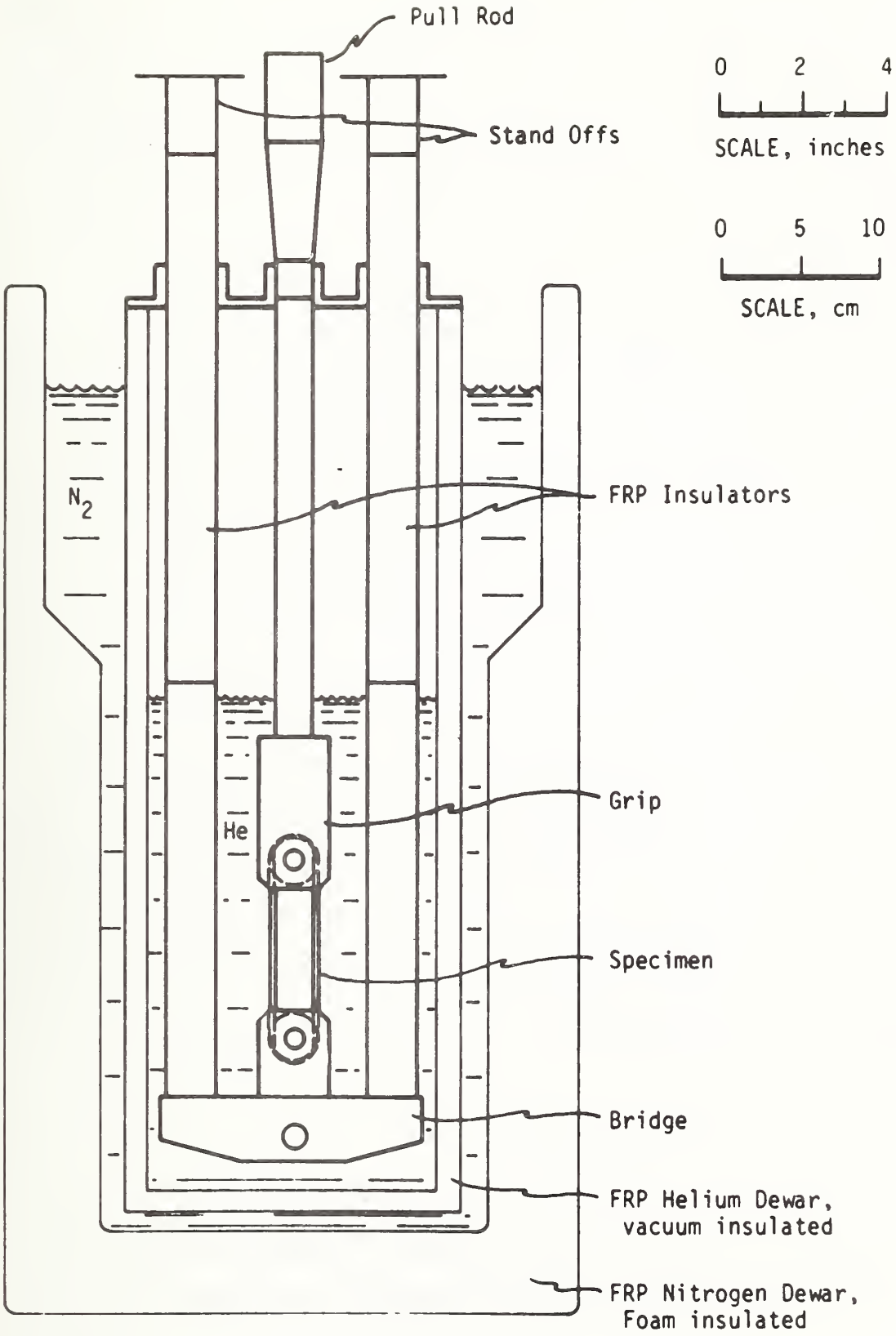

Fig. 2-2-2 Liquid helium fatigue cryostat.

Room temperature tests were performed with the apparatus in ambient air at 295 $\pm$ 2 K, and at a relative humidity of 30 $\pm$ 5%. The tests at 4 K were accomplished using the double-dewar arrangement illustrated in Figure 2-2-2. The specimen was enclosed in a fiberglass-reinforced plastic dewar, having a volumetric capacity of 9 liters. This dewar is vacuum insulated, and is surrounded by a fiberglass-epoxy dewar containing liquid nitrogen. Tests began by cooling the specimen and apparatus to 4 K, according to the two and one-half hour cool-down procedure previously described.[3] The liquid level was maintained several inches above the specimen, and was constantly monitored with a carbon-resistor level indicator. Liquid helium was continuously transferred into the cryostat to replenish the large amounts evaporated during fatigue tests.

All tests were conducted using a 100 kN closed-loop servo-hydraulic test machine. Replicate tensile tests were conducted at a loading rate of 5.7 $N \cdot s^{-1}$ to determine the nominal fracture strength and load-deflection (P-δ) characteristics of virgin specimens. Load cell and LVDT outputs were used in recording load-versus-actuator displacement curves. The nominal fracture strength, σ_f, was calculated from the maximum load, P_{max}, and the mean cross-section area 2A of the unloaded specimen at room temperature:

$$\sigma_f = P_{max}/2A \qquad (1)$$

The specimen stiffness, P/δ_S, was obtained by deducting the load frame deflection, δ_F from the total actuator displacement, δ_T:

$$\frac{P}{\delta_S} = \frac{P}{(\delta_T - \delta_F)} , \qquad (2)$$

where the load frame stiffness was measured separately by replacing the specimen with a rigid steel block. The nominal or effective value of specimen modulus was also calculated:

$$M_S = PL/2A\delta_S \qquad (3)$$

where L is the initial specimen length at room temperature, and δ_S is the specimen deflection at a 10 kN load.

The axial fatigue tests were conducted under controlled load, using a sinusoidal load cycle, at frequencies from 25 to 27 Hz. The ratio, R, of minimum/maximum load was 0.1, except as noted in the test. A digital indicator was used to measured the peak loads, which were controlled to within 2% of the specified values.

2.2.3 Results

A representative load-displacement record obtained at 4 K is shown in Figure 2-2-3a, and static tensile results are listed in Table 2-2-1. There was no measurable change in stiffness or modulus between 295 and 4 K, but tensile strength increased by 28% above room temperature value of 133.4×10^7 N · m^{-2}. The scatter in tensile strength at 4 K was higher than at room temperature, with one specimen at 4 K failing at a stress lower than any of the room temperature values. This anomalous result was not included in the average value of fracture strength listed in Table 2-2-1: the load-displacement record of the test of this specimen shows a noticeable increment in the displacement without a corresponding increase in the load at a low value of the load, as can be seen in Figure 2-2-3b.

Table 2-2-1 Static tensile properties of S-901 glass/epoxy specimens

Temperature (K)	Specimen (No.)	Mean X-sect. Area, 2A (cm^2)	Stiffness P/δ_s (10^5 N·m^{-1})	Effective Modulus, M_s (10^9 N·m^{-2})	Nominal Failure Strength, σ_f (10^7 N·m^{-2})
295	1[a]	.3612	N/A	N/A	134.6
	2[a]	.3604	"	"	133.8
	3[a]	.3648	"	"	131.6
	Avg.				133.4
	13	.3677	159	62.8	N/A
	14	.3652	148	61.8	"
	19	.3613	151	60.5	"
	Avg.		153	61.7	
4	4	.3664	160	66.7	158.8
	5	.3664	147	61.1	182.1
	21	.3652	145	60.6	126.7[b]
	Avg.		151	62.8	170.4

[a]Tests performed by the manufacturer [4].

[b]Not included in the average (see text).

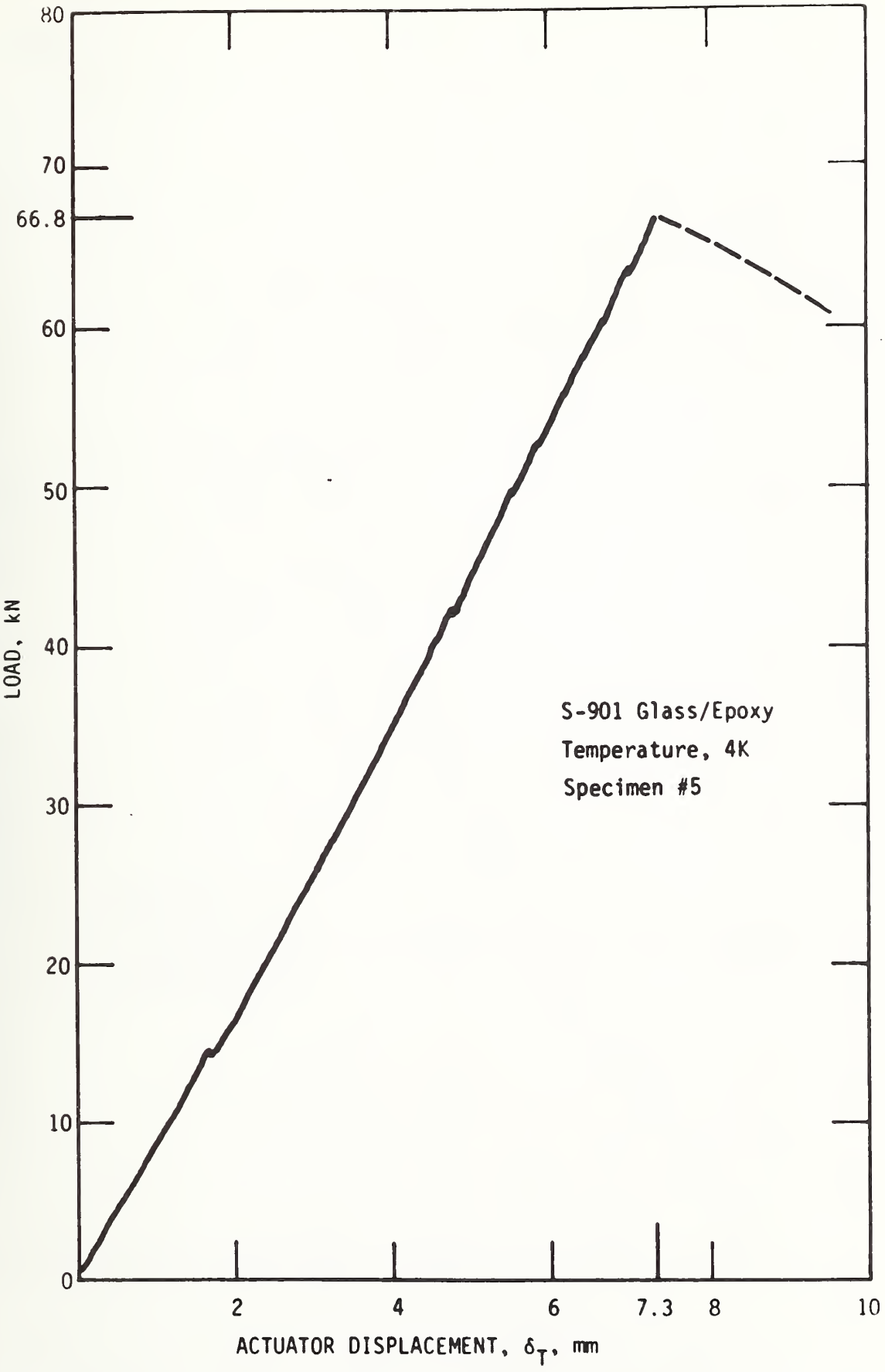

Fig. 2-2-3a Static test records; ordinary failure.

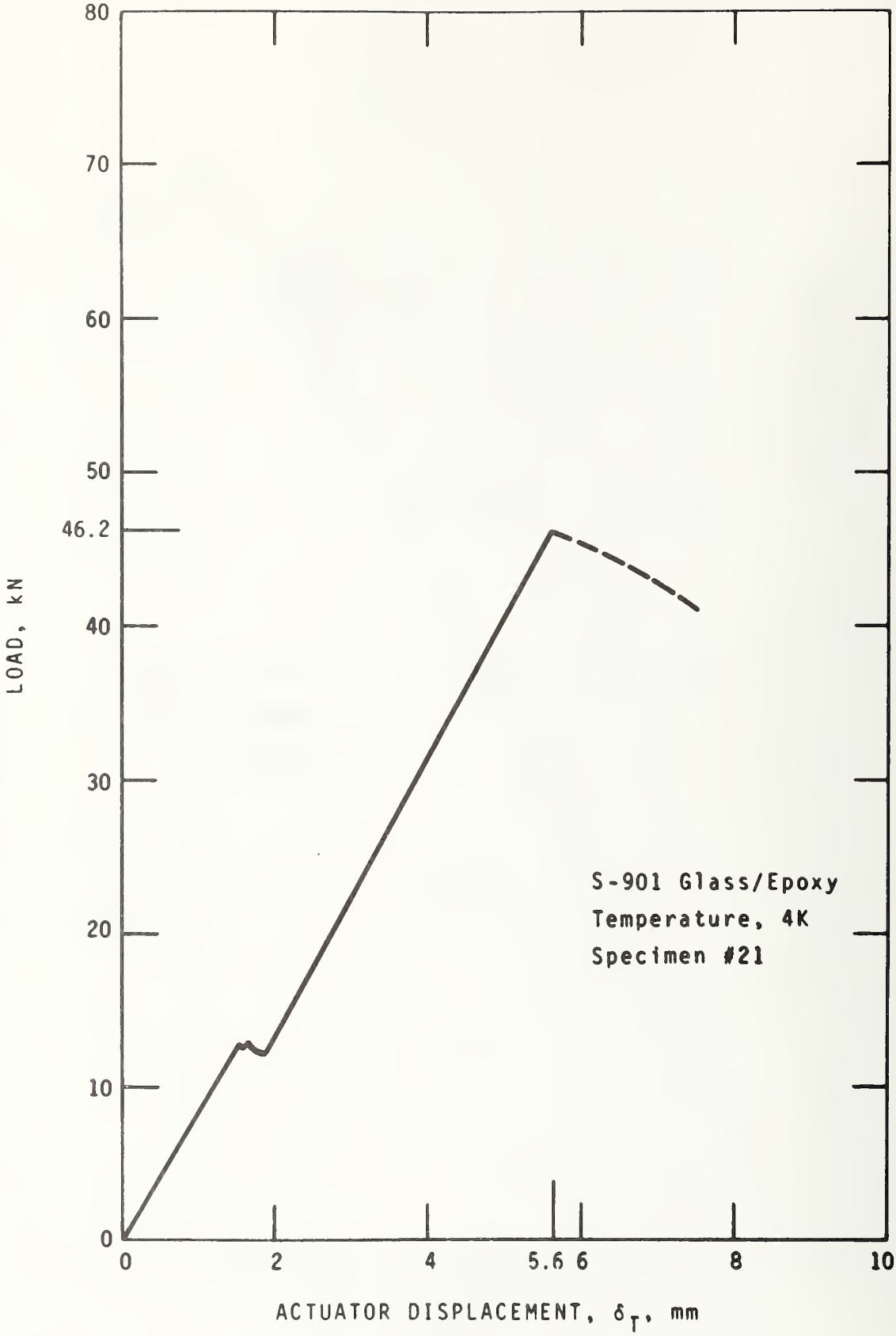

Fig. 2-2-3b Static test records; premature failure.

The room temperature fatigue results are shown in Figure 2-2-4, where the maximum fatigue stress is plotted as a fraction of the static strength. The data trend and scatter are similar to other results, particularly those reported by Hofer and Olsen[5] for a unidirectional S-994 glass filament-reinforced epoxy. Hofer and Olsen's data pertain to conventional hour-glass specimens having a tensile strength of about 162×10^7 N $\cdot$ m^{-2}. Although their material exhibited a higher cycle life capability at a given absolute stress value, the results for both composites can be normalized on the basis of differences in static strength as shown in Figure 2-2-4. It is also significant to note that these materials at room temperature do not exhibit a fatigue limit at cyclic stress levels as low as 20% of the static strength.

The effect of varying the load ratio was investigated briefly at room temperature where two specimens were fatigued to fracture at R = 0.5. As shown in Figure 2-2-4, the cycle life appeared to improve at the higher load ratio; further conclusions are not justified in view of the limited data.

The fatigue data obtained at liquid helium and room temperatures are summarized in Table 2-2-2 and Figure 2-2-5. These results clearly demonstrate a superior fatigue resistance at 4 K. Two specimens survived 10^6 stress cycles of maximum levels 29.0 and 30.0 $\times 10^7$ N $\cdot$ m^{-2} (17.6% of tensile strength) at 4 K without failure; their tensile strength and effective modulus after cycling were only slightly less than the average values for virgin specimens, as shown in Table 2-2-2b. These high values of residual strength and residual modulus indicate that cyclic loading at these levels at 4 K does not significantly degrade the load-bearing capability of these composite specimens. A third specimen failed

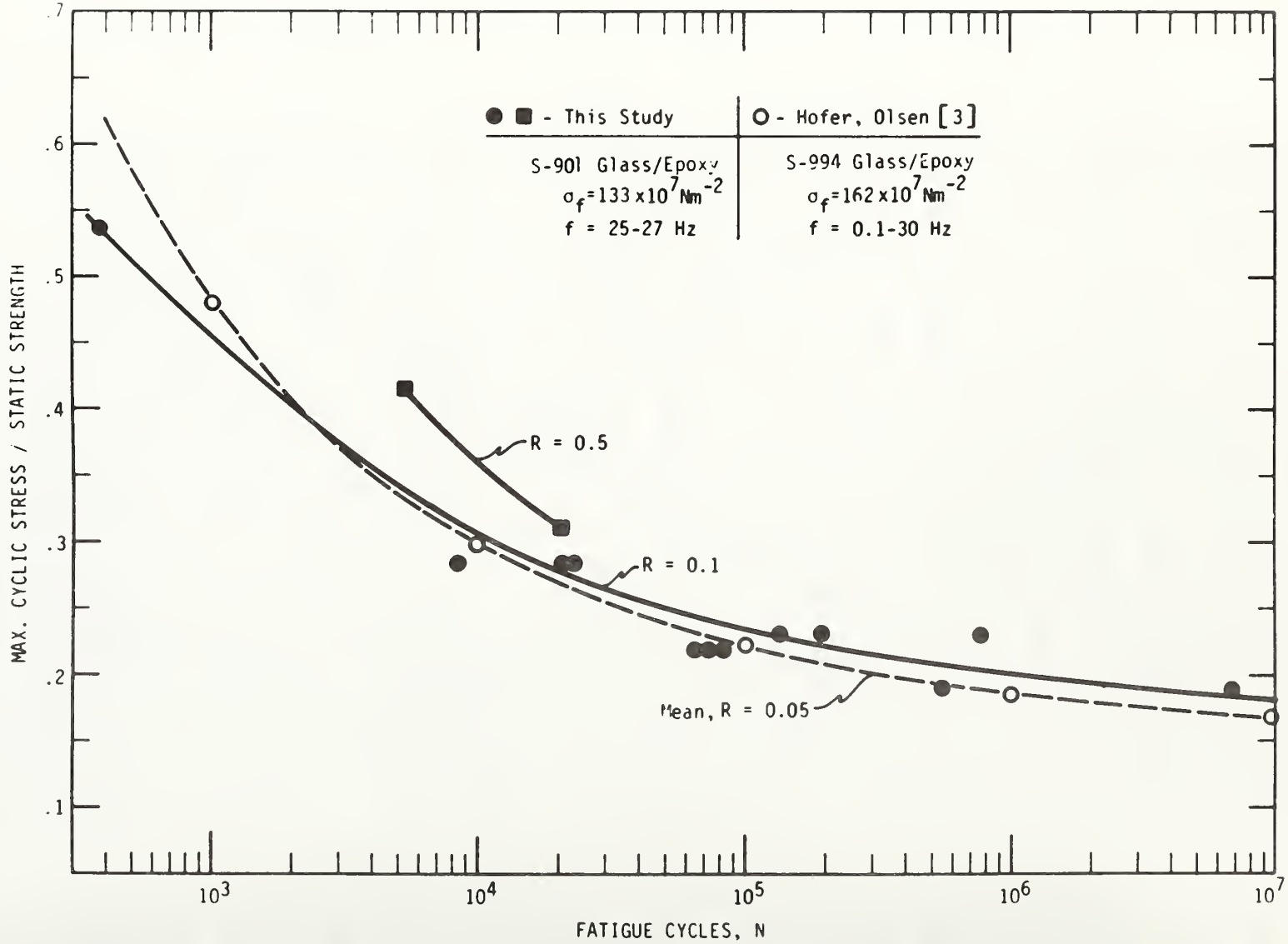

Fig. 2-2-4 Room temperature fatigue data, with stresses normalized to the static strength, showing the agreement between present results and those of Reference [5].

Table 2-2-2a Fatigue Results for S-901 glass/epoxy at 295 K

Specimen (No.)	Maximum Cyclic Stress, σ_M (10^7 N•m^{-2})	Fatigue Cycles to failure (No.)
13	25.5	7.246×10^6
19	25.5	5.76×10^5
9	29.3	6.75×10^4
16	29.3	8.36×10^4
18	29.3	7.38×10^4
7	31.0	1.96×10^5
12	31.0	1.42×10^5
20	31.0	7.46×10^5
6	37.9	8.85×10^3
10	37.9	2.22×10^4
11	37.9	2.09×10^4
24	71.0	3.93×10^2
22[a]	41.4	2.00×10^4
23[a]	55.2	5.40×10^3

[a] $R = 0.50$

Table 2-2-2b Fatigue results for S-901 glass/epoxy at 4 K

Specimen (No.)	Maximum Cyclic Stress, σ_M (10^7 N·m^{-2})	Fatigue Cycles (No.)	Residual Strength (10^7 N·m^{-2})	Residual Modulus (10^9 N·m^{-2})
8	29.0	1×10^6 (run-out)	139	58.2
17	31.0	1×10^6 "	156	65.8
14	71.0	1.49×10^4 (failure)	N/A	N/A
15[b] - 1	37.9	2.36×10^5 (run-out)	"	"
2	44.8	6.92×10^4 "	"	"
3	55.2	1×10^4 "	"	"
4	62.1	1×10^4 "	"	"
5	69.0	1×10^4 "	"	"
6	82.7	2.52×10^4 (failure)	"	"

[b]Cycled at increasing stress levels.

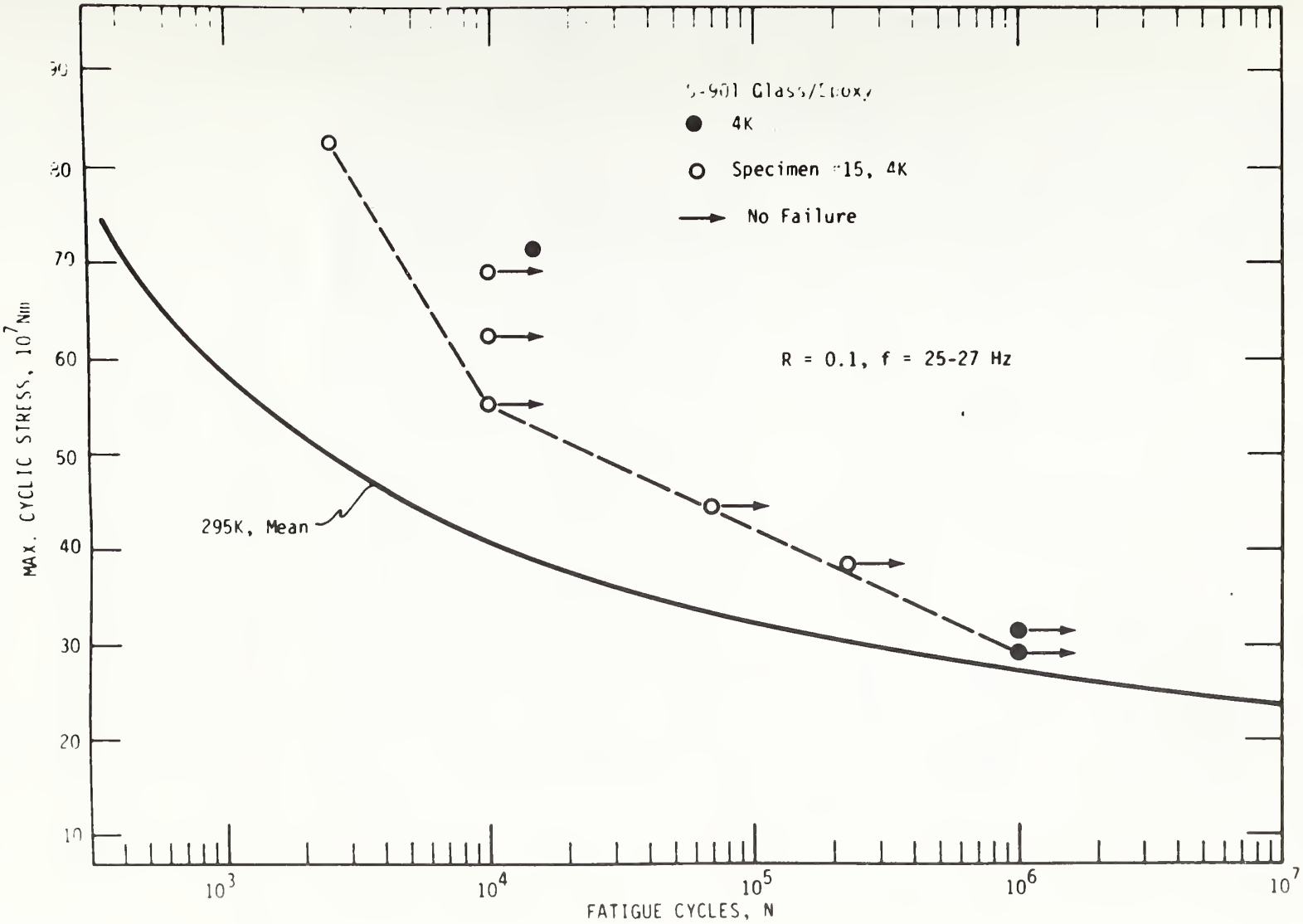

Fig. 2-2-5 4 k fatigue results, demonstrating a superior low temperature fatigue resistance, as compared to room temperature results.

after 1.49×10^4 cycles at a stress level of 71.0×10^7 N · m^{-2}, exceeding the room temperature endurance by a factor of 30. A final specimen was cycled for specified intervals at the increasing stress levels listed in Table 2-2-2. The results show that the cycle life at 4 K is at least ten times greater than at room temperature for maximum cyclic stresses from 38 to 82×10^7 N · m^{-2}.

Although a reliable S-N curve at 4 K could not be constructed without more extensive data, it appears that the stress level required for failure at a specified number of cycles may approach twice the value required at room temperature. The improvement in fatigue resistance at 4 K exceeds that which might be predicted based on scaling the fatigue stress levels to account for the increase in static strength alone.

Fatigue and tensile specimens fractured at 4 K are shown in Figure 2-2-6. Failure invariably occurred at points of tangency where the specimen contacted the bushings. Fatigue cracks initiated concurrently at all four of the points of tangency; the cracks penetrated the specimen ligaments along planes normal to the tensile axis; and delaminations subsequently emanated from the gripped regions. The delaminations propagated gradually in a direction parallel to the loading axis, along the entire length of the specimen. When fatigue damage reached critical proportions the weakest ligament splintered into filaments, which was the failure mode of tensile specimens, as shown in Figure 2-2-6. The epoxy at the four points of tangency in specimens fractured in fatigue at both 4 K and 295 K was quite dark, possibly indicating charring. Test temperature had no obvious influence on the appearance of these failures.

Fig. 2-2-6 Tensile (lower) and fatigue (upper) failures of specimens tested at 4 K.

Specimen deflection at maximum fatigue load increased progressively, as shown in Figure 2-2-7 for room temperature specimens fatigued at 25.5 x 10^7 N · m^{-2}. The rate of increase of deflection differed by an order of magnitude for these specimens, as did their fatigue lifetimes, N_f. This suggests that scatter in cycle life is due to specimen-to-specimen variability in resistance to fatigue damage propagation, as well as initiation. The loss of stiffness was always most pronounced during the last few cycles to failure, and extreme adiabatic heating was also noted in the terminal stages of fatigue.

2.2.4 Discussion

Relating laboratory results to service behavior is a practical problem which was minimized in this study by performing a limited number of tests under conditions nearly equivalent to those of the service application. The results must be regarded as lower bounds on the uniaxial tensile properties of the material itself, since the gripping fixture influenced the results. However, the gripping fixture is a practical one for service applications, and the data reported here are directly applicable in design.

It can be concluded from the 4 K results and known trends between 295 and 20 K^2 that the fatigue and tensile strengths of this material are lower at room temperature than at any cryogenic temperature. In the application under consideration, the component will experience temperatures ranging from 295 to 4 K. The room temperature properties are therefore limiting, and should form the basis for design. In certain applications where a component operates exclusively at cryogenic temperatures, it would also be possible to design conservatively on the basis

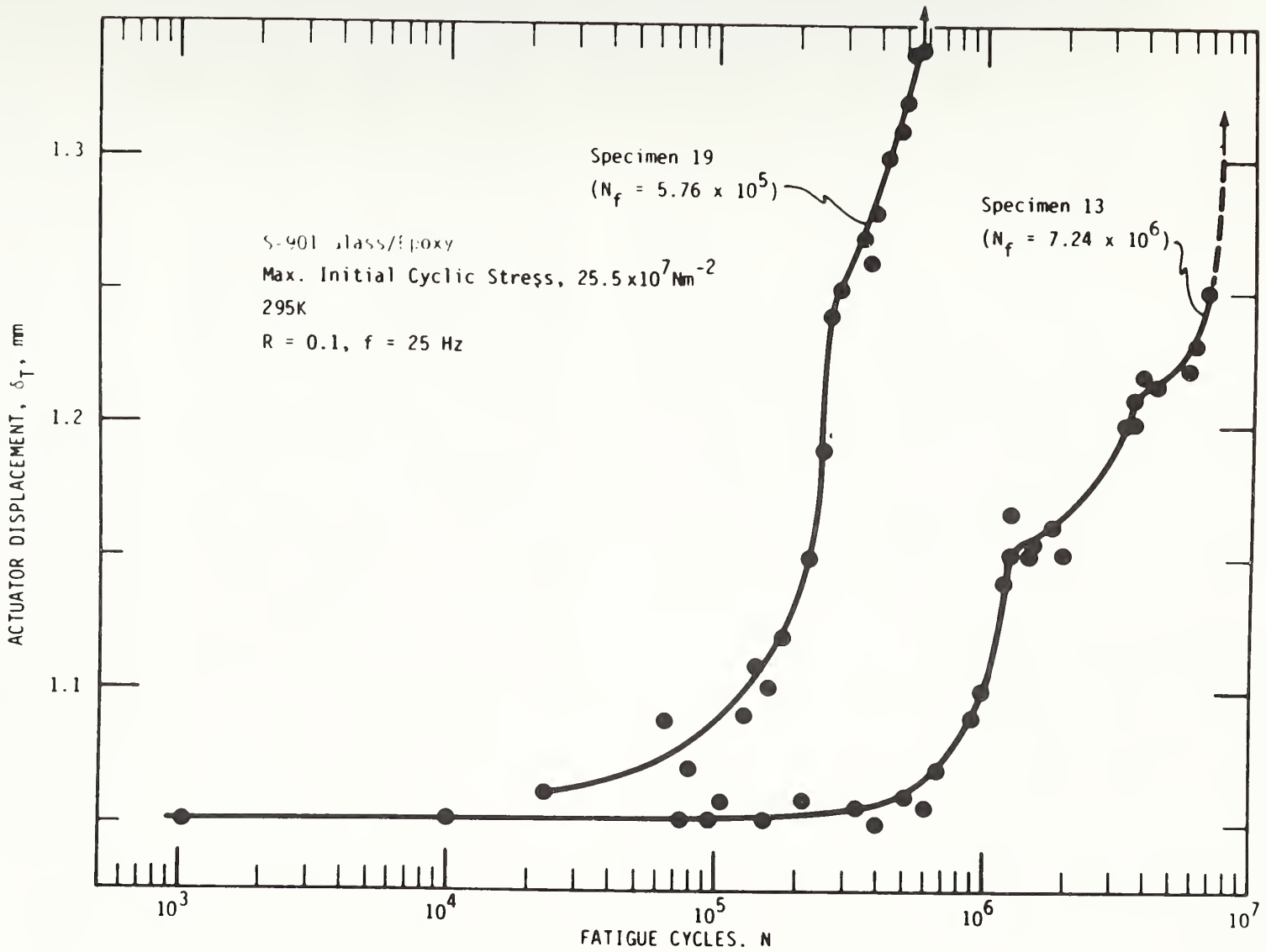

Fig. 2-2-7 Deflection-versus-cycles for specimens tested at 295 K, showing the increase in compliance preceding failure.

of room temperature properties. However, a maximum level of design efficiency at cryogenic temperatures requires more extensive low temperature mechanical property data.

In many structural applications, it is essential to monitor fatigue damage and to replace critical components before catastrophic failure becomes probable. The occurrence of delaminations in this composite after 25% of total cycle life provides obvious evidence of degradation. Damage could be detected earlier by dismounting the specimen to examine the surfaces in contact with the bushing. Surface deterioration and discoloration were noted at these locations. The loss of stiffness also provides a means of detecting fatigue damage. Thus, a simple inspection of service components should provide ample evidence of degradation prior to failure.

Cyclic stressing produces specimen heating and agitation of the cryogen. This agitation increases the heat leak into the cryogen due to convection, because the cryogen is splashed into the warmer regions of the cryostat. The heat input to the cryogen from both of these sources increases strongly with displacement. In these tests the helium loss under static load was only 0.15 $\ell \cdot h^{-1}$. This increased during fatigue tests, varying from 7 to 15 $\ell \cdot h^{-1}$, over the range of stress levels investigated.

Adiabatic heating in glass-reinforced plastics results from their high internal friction and low thermal conductivities.[6] Internal temperature rises as high as 40 K were noted in room temperature fatigue tests of such materials.[7] At 4 K, adiabatic heating should be more significant since the thermal conductivity of glass reinforced epoxies

is lowered by a factor of three.[4] Furthermore, the temperature in the interior of the specimen depends on the specimen thickness and cycling rate. Since the present data pertain to a specimen thickness and frequency equivalent to service conditions, the effects of adiabatic heating on fatigue resistance here are academic from an applications viewpoint. However, this effect must be accounted for in future tests if fatigue results are to be independent of specimen geometry and test variables.

2.2.5 Conclusions

From these tests, the following conclusions can be drawn:

1. The tensile strength and fatigue resistance exhibited by a glass roving reinforced epoxy plastic (GFRP) composite material indicate that such composites can be attractive structural materials for cryogenic applications.

2. The fatigue life of a GFRP composite material can be an order of magnitude greater at liquid helium temperature than at room temperature.

3. A measurable decrease in the stiffness of GFRP specimens may precede high cycle fatigue fracture at 295 K.

Acknowledgment

The cooperation of M. Calderon of Airesearch, Torrance, California in providing the specimens and reviewing the manuscript is gratefully acknowledged.

References

1. R. P. Reed and A. F. Clark, Eds., "Materials Research for Superconducting Machinery," National Bureau of Standards, Boulder, Colorado, AD 780596 and Ad/A 004 586, Nat. Tech. Inf. Serv., Springfield, Virginia (1974).

2. M. B. Kasen, "Mechanical and Thermal Properties of Filamentary-Reinforced Structural Composites at Cryogenic Temperatures - I: Glass-Reinforced Composites," Cryogenics, Vol. 15 (1975), p. 230.

3. C. W. Fowlkes and R. L. Tobler, "Fracture Testing and Results for a Ti-6Al-4V Alloy at Liquid Helium Temperature," Eng. Fract. Mechs., Vol. 8 (1976) p. 487.

4. M. Segimoto, "Qualification Test Results for Glass Filament-Wound Support Bands," Report No. 7581, Structural Composites Industries, Inc., California (Jan. 1975).

5. K. E. Hofer, Jr. and E. M. Olsen, "An Investigation of Fatigue and Creep Properties of Glass Reinforced Plastics for Primary Aircarft Structures,"Report M6104, Ill. Inst. Tech. Res. Inst. (Apr. 1967).

6. L. J. Broutman, "Fibre-reinforced Plastics," Chap. 13 in Modern Composite Materials, L. J. Broutman and R. H. Krock, Eds., Addison-Wesley, Massachusetts (1967).

7. R. B. Heywood, Present and Potential Fatigue and Creep Strengths of Reinforced Plastics, Tech. Note. No: Chem. 1337, Royal Aircraft Establishment, Ministry of Supply, London, W. C. 2 (Oct. 1958).

3. COMPOSITE COIL MATERIALS

3.1 EFFECT OF STRAIN ON EPOXY-IMPREGNATED SUPERCONDUCTING COMPOSITES

by J. W. Ekin, R. E. Schramm, and A. F. Clark

3.1.1 Introduction

Flux-jump stabilized superconducting magnets are usually impregnated with epoxy to prevent wire movement and enhance stability. Hoop stress experienced by the windings when the magnet is energized would otherwise cause wire movement, leading to localized heating and, quite probably, thermal runaway.

Unfortunately, the epoxy itself can act as a source of localized heating and initiate thermal runaway. This occurs when the epoxy is stressed to the point of fracture by a combination of magnetic hoop stress and stress introduced by differential thermal contraction betweeen the epoxy and superconducting wire during cooldown. Usually, failures take place only locally in regions of stress concentration. The local density of released energy, however, is usually more than adequate to initiate thermal runaway. Thus, epoxy impregnation of flux-jump stabilized magnets would be expected to contribute to their stable operation only at moderate stress levels. At some point of strain, localized failure of the epoxy is expected to degrade magnet performance. The purpose of this study is to see if this point can be predicted from the mechanical properties of the epoxy. A further purpose is to determine if the epoxy properties have any correlation with the common problem of magnet "training", wherein a flux-jump stabilized magnet must be quenched a number of times before it reaches the final design field.

This study is divided into two parts: first, a study of three types of epoxies commonly used in the construction of potted magnets;

second, a preliminary study of superconducting rings potted with these epoxies.

3.1.2 Epoxy Tests

Specimen Preparation and Tensile-Test Apparatus. Mixing of epoxy components was according to manufacturers'* directions; in some cases, outgassing the mixture at about 600 Pa (6×10^{-3} atm) for 5 to 10 minutes followed. Curing was in a silicone-rubber mold and yielded a flat, tapered specimen, accoring to ASTM D 638, Type I;[1] the gage length was 5 cm long and 1.3 cm wide with a thickness of about 0.5 cm. After the prescribed cure, commercial metal-foil strain gauges were attached directly to the specimen surface (the strain-gage-cement cure temperature was well below that of the test epoxy cure temperature). Specimen conditioning prior to testing was at least 50 hours at 50% relative humidity and 23°C (ASTM D 618, procedure A).[2]

The specimen grip system was 100 mesh stainless steel screen wrapped around 2.5 cm of each end before clamping between two stainless steel plates (0.6 cm thick) cross-serrated with 10 lines/cm. After assembly in an alignment jig, three pairs of 10-32 screws, torqued to

---

*Epoxy A, Armstrong A12, manufactured by Armstrong Products Company, Warsaw, Indiana; Epoxy B, Stycast 2850FT, manufactured by Emerson and Cuming, Canton, Massachusetts; Epoxy C, Araldite 6004, manufactured by Ciba Products Company, Summit, New Jersey, mixed with Lindride 16 hardener, manufactured by Lindau Chemicals, Inc., hardened and cured for 8 h at 80°C. Trade names are used to define the materials that were studied. Their use implies no endorsement of particular products by NBS.

2.3 to 4.5 N-m (20 to 40 in-lbs), were used to clamp the grip onto the specimen. Holes in the steel plates allowed a load pin attachment to clevises on each pull-rod. The test frame design[3] made it possible to immerse the entire system in a dewar of liquid helium.

During the test, a two-pen X-Y plotter recorded strain gage output as a function of load. Our procedure was to load cycle the specimen (strain rate, $\dot{\varepsilon} = 3 \times 10^{-4}\ s^{-1}$) to 25 to 35% of its ultimate strength four times with high sensitivity settings on the plotter; these data yielded the elastic parameters. We decreased the plotter sensitivity on the final loading cycle to record the fracture parameters.

Epoxy Results. Table 3-1-1 shows the mechanical property results for three types of epoxies at both room temperature and at liquid helium temperatures. The flexibilized epoxy A has a low modulus and high ultimate strain at room temperature, but a much higher modulus and lower ultimate strain at 4 K, about 0.4%. The filled epoxy B has the highest modulus, but a relatively low ultimate strain, 0.32% at 4 K. The low-viscosity epoxy C has a low modulus at 4 K, but the highest ultimate strain, about 0.8% at 4 K.

Note the substantial change in properties of flexibilized epoxy A on cooling to 4 K. At liquid helium temperature, its elongation is no better than the filled epoxy B. By contrast, the low-viscosity epoxy C has, by far, the greatest elongation at 4 K. The comparative differences in elongation at 4 K are the most important property for the purposes of this study.

Table 3-1-1. Epoxy Properties

Epoxy	Temperature, K	Young's modulus, GPa	Ultimate strength, MPa	Ultimate strain, %
A	4	8 (CV = 17%)*	30 (CV = 14%)	0.4 (CV = 27%)
B	4	24 (CV = 4%)	80 (CV = 11%)	0.32 (CV = 7%)
C	4	8 (CV = 13%)	60 (CV = 21%)	0.8 (CV = 12%)
A	295	3	25	0.6
B	295	13	40	0.32
C	295	4	34	0.8

*CV = coefficient of variation among test specimens.

3.1.3 Composite Ring Tests

Ring Specimens and Test Apparatus. Several superconducting composite rings were fabricated using each of these epoxies. Approximately 150 turns of copper-stabilized NbTi (1.8:1 copper-superconductor ratio) were wound into rings 15 cm in diameter, 1 cm thick by 1 cm high. Fiberglass cloth was used to separate each layer of superconducting wire. A cross-sectional view of the final ring structure is shown in Fig. 3-1-1. For epoxies A and B, the rings were potted as they were wound, using a wet layup technique. Rings made with the low-viscosity epoxy C were vacuum impregnated after winding.

To stimulate the hoop stress that would be generated in an actual magnet solenoid, a split-D fixture was used to apply stress to the ring, as shown schematically in Fig. 3-1-2. With this arrangement, the stress is concentrated in the gap region between the two D's and, unfortunately, a significant amount of bending strain is also introduced. To better simulate the actual hoop stress in a magnet, a multifingered-cone and magnet arrangement is now being developed. Nevertheless, tests with the simplified apparatus have served to give comparative results among the different epoxy types, although the relative strain values indicated below should not be taken to represent absolute hoop strain. Strain was calculated from measurements of D separation using an extensometer. These calculated values were also correlated with strain measured directly with gages attached to various sections of the ring. The strain values given in this paper represent the maximum combined hoop strain and bending strain occurring in the ring.

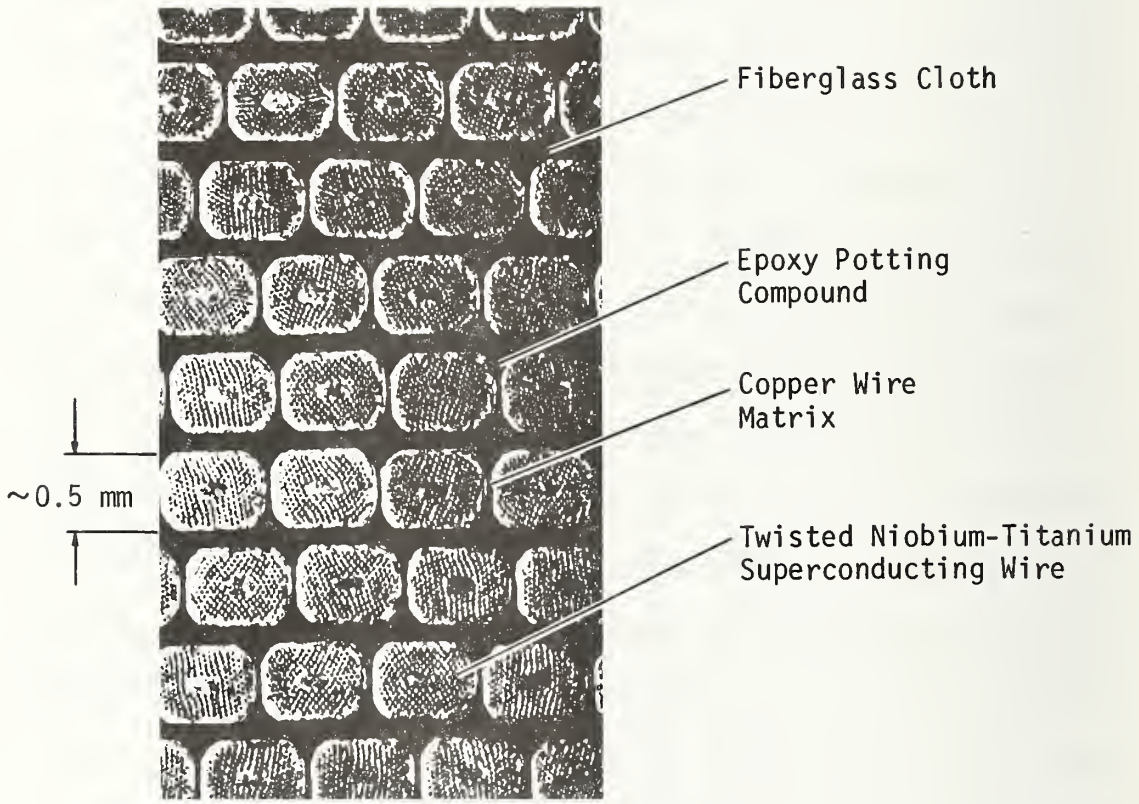

Fig. 3-1-1 Cross-sectional view of a superconducting composite ring showing its components.

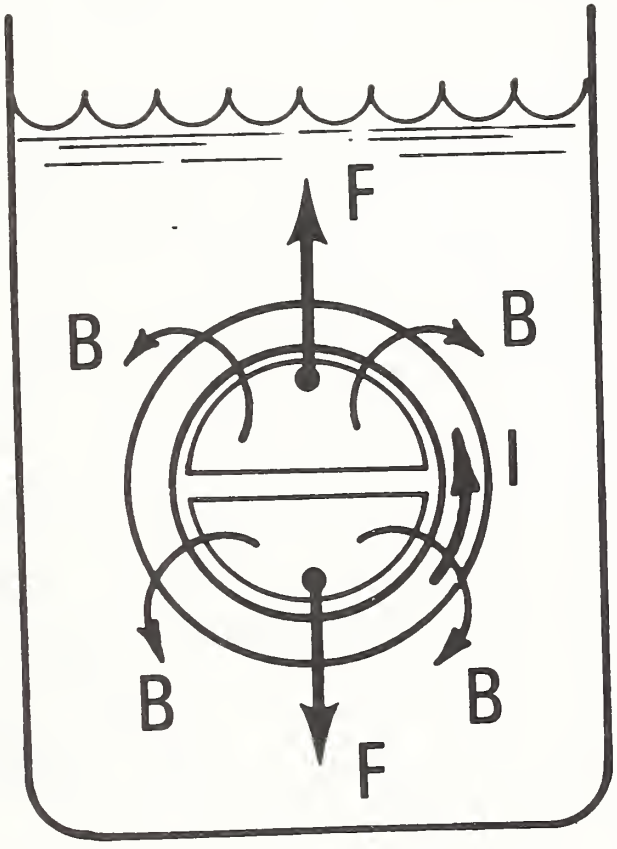

Fig. 3-1-2 Schematic of the ring test setup showing the configuration of force, F, applied to the D's, current I, applied to the superconducting ring, and the resulting self-field B, calculated to be about 3 T at maximum current.

Composite Ring Results. While under strain, each ring was energized with current until it quenched. At constant strain, the quench current kept increasing until it reached an ultimate value, i.e., the ring "trained". The number of quenches it took to reach the ultimate current is shown in Fig. 3-1-3.

What causes training? We suggest that a dominant cause of the training process in potted magnets may be associated with localized fracture of the epoxy impregnant, as follows: When the coil is energized, the magnetic hoop stress on the coil increases. This charging process continues until a failure of the epoxy occurs in the region of stress concentration sufficiently large to initiate thermal runaway. However, the net result is that the stress concentration in the epoxy is relieved, and the next time the coil is energized, it can withstand a higher hoop stress, allowing the coil to go to a higher current. This process continues until the highest levels of stress concentration are all relieved, or the superconducting wire reaches its short-specimen critical current.

As may be seen from Fig. 3-1-3, all three epoxies showed little or no training initially, but all trained to varying degrees at high strain. The training in rings impregnated with epoxies A and B was more severe, in correlation with their relatively low ultimate strain. In contrast, the ring made with epoxy C showed significantly less training, consistent with its much higher strain tolerance and the training mechanism described above.

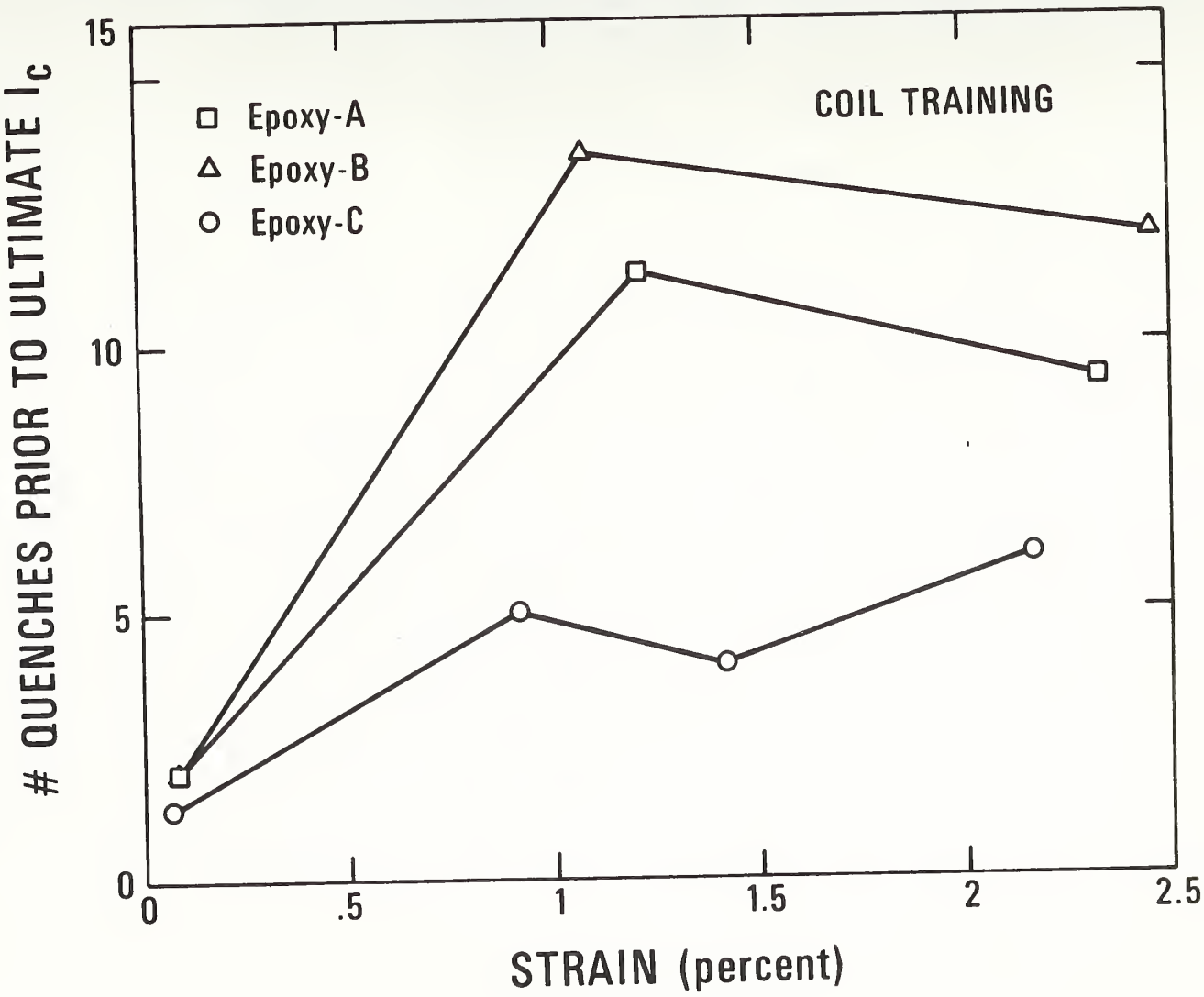

Fig. 3-1-3 Training behavior of each ring type as a function of applied strain.

The ultimate critical current reached after training is plotted for each ring type in Fig. 3-1-4. The critical current degradation shown in Fig. 3-1-4 is mainly a function of the localized strain in the superconducting wire rather than the epoxy. Recently, it was shown in a separate study on nonpotted NbTi wire specimens[4] that the critical current of NbTi will begin to degrade significantly at about 1% strain. This effect is aggravated, however, by cracks in the epoxy, which lead to localized strain in the superconductor. It is seen in Fig. 3-1-4 that the critical-current degradation is most pronounced in the composite rings potted with epoxies A and B, again correlating with the lower strain tolerance of these epoxies compared with epoxy C.

The method of epoxy impregnation may also be playing a role in both these results. Rings potted with epoxies A and B were fabricated using a wet layup technique. The ring made with epoxy C was made using a vacuum-impregnated technique. Voids introduced by the wet layup technique may well serve as crack initiation sites, leading to even lower strain tolerance of epoxies A and B.

3.1.4 Conclusions. These preliminary data indicate that the training process in potted superconducting magnets is associated with a succession of stress-concentration relief in the epoxy impregnant. The elongation of the epoxy at 4 K and the method of impregnation appear to be key factors controlling training.

Acknowledgments

We are grateful to American Magnetics, Inc. and to M. J. Superczynski and F. E. McDonald of the Naval Ship Research and Development Center

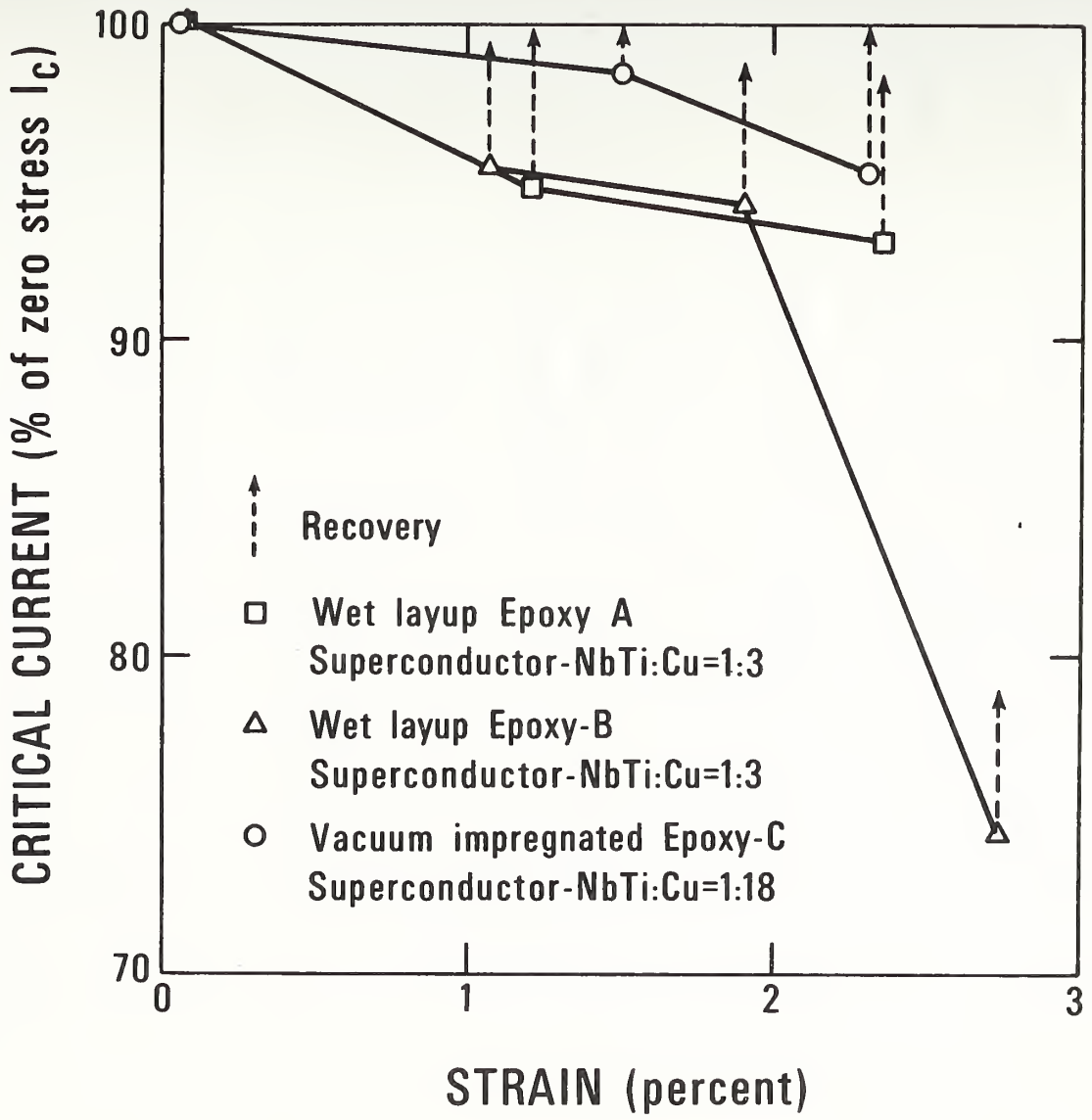

Fig. 3-1-4 Critical-current degradation of each ring type as a function of applied strain.

for fabricating the superconducting composite rings tested in this study. We wish to particularly than M. J. Superczynski for his suggestions and helpful discussions relating to these results.

References

1. "Tensile Properties of Plastics", Annual Book of ASTM Standards, Part 35, ASTM D638-76, American Society for Testing and Materials, Philadelphia, Pennsylvania (1977), p. 215.
2. "Conditioning Plastics and Electrical Insulating Materials for Testing", Annual Book of ASTM Standards, Part 35, ASTM D618-61, American Society for Testing and Materials, Philadelphia, Pennsylvania (1977), p. 198.
3. R. P. Reed, in: Advances in Cryogenic Engineering, Vol. 7, Plenum Press, New York (1962), p. 448.
4. J. W. Ekin, F. R. Fickett, and A. F. Clark, in: Advances in Cryogenic Engineering, Vol. 22 (Proc. Int. Cryogenic Materials Conf., Kingston, Ontario, Canada, 1975), Plenum Press, New York (1977), p. 449.

3.2 YOUNG'S MODULUS OF COMPOSITE COIL MATERIALS

by D. T. Read and A. F. Clark

3.2.1 Introduction

Using the acoustic resonance technique described in the second report[1] the Young's moduli were determined for the various coil composites tested in the previous section. Samples were sectioned from actual coils and, therefore, contained curved wire segments. The effect of the curvature was assessed by measuring two different lengths and also comparing to one specimen from an intentionally straight segment manufactured in an identical manner. These values can then be compared to the measurements reported earlier for the coil composite[1] and to calculated values to assure repeatability in the ring structures.

3.2.2 Specimens

Listed in Table 3-2-1 are the various specimens measured, their source, size, epoxy, and measured density. All were made with a similar copper-stabilized NbTi wire with a copper-to-superconductor ratio of 1.8:1. The wire in the A and B specimens was slightly larger. The various epoxy formulations are listed in the prior section (3.1). All specimens had the ends ground flat and their lengths were measured with a precision micrometer. Densities were measured by a water displacement method.

3.2.3 Results and Discussion

The values for the Young's modulus, E, are given in Table 3-2-1 and are accurate to $\pm$ 5% overall. The densities are estimated to be accurate to $\pm$ 1%. Since these measured E values were so close to what

Table 3-2-1 Acoustic Modulus Specimen Characterizations

Specimen	Material and Source	Length (cm)	Density (g/cm^3)	Young's Modulus (GPa)
A2 A5	Coil composite, epoxy A, wet layup, cut from ring.	1.99 5.07	5.90 5.90	74.0 75.4
B2 B5	Coil composite, epoxy B, wet layup, cut from ring.	2.02 4.77	5.77 5.77	78.2 79.4
C2R	Coil composite, epoxy C, vacuum impregnated, cut from ring.	2.02	6.06	83.9
C2S	Coil composite, epoxy C, vacuum impregnated, cut from straight specimen.	1.94	6.00	81.5
	(Static measurement in straight specimen, see Ref. 1)	----	----	(75.8)
WAB	Cu/NbTi wire used with A and B epoxy coils.	----	8.3 (est)	114.
WC	Cu/NbTi wire used with C epoxy coils.	----	8.3 (est)	113.
EFG	Epoxy/fiberglass, epoxy C, vacuum impregnated, without wires (see Ref. 1).	----	1.93	31.

was reported earlier[1], it was decided unnecessary to measure any other elastic constants or any of their temperature dependences. Everything could be scaled against the prior values and these were used for comparison only.

The differences in apparent E values between the 2 cm and 5 cm specimens are about 5%. This is attributed to the effects of the curvatures of the wires; the shorter, and thus straighter, specimens having the higher values.

The velocity of a Young's modulus wave in the composite Cu/NbTi wire used in the A and B epoxy bonded specimens was measured to be 3.71×10^5 cm/sec. The velocity of sound in the Cu/NbTi wire in the C specimens was measured to be 3.69×10^6 cm/sec. Estimating the density of these materials at 8.3 gm/cm^3 gives a Young's modulus of $E_{wire} = \rho v^2 = 114$ GPa at room temperature. The polycrystalline Young's modulus of copper at room temperature is 123 GPa. The value of E obtained for the composite wire is within 7% of this and is considered reasonable agreement.

Applying a law of mixtures, the estimated density for the wire (8.3 g/cm^3) and the density of epoxy (1.93 g/cm^3) we have for a volume fraction of epoxy, α,

$$(1 - \alpha)8.3 + \alpha\,(1.93) = 5.9$$

$$\alpha[1.93 - 83] = 5.9 - 8.3$$

$$\alpha = .377$$

Applying a simple law of mixtures to the modulus, we have

$$E_{calc} = .623 \times E_{wire} + .377 \times E_{fg\text{-}ep}$$

Using the wire modulus above and the measured modulus of the epoxy-fiberglass (31 GPa)[1] we have

$$E_{calc} = 83 \text{ GPa}$$

This is within 1% of the measured value for C specimens and also agrees well with the static value of

$$E_{static} = 75.8 \text{ GPa}^{1}$$

3.2.4 Summary

The Young's modulus, E, was measured using dynamic techniques at 300 K in a total of 6 specimens of 3 different types of copper-niobium-titanium/epoxy-fiberglass composite in both the copper-niobium-titanium wires, and in one fiberglass-epoxy without wires. The values are shown in Table 3-2-1. The uncertainties are possibly effects of the curvature of the wires within the specimens and the nonuniformity of the cross section due to differences in manufacture and machining. The values of E obtained are in good agreement with the value calculated using a simple law of mixtures and the values of the moduli of the components of the composite. They also agree well with values determined by conventional static techniques. Thus, the dynamic technique can readily be used for coil composite materials, simple laws of mixtures do apply, and the modulus behavior of one system can be extrapolated to others.

References

1. Clark, A. f., Weston, W. F., Arp, V. D., Hust, J. G., and Trapani, R. J., "Characterization of a coil composite and its constituents", NBSIR 76-837, Nat. Bur. Stds., Boulder, CO (1976), p. 53.

4. CONDUCTORS

4.1 LOW TEMPERATURE TENSILE BEHAVIOR OF COPPER-STABILIZED NIOBIUM-TITANIUM SUPERCONDUCTING WIRE

by R. P. Reed, R. P. Mikesell, and A. F. Clark

4.1.1 Introduction

The main component of each superconductivity application is the superconducting element. For most large-scale applications, such as electrical machinery, thermonuclear fusion and energy storage, this basic element is a multifilamentary wire usually wound into a solenoid. These superconducting solenoids are complex composites exposed to mechanical stresses, magnetic fields, and thermal gradients. Mechanical stresses are imposed by the preloading of the wire during winding, by thermal gradients and component thermal expansion differences during cooldown, and by the composite magnetic field. Reaction of the superconducting wire to mechanical stresses at the magnetic operating temperature must be known to insure optimum design and efficient and successful long-time operation of the superconducting application.

There have been few measurements of the mechanical properties of niobium-based superconductors at 4 K. Fox and Pryle[1] examined the tensile behavior of unstabilized monofilaments of Nb-25 wt.% Zr wire at 298, 77 and 4 K. They reported extremely good properties at 4 K for the 0.0125 and 0.025 cm diameter wire specimens: tensile strengths from 28×10^8 N/m^2 (420,000 psi) to 45×10^8 N/m^2 (640,000 psi). These wires had insufficient elongation over the entire specimen length at 4 K to record a yield strength but exhibited between 20 and 50% elongation at 298 K. Brechna[2] presents one figure that includes the stress-

strain curves of Nb-43 wt.% Ti wire (0.0625 cm diameter) at 4 K and a Cu-Nb/Ti (10 to 1 ratio) composite wire at 300 K. Cornish[3] measured the stress-strain behavior of Nb-Ti core, copper-stabilized wire at 77 K and found good tensile strength (5.3×10^8 N/m^2, 80,000 psi) considering that the copper-superconductor volume ratio was 2.74. Finally, Evans[4] briefly reported several stress-strain curves measured using a clamp-on extensometer at 4 K of both Nb-Ti, twisted, multifilamentary wire and Nb-Ti filaments. These stress-strain curves had numerous sudden load drops, which were interpreted as discontinuous yielding caused by local, adiabatic heating of the specimen. However, these curves had no strain associated with the load drops, leading one to suggest that the load drops originated in the gripping area, rather than in the gauge length monitored by the extensometer.

As one part of a systematic evaluation of a particular superconducting coil,[5] the tensile behavior has been measured at 298, 76, and 4 K of its superconducting wire, the Nb-Ti filaments contained in the superconducting wire, and copper wire given the same thermal and mechanical treatments as the stabilizing copper of the superconducting wire. For this application, a prototype dc motor for marine propulsion, the wire is wound into a coil and then vacuum impregnated with epoxy. The mechanical behavior of the wire is used to program the winding tension properly, to correlate with the electrical degradation,[6] and to predict the stress limits for system operation.

4.1.2 Materials

The superconducting wire composite consists of 180 filaments (0.032 mm diameter, twisted, 0.8 twists/cm) of 55 wt.% (38 at.%) Nb-45 wt.%

(62 at.%) Ti stabilized by oxygen-free, high-conductivity copper (Fig. 4-1-1). The volume ratio of copper to superconductor is 1.8 and the wire cross section is rectangular with dimensions of 0.07 x 0.055 cm.

To best approximate the expected copper properties in the superconducting wire a specially worked and heat-treated oxygen-free copper wire was supplied by the American Metals Climax, Inc. This copper wire had been sequentially hot rolled at 1123 K to 0.6 cm diameter rod, annealed at 1123 K for 0.5 hr, water quenched, cold drawn to 0.2 cm wire, annealed at 773 K for 0.5 hr, water quenched, cold drawn to 0.07 cm diameter wire, and finally annealed at 573 K for 1 hr. Its chemical analysis was, in parts per million, 14Ag, 3Fe, < 3As, 2Sb, 6Pb, 4P, 11S, 0.7Bi, < 2Te, < 2Sn, < 1Zn, 4Ni, < 1Cd, and 0.4Mn. Its residual resistance ratio was reduced from 210 (AMAX data) to 146 (measured at 4 K at NBS) by the sequential treatment listed above. Microhardness measurements produced a DPH hardness number of 70 with variations of $\pm$ 10 (2 g load) and the average grain diameter was 0.011 mm.

The copper-stabilizing material in the superconducting wire was cold worked in the final condition, after receiving approximately the same sequential mechanical and thermal treatments as the copper wire. The average hardness of the copper in the superconducting wire was DPH 98 (2 g load) with variation of $\pm$ 20, the residual resistance ratio was 64, and the average grain size was 0.017 mm.

The hardness of annealed, high-conductivity copper in bulk form is DPH 65 $\pm$ 5, using a 2 g load. Comparatively, the copper wire has a slightly higher hardness (DPH 70, 2 g load) and a spread of $\pm$ 10, while the copper of the superconducting wire has the highest hardness (DPH 98, 2 g load) and greatest spread of ($\pm$ 20). This corresponds

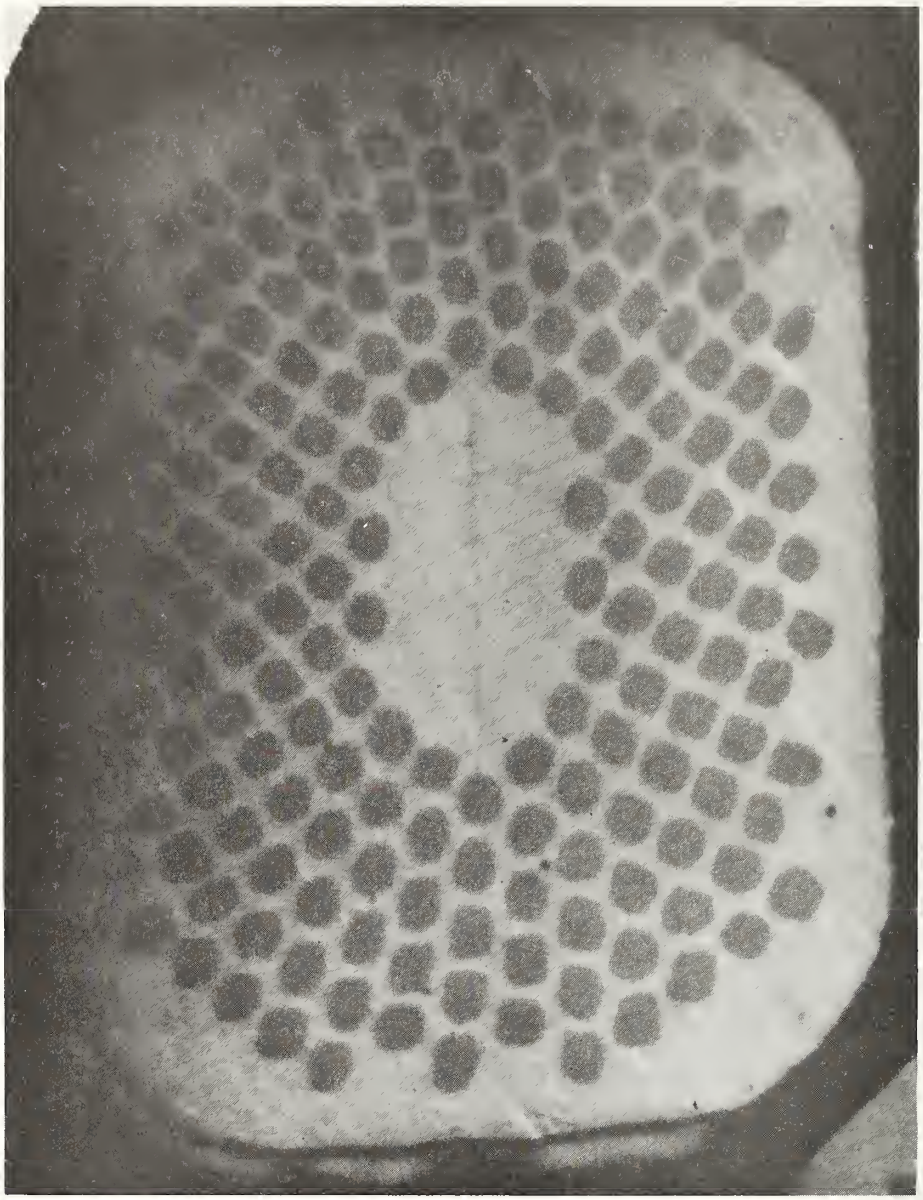

Fig. 4-1-1 Photomicrograph of the multifilamentary superconducting wire containing 180 filaments and a copper to conductor (Nb-Ti) ratio of 1.8 to 1.0.

well with the residual resistance ratios of 210 for annealed copper, 146 for copper wire, and 64 for the copper of the superconducting wire composite.

The Nb-Ti filament specimens were prepared by chemically removing the copper from the superconducting wire. The desired length of wire was immersed in dilute nitric acid for 2 hr to etch away all copper. No attack of the Nb-Ti filaments by the dilute nitric acid was detected. All strands (180), remaining twisted, were then used as the specimen. Each filament diameter remained at 0.0322 mm.

The wire composite is coated with formvar insulation, a polyvinyl formal resin. Low-temperature tensile tests with this coating remaining on the wire produced load-time curves that resembled discontinuous yielding curves. The load drops did not occur within the specimen gauge length since no associated strain, as sensed by the strain gauge extensometer, was detected. Removal of the formvar coating using a commercial stripping solution, which attacked only the coating, produced load-time curves that had no load drops. Therefore, the load drops with the formvar on the wire are thought to result from the cracking of the formvar on the spool grips. Consequently, all reported data at all temperatures represent tests on specimens having their grip length uncoated, although from the limited comparative tests, no difference (other than the load drops) was found.

4.1.3 Procedures

Tensile measurements were performed using a commercial screw-driven tensile machine with a 4500 kg load capacity. Cryostat equipment has been described by Reed.[7] Commercial load cells of 45 kg capacity were

used. Strain was measured using conventional four-strain gauge extensometers, which were held to the wire specimens using spring tension on knife edges. These extensometers were able to sense plastic deformation over sufficient lengths to measure the total strain (0.01 to 0.04) of the wire composite and twisted Nb-Ti filaments, all within a gauge length of 2.5 cm. Approximately 10% elongation could be recorded for the copper wire specimens. At room temperature an elongation of 1% resulted in an output of approximately 5 mV. The sensitivity of the extensometer decreased about 1% betweeen 298 and 4 K. The extensometers were calibrated at 298, 76, and 4 K using a sensitive drum micrometer and overlapping, concentric extension arms that were immersed in the cryogens. Except where indicated, all cross-head speeds were 0.05 cm/min, resulting in specimen strain rates during plastic deformation of about 0.004/min. All tests were conducted in air (298 K), liquid nitrogen (76 K), and liquid helium (4 K). At least four composite and copper specimens and two Nb-Ti twisted filament specimens were measured at each temperature.

Specimens were gripped as illustrated in Fig. 4-1-2. Two wire segments carried the load and attached to each segment was one extensometer beam. In the upper spool care was taken in the winding to ensure no wire overlap. Wire overlap in the grip areas tended to promote erratic load drops when testing at low temperatures. The arrangement produced well-aligned loading and the fractures occurred randomly along the spool loading areas and along the open wire lengths. The recorded strain output was the average of the independent flexing of both extensometer beams.

Microhardness of the three types of copper specimens was measured using a standard microhardness machine. A 2 g load, small enough to

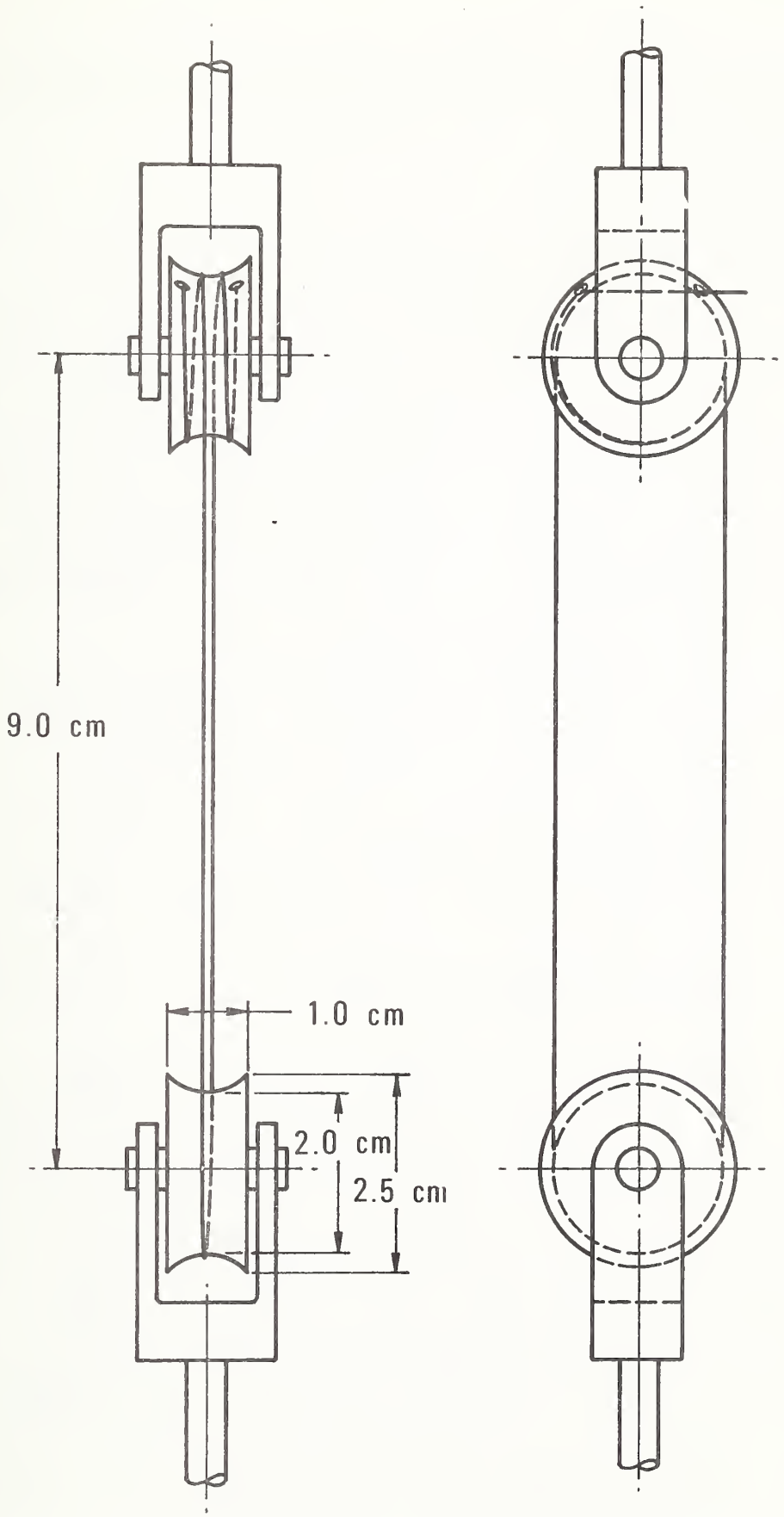

Fig. 4-1-2 Loading assembly for the wire specimens.

prevent impingement of the indenter on the Nb-Ti filaments, and a diamond pyramid indenter were used.

4.1.4 Results and Discussion

Hardness. The condition of the copper-stabilizing material in the rectangular wire was rather nonuniform. This is indicated by the relatively large variation of hardness of the copper found along the wire length. This large variation suggests variations in composite properties. In practice, such large variations in composite yield or tensile strength were not found. This implies that considerable "averaging" occurs along the wire length during deformation; however, the tensile strength may reflect fracture in the softer areas.

Young's Modulus. Using the Nb-Ti twisted filaments and oxygen-free copper data, one can predict their composite Young's modulus (E) values knowing the volume ratio (1.8 part Cu, X_{Cu}, to 1 part Nb-Ti, $X_{Nb\text{-}Ti}$) and using the law of mixtures relationship,

$$E_{comp} = \frac{X_{Cu}E_{Cu} + X_{Nb\text{-}Ti}E_{Nb\text{-}Ti}}{X_{Cu} + X_{Nb\text{-}Ti}} \qquad (1)$$

Two possible effects may contribute to a lower wire modulus, compared to the bulk modulus of the Cu and Nb-Ti components: (1) the predominance of <100> copper texture in wire after small increments of plastic deformation, and (2) the reduction of E from defect generation during plastic deformation. Young's modulus of annealed copper crystals, pulled along <100>, is relatively low, a typical room temperature value[8,9] being about 7.6 x 10^{10} N/m^2. Other crystal orientations measured by Cuykendall and Sack[10] had larger values of E ranging from 15.8 to 20 x 10^{10} N/m^2. Soliman

et al.[11] and Yeomens[12] have indicated that a <100> texture is observed after small plastic strain increments in copper. This texture gradually shifts to half <100> and half <111> at larger strains.[12] Low-temperature (400 to 800 K) annealing was not found to change the wire microstructure significantly.[10] Therefore, since the wire composite was strained and finally annealed at low temperatures, it is probable that a <100> texture does predominate and may contribute to a low value of E.

Concurrent with the change of crystal orientation, the presence of lattice defects is known slightly to decrease elastic constants (see Ledbetter and Naimon[8] for specific references). Excessive defects, generated during the composite forming process and not entirely removed by the low-temperature anneals, are known to be present; this is indicated by the high hardness and low residual resistance ratio of the copper.

The combination of preferred orientation and defects, usually found only wire specimens, provides low values of Young's modulus. Soliman et al.[11] measured minimum values of E at room temperature as a function of plastic deformation of from 5.5 to 6.8 x 10^{10} N/m^2 for copper wire. Unusually low values of E for bronze-multifilamentary Nb_3Sn wire have been reported by Old and Charlesworth[13], who found E for the composite to be lower than both the bulk Nb_3Sn and the bronze base elements.

Comparative elastic data for Nb-Ti and Cu, Nb-Ti composites are scarce. The values of E for Nb-45 wt.% Ti and Nb-48 wt.% Ti in bulk specimens at room temperature, as determined by Ledbetter[14], are 7.80 and 7.45 x 10^{10} N/m^2 (1.1 x 10^6 psi). The Young's modulus of bulk

copper at room temperature is about 12.5 to 13.0 x 10^{10} N/m^2 (18 x 10^6 psi)[8], although considerable data scatter has been reported.[8,9] The values of E at room temperature determined for Cu, Nb-Ti wire by Easton and Koch[15] range from 9.3 to 11.0 x 10^{10} N/m^2. The room temperature data for E of Cu, Nb-Ti wire, measured using the strain gauge extensometer in this study, range from 5.8 to 13.0 x 10^{10} N/m^2. Obviously the spread of values is too large and further research is continuing to separate material variability from experimental imprecision

Tensile Properties. The tensile properties of the twisted Nb-Ti filaments, the drawn copper wire, and the superconducting wire composite are summarized in Figs. 4-1-3 and 4-1-4. The tensile and yield strengths (0.2T offset) have no abnormalities as a function of temperature. The yield strength of Nb-Ti could not be determined since the filaments did not deform plastically 0.2%. Predicted values of the composite tensile strength, based on the mixture law, fall about 25% below the actual composite values; this discrepancy is thought to result from the harder condition of the copper in the composite, manufacture cold working subsequent to the 573 K anneal and is indicated by the hardness and residual resistivity measurements. There is little dependence of the yield strength of the wire composite on temperature.

The Nb-Ti multifilamentary composite is considerably weaker than the monofilaments of Nb-Zr[1] and Nb-Ti.[3] However, the room temperature multifilamentary Nb-Ti wire tensile properties compare favorably with the the properties of Nb_3Sn multifilamentary composite formed by tin diffusion into niobium filaments.[4] They also compare favorably to

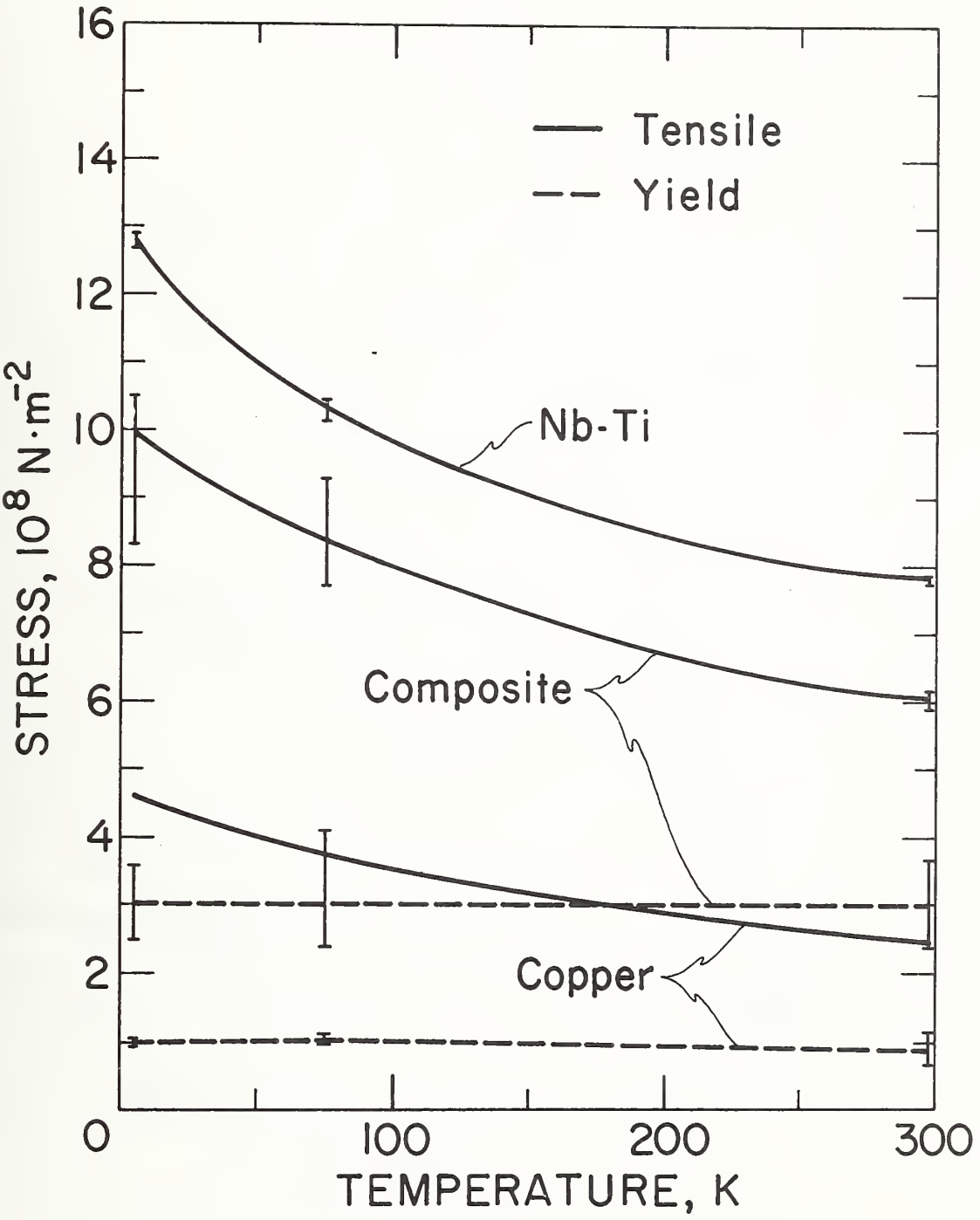

Fig. 4-1-3 Tensile and yield strengths as a function of temperature. Yield strength for Nb-Ti twisted filaments was unobtainable due to their small amount of plastic deformation ($0.689 - 10^4$ psi = N/m^2).

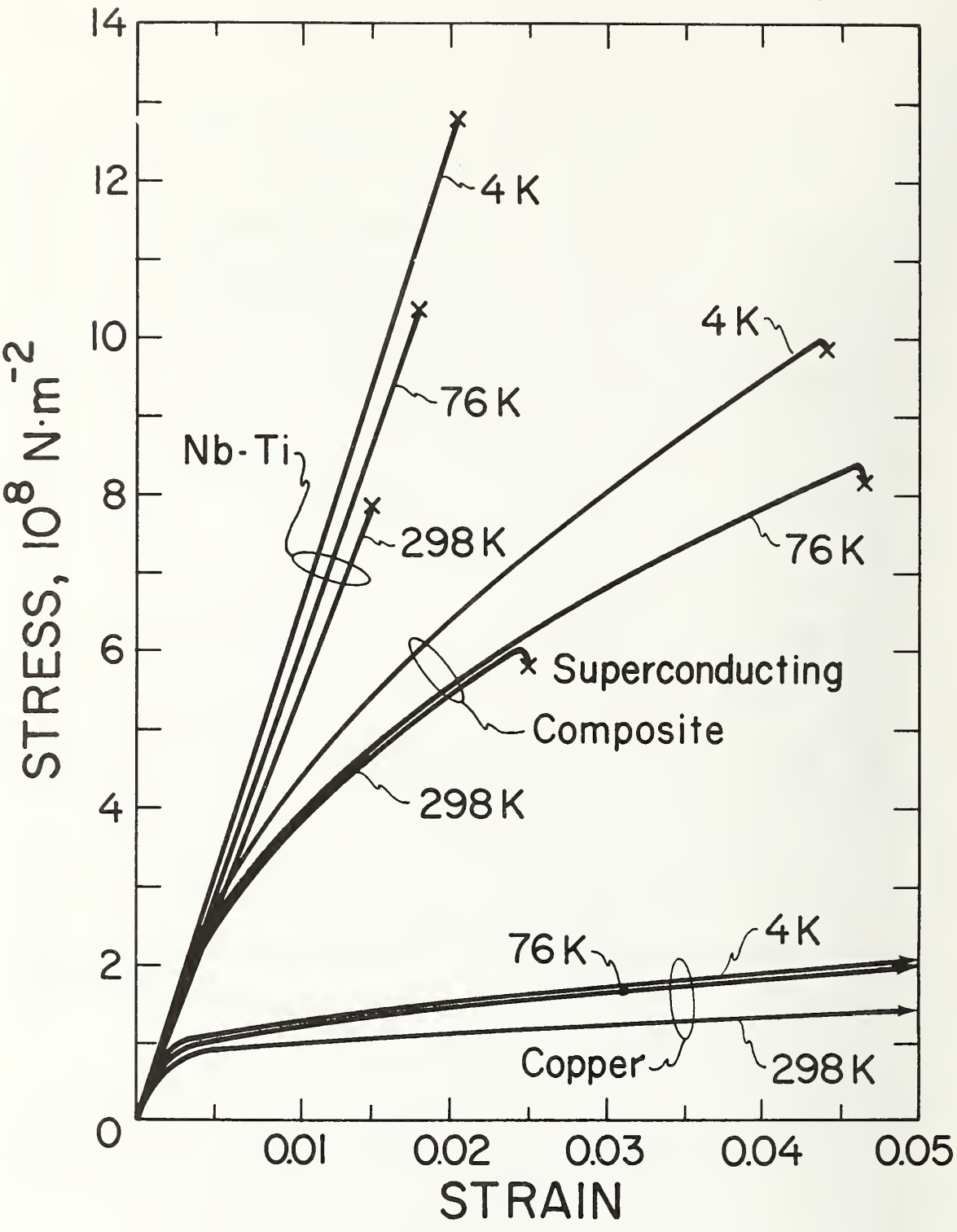

Fig. 4-1-4 Stress-strain curves at 298, 76, and 4 K (0.689×10^4 psi = N/m^2).

previous work at 77 K,[3] although the tensile values are somewhat higher as might be expected with a lower copper-to-superconductor ratio.

The stress-strain curves are presented in Fig. 4-1-4. Elongation to fracture, recorded using the clip-on, strain gage extensometers, can be obtained from these curves as the tensile strengths and strain to failure represent average values. The elongation to fracture was about twice as great at 76 and 4 K as compared to 298 K. Contrary to the findings of others,[4,8] no significant discontinuous yielding was observed in either the Nb-Ti or the wire composite. As mentioned earlier, prior to the adoption of the present test technique (removal of wire coating and no overlapping wire on the spools) load drops were commonly observed. Occasionally, with the present test technique an independent load drop was noticed on the load-time chart recordings, accompanied by an audible click. But, none of these sudden load decreases occurred within specimen gauge lengths, as associated strain increases were never recorded by the extensometer. This has led to the conclusion that, for this wire, all load discontinuities occurred in the grip area. Very little plastic deformation of the Nb-Ti filaments was observed; this implies that adiabatic heating cannot be a major influence on the filament deformation processes. The appearance of discontinuous yielding in a superconductor wire deformed at 4 K is a sufficient, but not a necessary, condition for plastic deformation-induced adiabatic heating to induce training effects in solenoids. Discontinuous yielding requires both large temperature rises and a steep temperature dependence of the superconductor flow stress. It is very unlikely that large temperature rises will occur in the Nb-Ti filaments since very little plastic deformation of the filaments

occurs and also because these filaments are surrounded by copper, a good thermal conductor.

The influence of strain rate on the tensile properties at 4 K of the wire composite is shown in Fig. 4-1-5. The 4 K tensile strength is essentially independent of strain rate, while there is a slight increase of yield strength with increasing rate of loading. The largest strain rate effect is the dependence of elongation; fracture of the composite occurs at decreasing values of plastic deformation as the rate of loading is increased. Even at high strain rates, no discontinuous yielding was observed in this conductor, leading one to speculate that local, adiabatic heating conditions are not the cause of irregular yielding reported to occur in the specimens of Evans[4] and Easton and Koch.[8]

Finally, hysteresis of the stress-strain curve during sequential specimen loading to the plastic deformation range and unloading to zero load was examined. Specimens were loaded, unloaded, and then loaded to a higher stress; this process was continued for 4 to 6 cycles per specimen at 4 K. A measure of these effects can be estimated from the parameter $(\varepsilon_2 - \varepsilon_1)/\varepsilon_2$, where ε_2 is the strain difference at one-half the maximum stress and ε_1 the strain difference at zero stress. A high value of $(\varepsilon_2 - \varepsilon_1)/\varepsilon_2$ indicates substantial recovery, while a zero value indicates perfect elastic behavior. The parameter $(\varepsilon_2 - \varepsilon_1)/\varepsilon_2$ is plotted vs. the maximum applied stress in Fig. 4-1-6 and is shown to increase steadily with applied stress. Sizable data scatter is observed. Continuation of the cycling process to the same maximum load (fatigue) produces decreased values of ε_2 (corresponding to a decrease in Young's modulus), but sufficient testing has not been completed to document adequately the effect on ε_1.

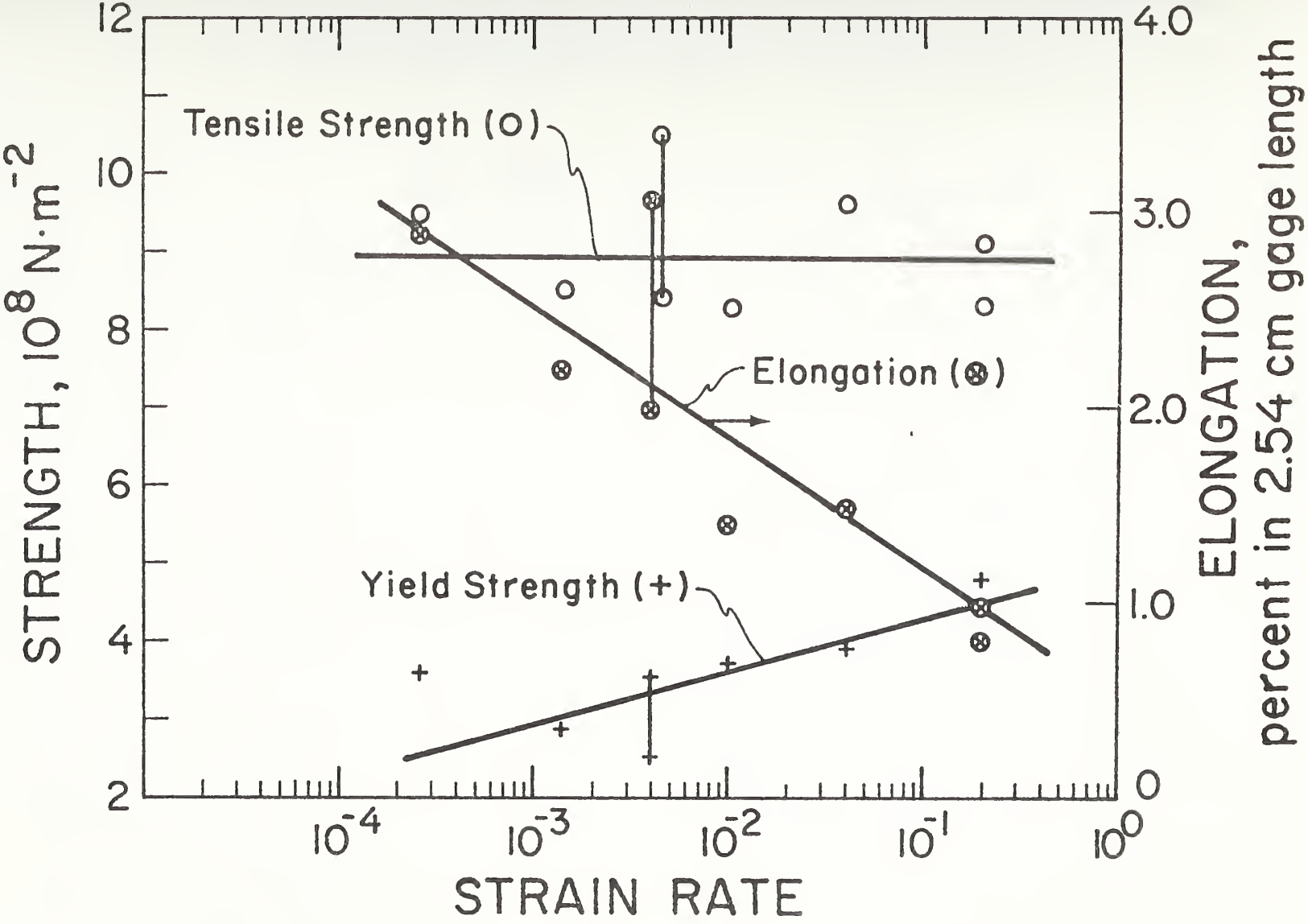

Fig. 4-1-5 The effect of strain rate on tensile properties. All data were obtained at 4 K. Brackets represent spread of data presented in Fig. 4-1-4/

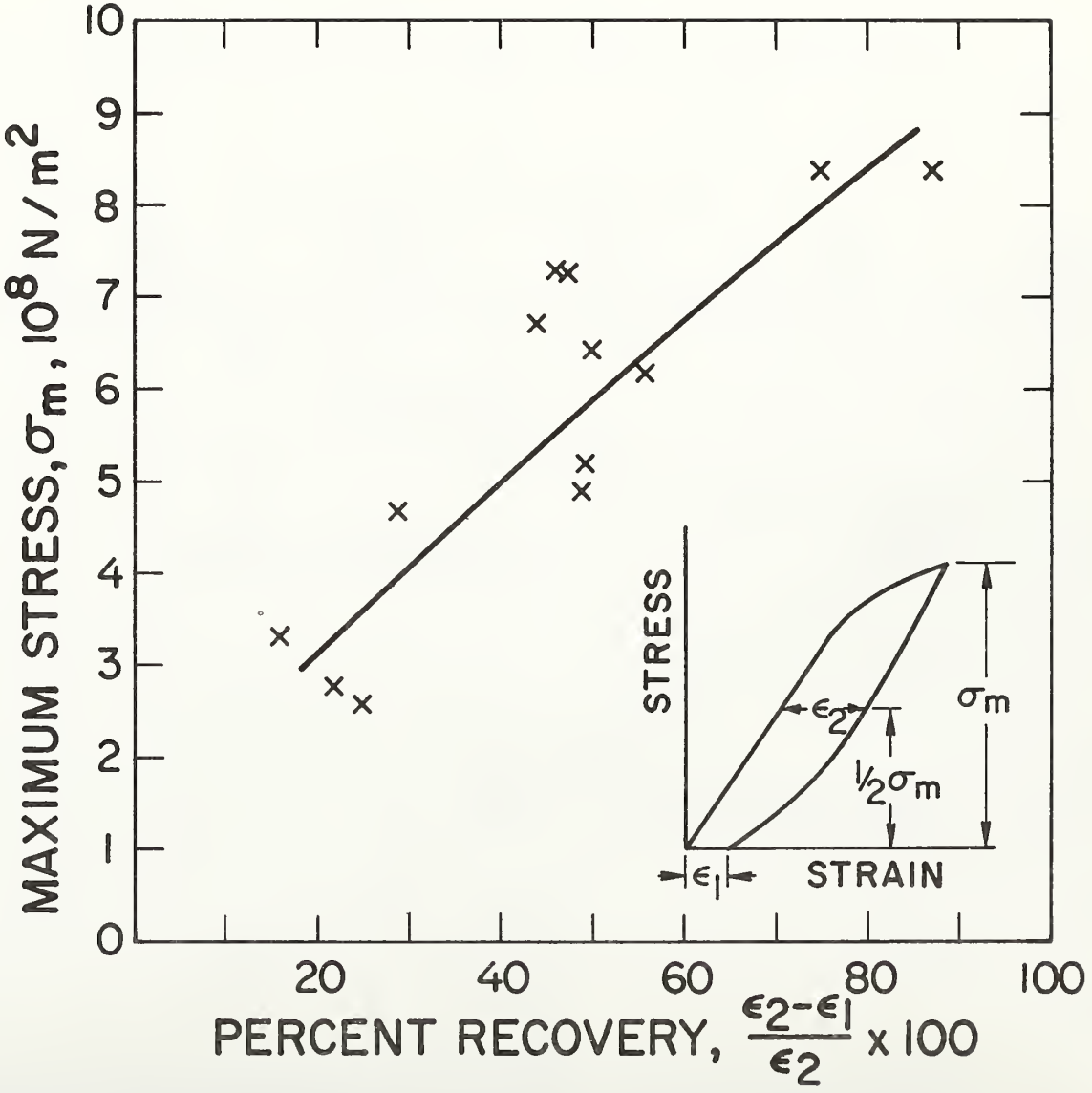

Fig. 4-1-6 Anelastic recovery of multifilamentary superconducting wire as a function of maximum applied stress.

4.1.5 Summary

In brief, the following comments summarize this study of the stress-strain behavior of one twisted multifilamentary, copper-stabilized, Nb-Ti superconducting wire.

The tensile and yield strengths of the Nb-Ti, copper, and wire composite are well behaved from 4 to 300 K. The Nb-Ti has very little plastic deformation, signifying that little adiabatic heating can take place in the superconducting filaments prior to fracture. No discontinuous yielding was observed at 4 K. The yield strength was found to increase slightly with increasing strain rate and the elongation to decrease with increasing strain rate, both measured at 4 K.

Anelastic unloading behavior was observed by the wire composite at 4 K. The degree of recovery was dependent on the maximum applied stress.

Acknowledgments

The authors would like to acknowledge the helpful assistance of R. L. Durcholz and R. J. Trapani.

References

1. D. K. Fox and W. H. Pryle, in: Advances in Cryogenic Engineering, Vol. 9, Plenum Press, New York (1963), p. 124.
2. H. Brechna, in: Superconducting Magnet Systems, Springer-Verlag, Munich (1974), p. 413.
3. D. N. Cornish, in: Proceedings Intern. Conference on Magnet Technology, Ther Rutherford Laboratory, Oxford, England (1967), p. 507.
4. D. Evans, "An Hypothesis Concerning the Training Phenomenon Observed in Superconducting Magnets," RL-73-092, Rutherford Lab., Harwell, England (August 1973).

5. C. W. Fowlkes, P. E. Angerhofer, R. N. Newton, and A. F. Clark, "Characterization of a Superconducting Coil Composite," NBS-IR-73-349, National Bureau of Standards, Boulder, Colorado (Dec. 1973).

6. J. W. Ekin, F. R. Fickett, and A. F. Clark, in: Advances in Cryogenic Engineering, Vol. 22, Plenum Press, New York (1976), p. 449.

7. R. P. Reed, in: Advances in Cryogenic Engineering, Vol. 7, Plenum Press, New York (1961), p. 448.

8. H. M. Ledbetter and E. R. Naimon, J. Phys. Chem. Ref. Data 3(4):897 (1974).

9. R. P. Reed and R. P. Mikesell, "Low Temperature Properties of Copper and Copper Alloys," NBS Monograph 101, U.S. Govt. Printing Office, Washington, D.C. (1967).

10. T. R. Cuykendall and H. S. Sack, "Dynamic Elastic Properties of Solids," PB 121701, NTIS, Springfield, Virginia (1955).

11. M. R. Soliman, T. H. Youssef, and R. A. Essawi, Indian J. Phys. 45:77 (1971).

12. D. D. Yeomans, J. Inst. Metals 82:653 (1953).

13. C. F. Old and J. P. Charlesworth, "Some Tensile Properties of Multi-filamentary Nb_3Sn Superconductors," AERE-R 7903, AERE Harwell, England (December 1974).

14. H. M. Ledbetter, National Bureau of Standards, Boulder, Colorado, private communication.

15. D. S. Easton and C. C. Koch, in: Advances in Cryogenic Engineering, Vol. 22, Plenum Press, New York, (1976), p. 453.

4.2 EFFECT OF STRAIN ON THE CRITICAL CURRENT OF COPPER-STABILIZED AND ALUMINUM-STABILIZED NbTi MULTIFILAMENTARY COMPOSITES

by J. W. Ekin

4.2.1 Introduction

Superconducting composites within large-scale magnets can be subjected to high stresses. These stresses arise from several sources, chief among them being the winding tension and prestressing during construction of the magnet, thermomechanical forces incurred during thermal cycling to cryogenic temperatures, and, especially in large-scale systems, magnetomechanical forces generated when the magnet is energized. These mechanisms can combine to exert large stresses on the superconducting composite, with magnitudes approaching a significant fraction of the ultimate strength of the wire itself [about 10^9 N/m^2 ($\sim$150 ksi) for NbTi:Cu composites].

Typically, data on the critical-current characteristics of superconducting composites are obtained on wires that are in an unstressed state. Very little is known, however, about how the critical current behaves in wires experiencing stresses of the type described above.[1] To measure these effects, short sample critical current tests were made under conditions simultaneously simulating the mechanical and magnetic environments of high-field superconducting magnets. The program was initiated both to form a basis for the fundamental understanding of strain effects on superconductor stability and to provide engineering data for optimizing design and construction of high-field magnets. As will be seen, the results show that multifilamentary superconducting

composite wires are not characterized by a single critical current vs. field curve, but rather by a family of curves, each corresponding to a different operating strain level.

4.2.2 Experimental Apparatus

Two types of apparatus were constructed for simultaneously applying current, tensile force and a perpendicular magnet field to short wire specimens at 4K. The first apparatus was designed for testing samples that can be bent to a radius less than 1.25 cm; the second for testing straight samples.

The first apparatus utilizes a 100 kOe simple solenoidal magnet with the sample in a hairpin geometry (shown schematically in Fig. 4-2-1). At the center of the magnet an approximately 2 m long wire sample is passed around a pair of 2.5 cm diameter, nonmagnetic, stainless steel rollers designed to provide a short straight section of the superconductor transverse to the maximum mangetic field. Voltage was detected along a 3 cm section of the wire perpendicular to the applied field at the center of the magnet. The wire ends were led out of the magnet bore, wrapped around a 3.8 cm diameter friction grip, anchored, and soldered to two 600 A current leads. Stress was applied to the wire using dead-weight loading. Strains were measured with a clip gauge over a 1.2 cm gauge length outside the magnet. Voltage across the perpendicular test section was measured with a sensitivity of 400 nV; current was determined to within 0.5%, magnetic field to within 0.1%, stress to within 1%, and strain to within 0.01%.

The second apparatus utilizes a 5 cm bore 7T split-pair superconducting magnet with 1.5 cm diameter radial access ports which per-

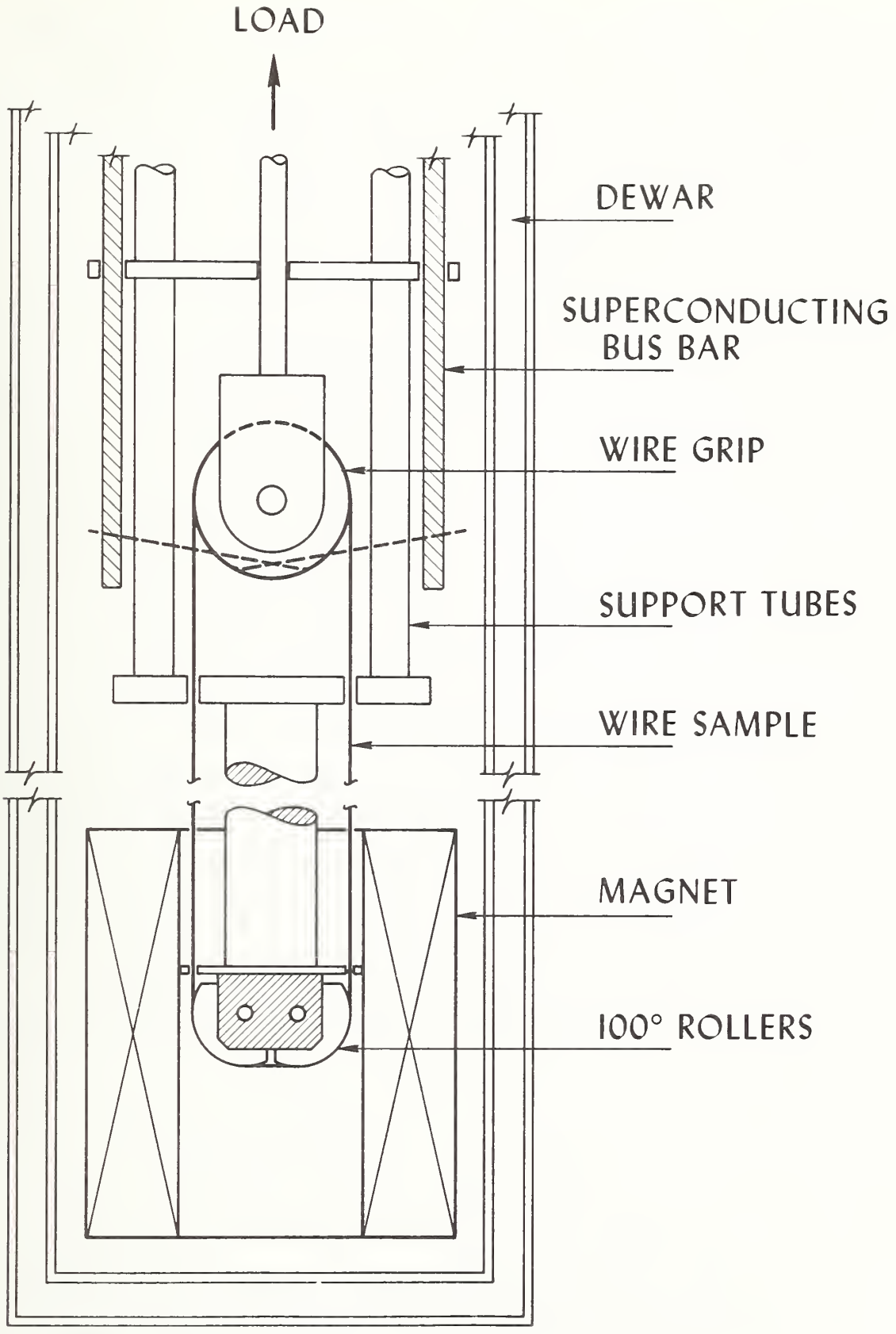

Fig. 4-2-1 Schematic diagram of the stress-I_c apparatus for testing hairpin samples.

mitted testing of long (35.5 cm) straight specimens (shown schematically in Fig. 4-2-2). The specimens were gripped at either end outside the magnetic field by soldering into copper sleeves attached to the load train through self-aligning universal joints. In fracture tests, the specimens did not break at the grips, but fractured at random points along the gauge length between the grips, indicating no stress concentration at the copper-solder grips. This arrangement also allowed the introduction of current directly through the grips. The solder grip length was 3.2 cm and the current-transfer length between each grip and the 4 cm center test section consisted of a ∿10 cm length in a linear magnetic field gradient and a 0.5 cm length at full field. These lengths are more than the theoretical minimum transfer length calculated from Appendix A.1 and A.2 and, experimentally, no current transfer effects were observed in the data (i.e., no finited slope to the V-I characteristics at low currents, and no heating at the grips). The critical current criterion used was 2 μV/cm unless otherwise stated, see Appendix A.3. Current was determined to within 0.5% and magnetic field to within 0.1%. Tensile load for this second apparatus was supplied by a servohydraulic system which was capable of either load, stroke, or strain control. Specimen strain was determined to within 0.01% and load to within ± 1 lb.

4.2.3 Procedure

After the wire is cooled to 4K, a small preload (≲5N) is applied. This serves the purpose of minimizing wire movement in the presence of the Lorentz force developed during testing. Critical current is determined by increasing the current through the wire until the voltage

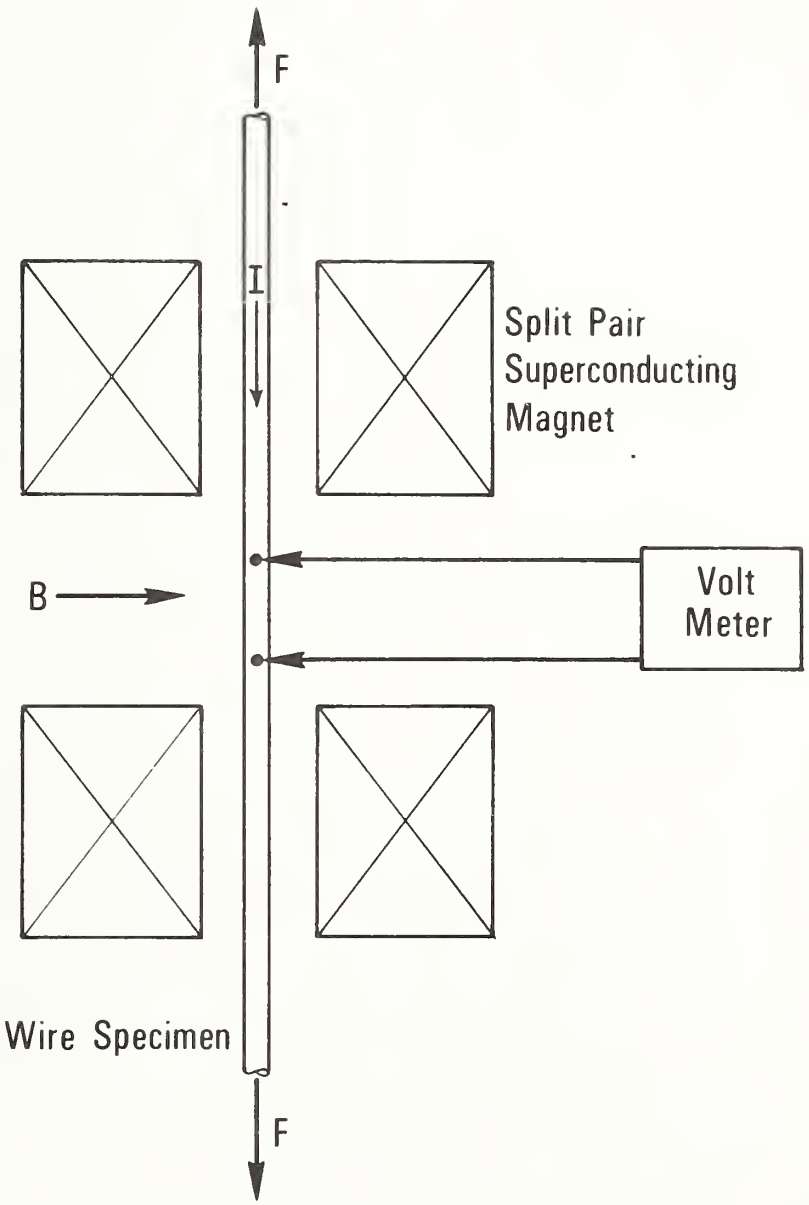

Fig. 4-2-2 Schematic diagram of the strain-I_c apparatus for testing straight samples.

across the transverse section of the sample starts to increase sharply and exceeds the critical-current criterion. This increase is extremely rapid and is reversible provided the voltage is not allowed to become too great. Monitoring this reversible rise in voltage also allows a distinction between the intrinsic critical current of the wire and irreversible premature quenches occasionally generated by wire movement.

The following measurement procedure was adopted. Initially the critical current I_c was determined as a function of the magnetic field H at the prestress level. For the first (second) apparatus, the load (strain) was then increased and maintained constant while the I_c vs. H characteristic was determined. This was followed by reducing the load to the prestress level and remeasuring the initial I_c vs. H characteristic before proceeding to still higher loads. Using this procedure, information was obtained on both the critical current degradation under load, as well as any recovery that had occurred after the load was reduced to the prestress level.

4.2.4 Results: NbTi-Copper

Unless otherwise noted, results are reported here for sample 1, a multifilamentary NbTi composite which consisted of 180 NbTi filaments in an "oxygen-free" copper matrix having an initial resistance ratio (R_{295K}/R_{9K}) of 70. Copper-to-superconductor ratio was 1 8:1 and the NbTi alloy was composed of 55 wt-% Ti and 45 wt-% Nb. Twist pitch was 1.3 cm and the overall wire dimensions were 0.53 x 0.68 mm. A crossectional view is shown in the top half of Fig. 4-2-3. The specifications are tabulated in Table 4-2-1; mechanical properties are described in Sec. 4.1.

A typical set of voltage-current characteristic for this conductor is shown in Fig. 4-2-4. Also shown in Fig. 4-2-4 are three dashed reference

Table 4-2-1. Sample Characteristics

Sample	Size	No. Fil	Fil. Diam	Fil. Twist Length	Composition
Copper Stabilized					
1 (NSRDC 4-2)	0.53 x 0.68 mm	180	30 μm	1.3 cm	36% Nb-55Ti 64% OFHC Copper
2 (NSRDC 1-9)	0.63 x 0.80 mm	120+		1.3 cm	36% Nb-50Ti 64% OFHC Copper
3 (Monofilament)	0.30 mm diam	1	0.254 mm		70% NbTi 30% Copper
Aluminum Stabilized					
4 (MCA)	.76 mm diam	180	35 μm	1.3 cm	38% NbTi 62% PDOF Copper
5 (Fermi Lab)	.70 mm diam	2046	9.2 μm	1.3 cm	36% NbTi 64% PDOF Copper
6 (Alcoa)	0.56 x 0.66 mm	54 tubes	69 μm O.D. 39 μm I.D.	1.3 cm	40% Nb-55Ti 17% 5-9 pure Al 43% 5056 Al alloy
7 (Alcoa)	0.56 x 0.64 mm	54 tubes	69 μm O.D. 39 μm I.D.	1.7 cm	46% Nb-55Ti 21% Cu 33% 5056 Al alloy
8 (NSRDC 14-3)	1.00 x 1.25 mm	6 x 54	43 μm		40% Nb-47Ti 17% 5-9 pure Al 43% 5056 Al alloy
9 (NSRDC 13-2)	0.89 mm	121		∞ cm	37% Nb-53Ti 18% 4-9 pure Al 45% 1100 Al alloy

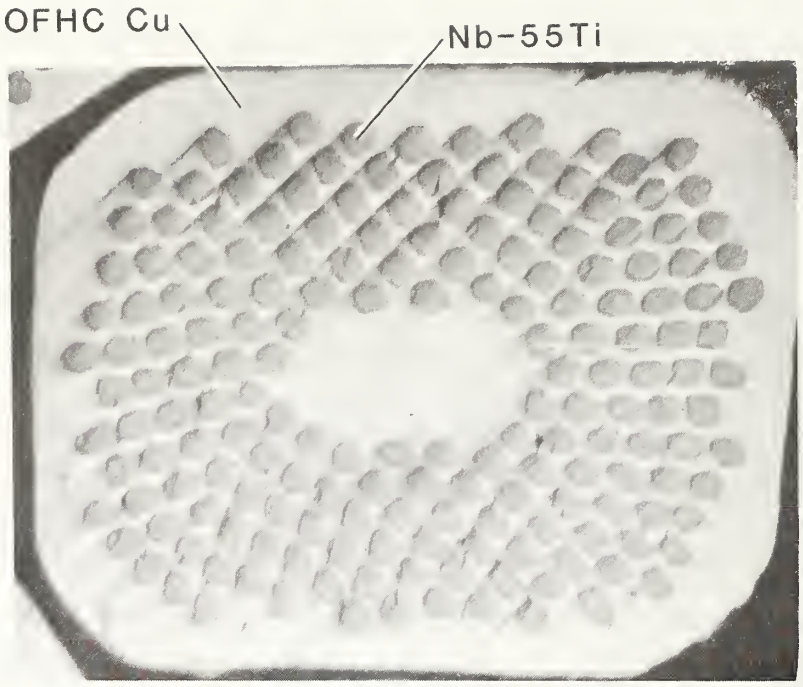

Fig. 4-2-3a Crossectional view of sample 1 (NSRDC 4-2, NbTi:Cu = 1:1.8).

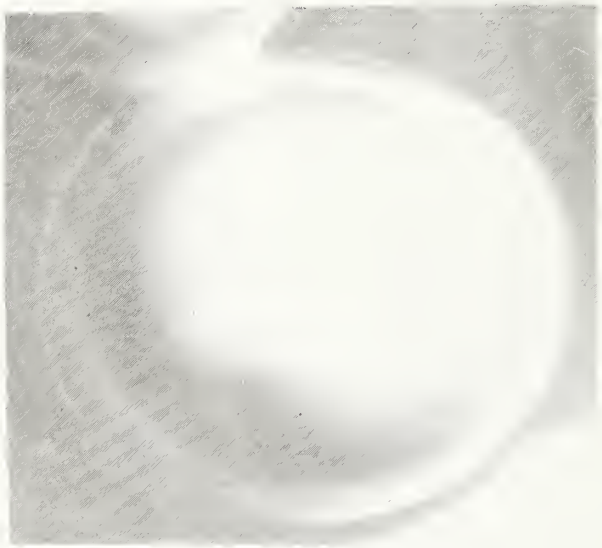

Fig. 4-2-3b Crossectional view of sample 3.

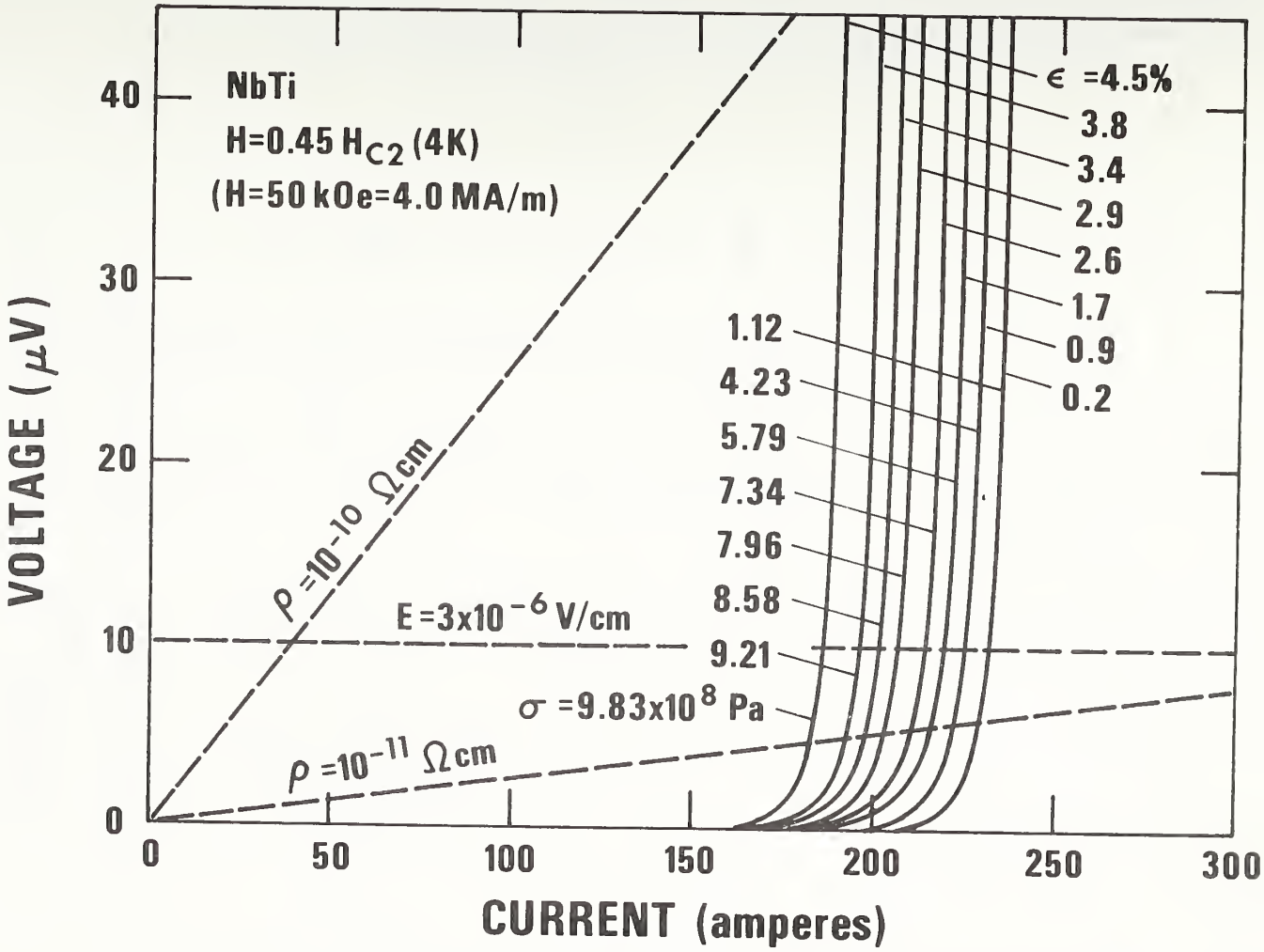

Fig. 4-2-4 Voltage-current characteristics for NbTi multifilamentary wire (sample 1) as a function of stress and strain. Also shown are 3 dashed lines corresponding to several critical-current criteria: an electric field along the wire of 3 μV/cm, and resistivities of 10^{-10} and 10^{-11} Ωcm, normalized to the cross sectional area of NbTi in the conductor.

lines corresponding to several critical current criteria: an electric field along the wire of 2×10^{-6} V/cm, and two resistivity levels of 10^{-10} Ωcm and 10^{-11} Ωcm (normalized to the cross-sectional area of NbTi in the composite wire). For consistency, the electric-field criterion has been used throughout the following discussion.

From Fig. 4-2-4, it can be seen that the critical current for this particular NbTi wire was found to be about 230 A at low stress. However as stress on the wire was increased, the critical current systematically degraded until eventually a critical current of less than 190 A was reached just prior to fracture.

In Fig. 4-2-5, I_c has been plotted as a function of stress. Here the open circles correspond to the critical current measured while the wire is under load and crosses represent the critical current measured after the load is applied and reduced to the prestress value. (The dotted line is included as a reference indicating the initial critical-current value measured at the preload level; the large X represents the point of fracture.)

Also tested were two other NbTi wires: the first was similar to the one described above, except larger in size (0.63 x 0.80 mm); the second was a monofilamentary wire shown in the bottom half of Fig. 4-2-3. Specifications for both are tabulated in Table 4-2-1. Critical-current results for each wire are shown in Figs. 4-2-6 and 4-2-7. Note that the qualitative form of the dependence of critical current on stress was the same in each case, i.e., the geometry of the wire did not significantly affect the results. Furthermore, when the results are normalized by the zero-strain value of the critical current, I_{co}, and plotted as a function

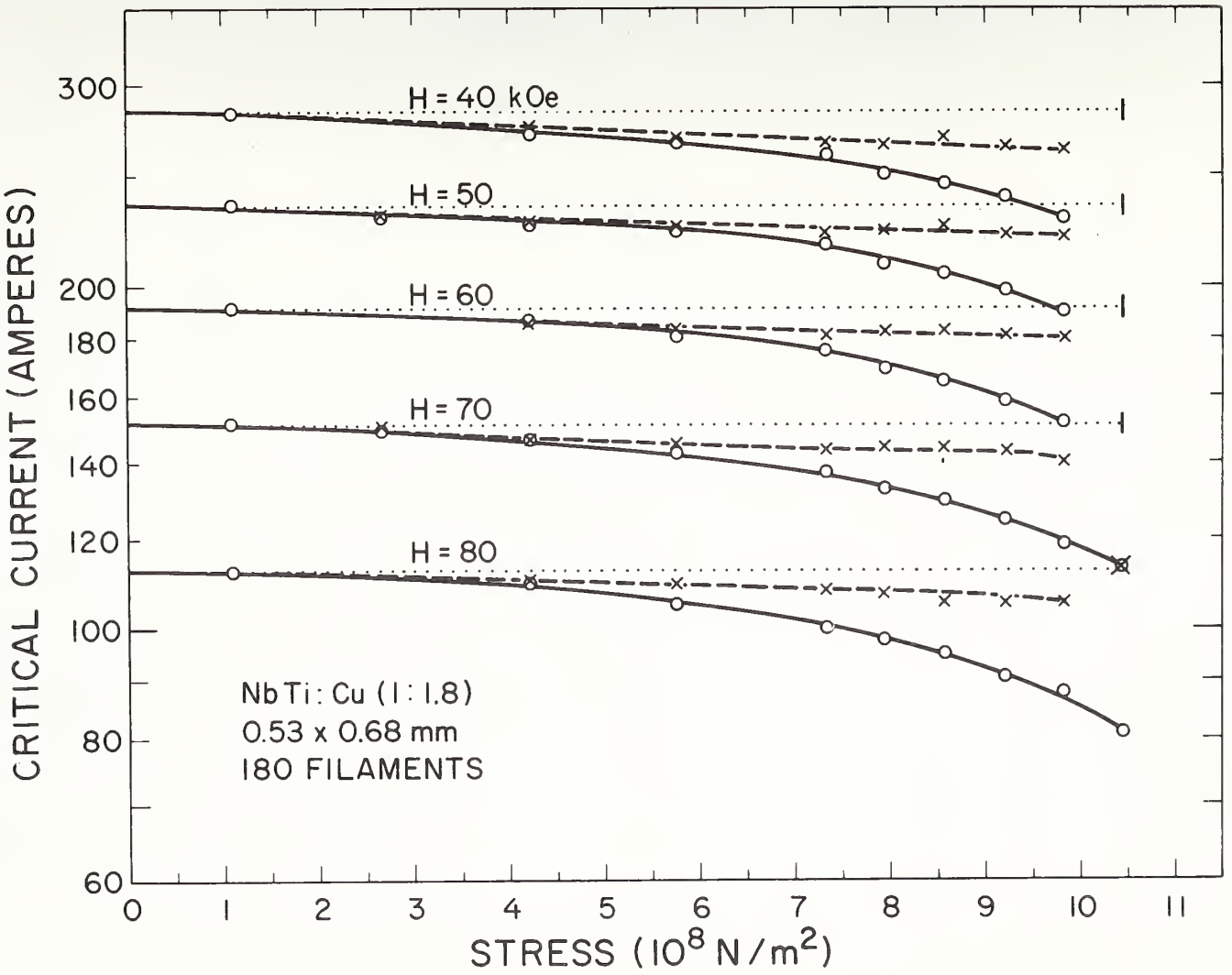

Fig. 4-2-5 Critical current as a function of stress at various applied magnetic fields. Solid curves correspond to the critical current measured while the wire is under stress; dashed curves represent the critical current measured after load is applied and reduced to the prestress value. (Sample 1).

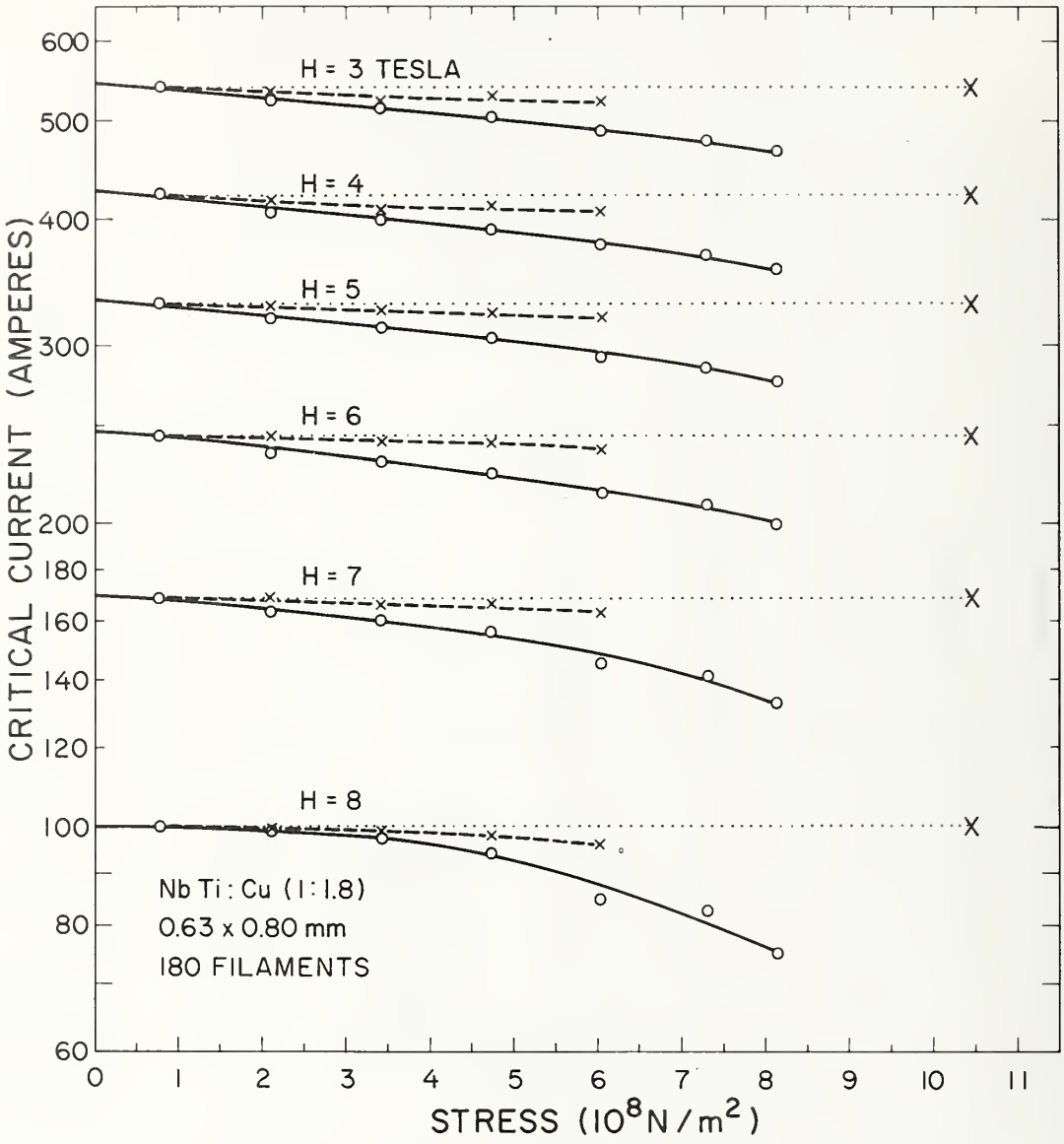

Fig. 4-2-6 Critical current as a function of stress at various applied magnetic fields. Solid curves correspond to the critical current measured while the wire is under stress; dashed curves represent the critical current measured after load is applied and reduced to the prestress value. (Sample 2).

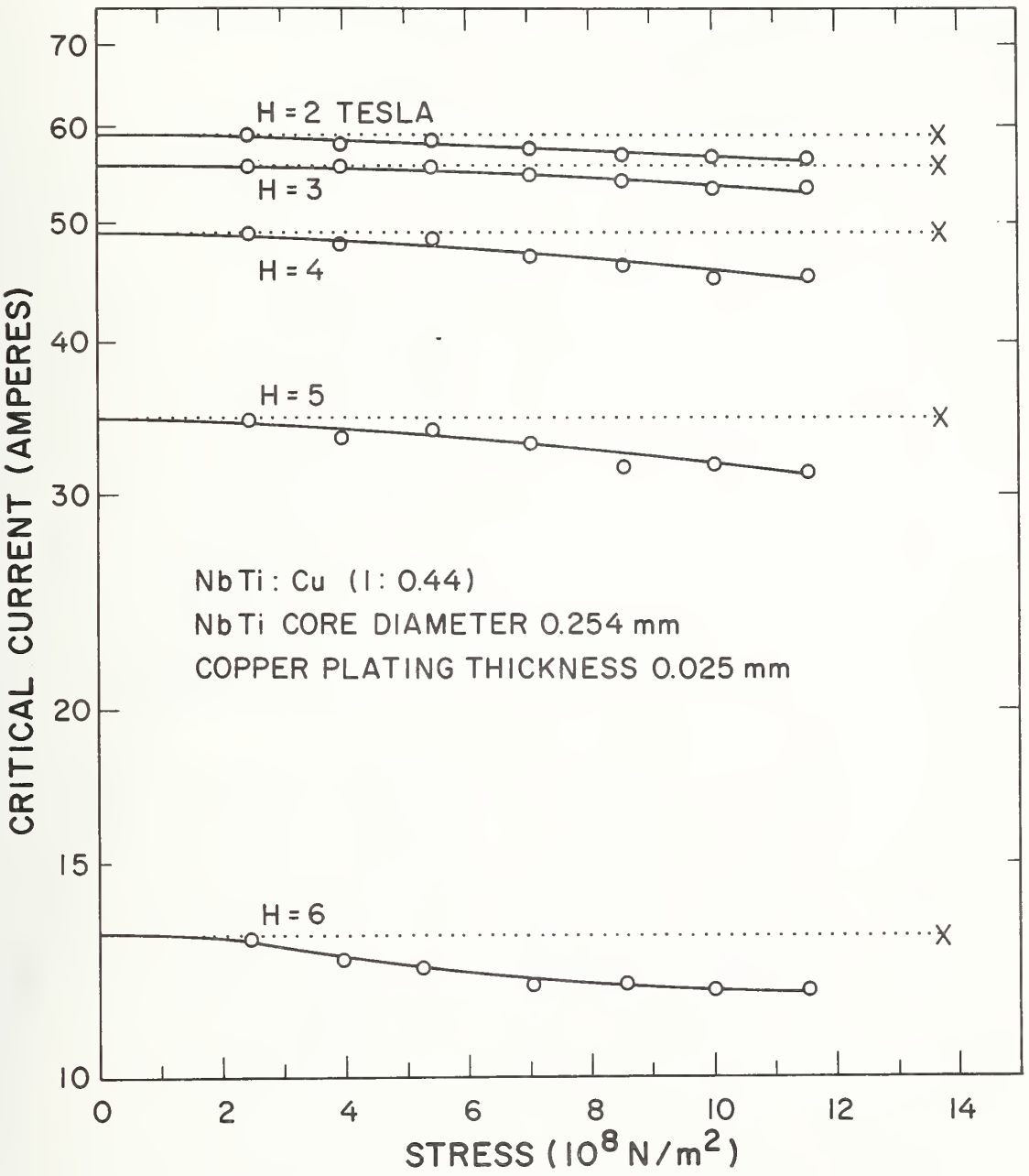

Fig. 4-2-7 Critical current as a function of stress at various applied magnetic fields. Solid curves correspond to the critical current measured while the wire is under stress; dashed curves represent the critical current measured after load is applied and reduced to the prestress value. (Sample 3).

of strain, there were quantitatively the same to within 5 to 10%. Such a universal strain plot is shown in Fig. 4-2-8 where the normalized results of sample 1 are compared with two other NbTi samples (4 and 5) having different amounts of copper and different filament sizes.

Three features of these data are emphasized.

1) The decrease in I_c commences at about 0.5% strain but does not become appreciable (i.e., greater than 5%) until strains exceeded about 1%.

2) A surprisingly large part of the degradation is recoverable. This can be seen most easily by comparing the two sets of data (circles and crosses) at the higher stress levels in Fig. 4-2-5. The residual critical-current degradation upon load removal was directly proportional to the residual strain remaining in the wire. [In fact a plot of I_c/I_{co} vs. residual strain upon load removal would fall right on top of the curves shown in Fig. 4-2-8.]

3) The magnetic field dependence in the 3 T to 7 T range was relatively small and is shown for sample 1 in Fig. 4-2-9. Based on all results to date, Fig. 4-2-9 is nearly universal and may be used for design purposes in most NbTi magnet systems.

From an engineering viewpoint, this stress degradation can be of importance in setting operating-current levels with adequate safety margins. As seen in Fig. 4-2-10, the usual I_c vs. H characteristic becomes a family of curves, each corresponding to a different stress level. At a low stress level of $1.12 \times 10^8 N/m^2$ (16 ksi) these data agree within 1% with independent data[2] obtained on the same wire using a standard zero-stress technique. However, as can be seen in Fig. 4-2-10, at higher

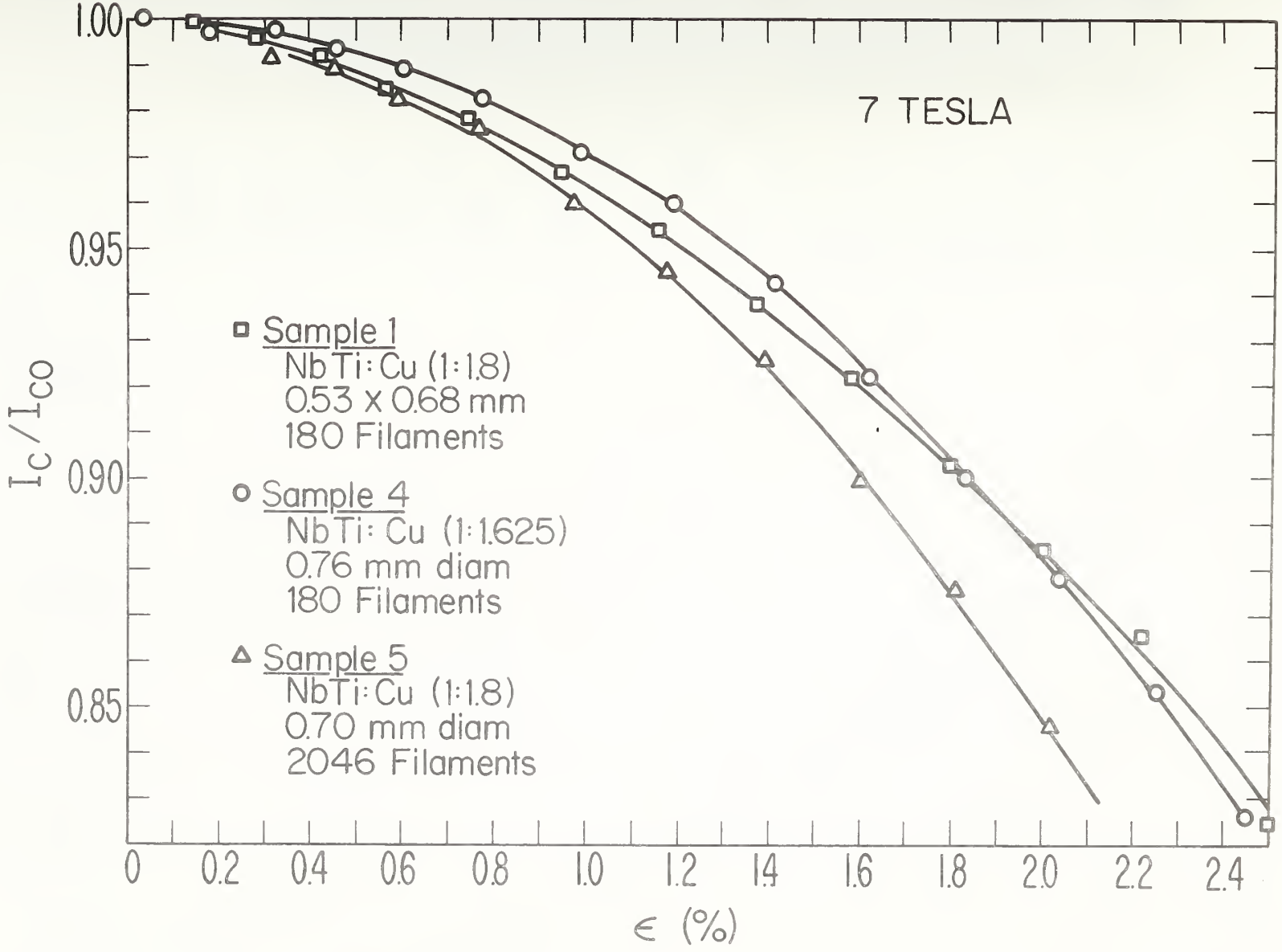

Fig. 4-2-8 Critical-current degradation in several multifilamentary NbTi:Cu composites (samples 1, 4, and 5) as a function of strain. Critical current, I_c, is expressed as a fraction of the initial unstrained critical current, I_{co}.

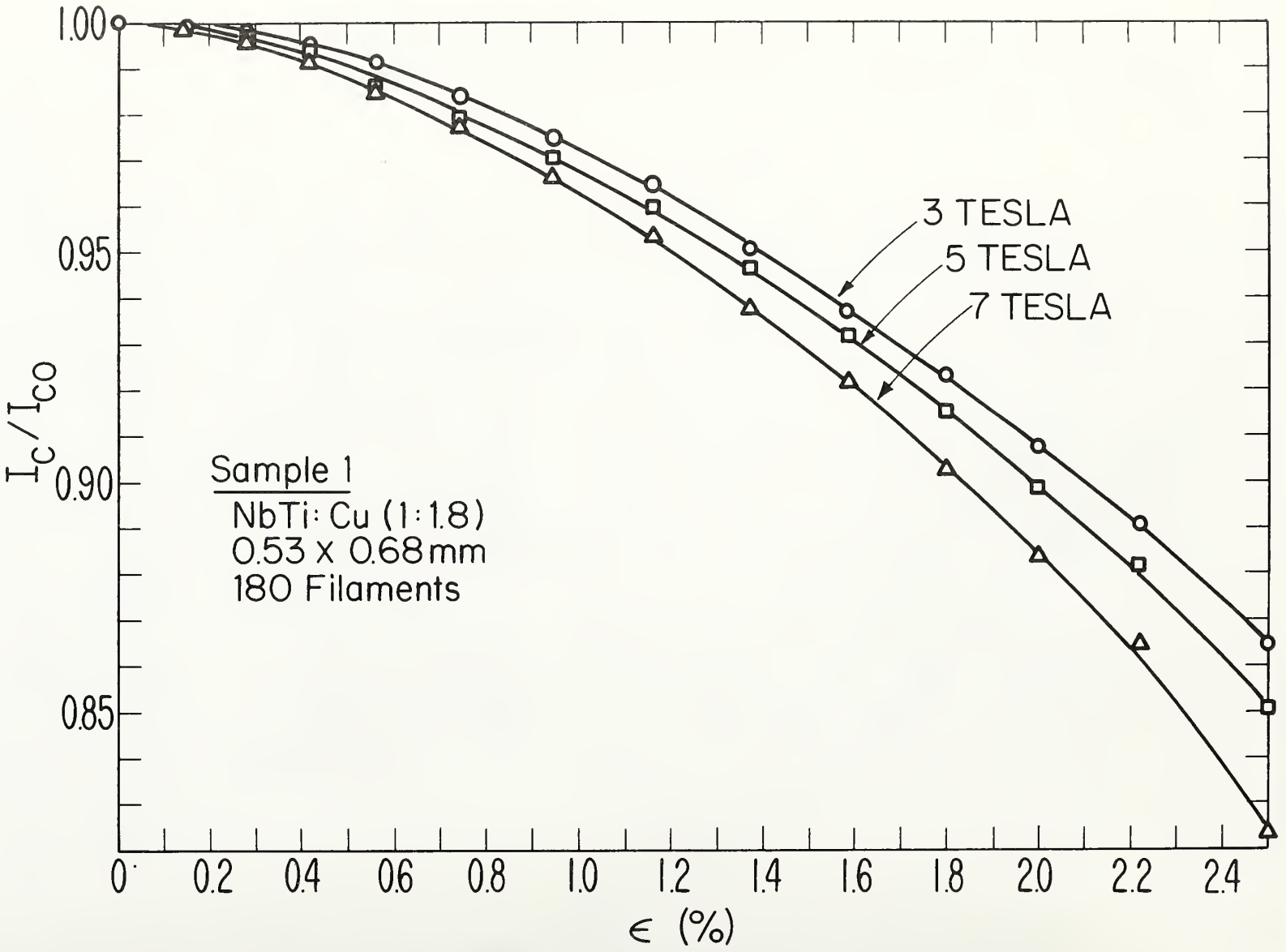

Fig. 4-2-9 Critical-current degradation in a multifilamentary NbTi:Cu composite (sample 1) as a function of strain at three applied magnetic fields. Critical current, I_C, is expressed as a function of the initial unstrained critical current, I_{CO}.

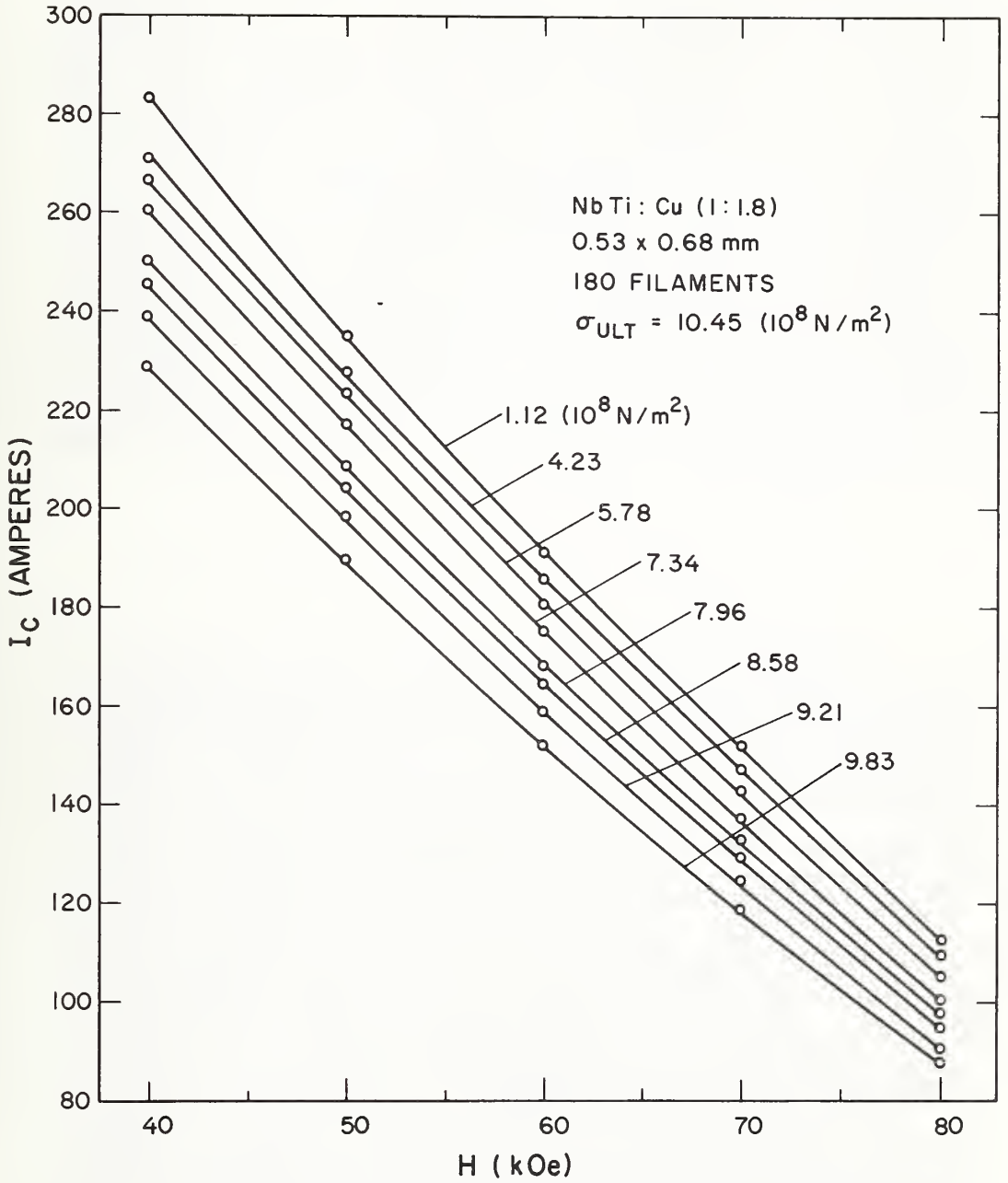

Fig. 4-2-10 Critical current vs. magnetic field at various applied stress levels.

stress levels (but still considerably below the ultimate) the characteristic is significantly depressed. As a percentage of the total critical current, the change for this particular sample varies from about 7% at half the ultimate strength ($5 \times 10^8 N/m^2$) to about 25% near the ulimate ($10 \times 10^8 N/m^2$). The percentage change in operating safety margins can be correspondingly greater, especially in large-scale applications involving high magnetomechanical stress levels.

4.2.5 Results: NbTi-Aluminum

Because aluminum costs less than copper, has a smaller magnetoresistance than copper, and weighs less than copper, it would be advantageous to use aluminum rather than copper to stabilize superconducting composites. Strain-effect data are reported here on the first attempts at fabricating aluminum-stabilized multifilamentary conductors.

Three types of aluminum-stabilized conductors were studied, the first type (tubular geometry) consisted of NbTi tubes filled with a high-purity aluminum stabilizer and embedded in a low conductivity 5056 aluminum-alloy matrix (shown in Fig. 4-2-11a); the second type (cable geometry) consisted of filaments of NbTi embedded in a 5056 aluminum-alloy matrix cabled with high-purity aluminum (shown in Fig. 4-2-12); and the third type (high-conductivity alloy) consisted of filaments of NbTi embedded in a higher conductivity 1100 aluminum-alloy matrix which was surrounded by high-purity aluminum (shown in Fig. 4-2-13). Results for each of these will be discussed in turn:

Tubular Geometry. Because pure aluminum is so much softer than pure copper, it is metallurgically very difficult to fabricate a conductor similar to that shown in Fig. 4-2-3 by simply replacing the

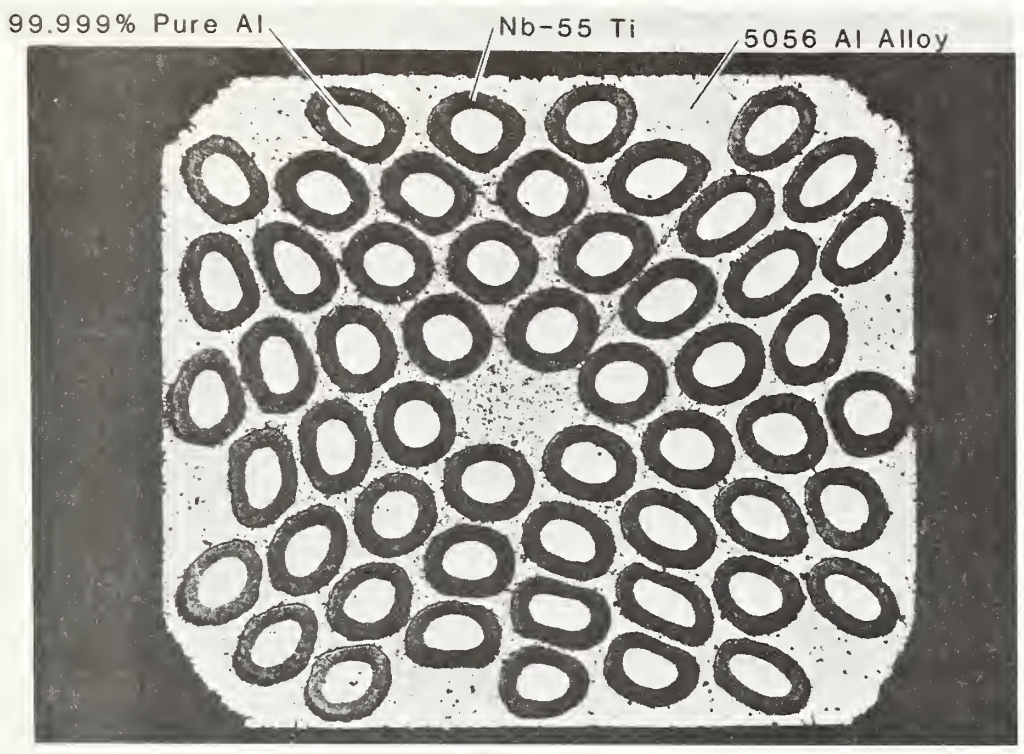

Fig. 4-2-11a Crossectional view of sample 4.

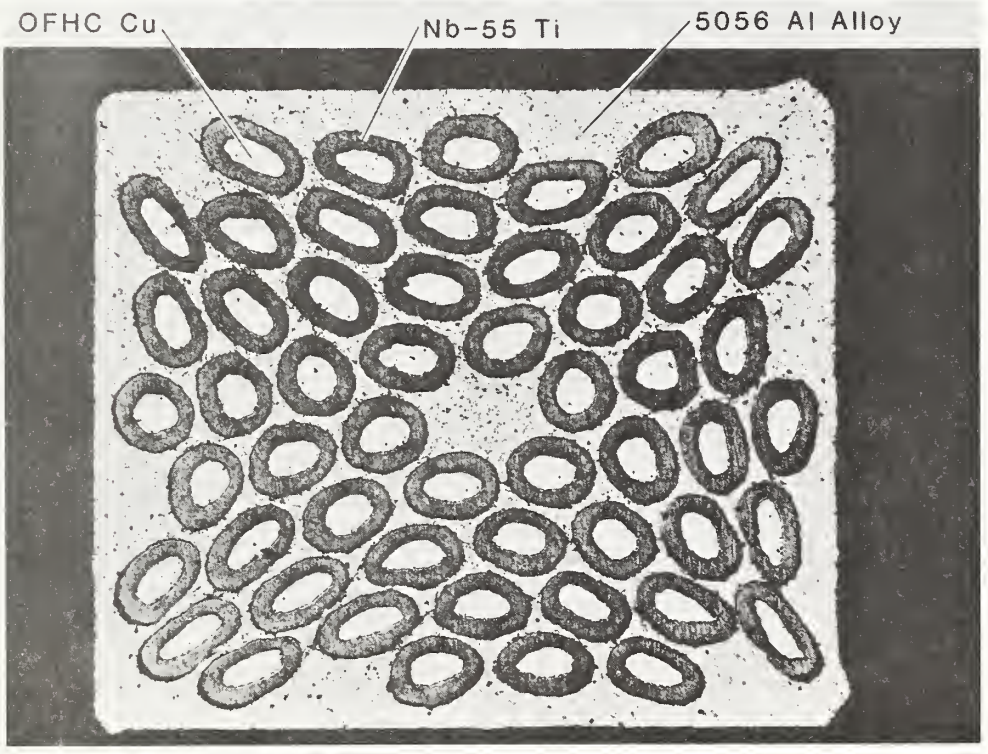

Fig. 4-2-11b Crossectional view of sample 5.

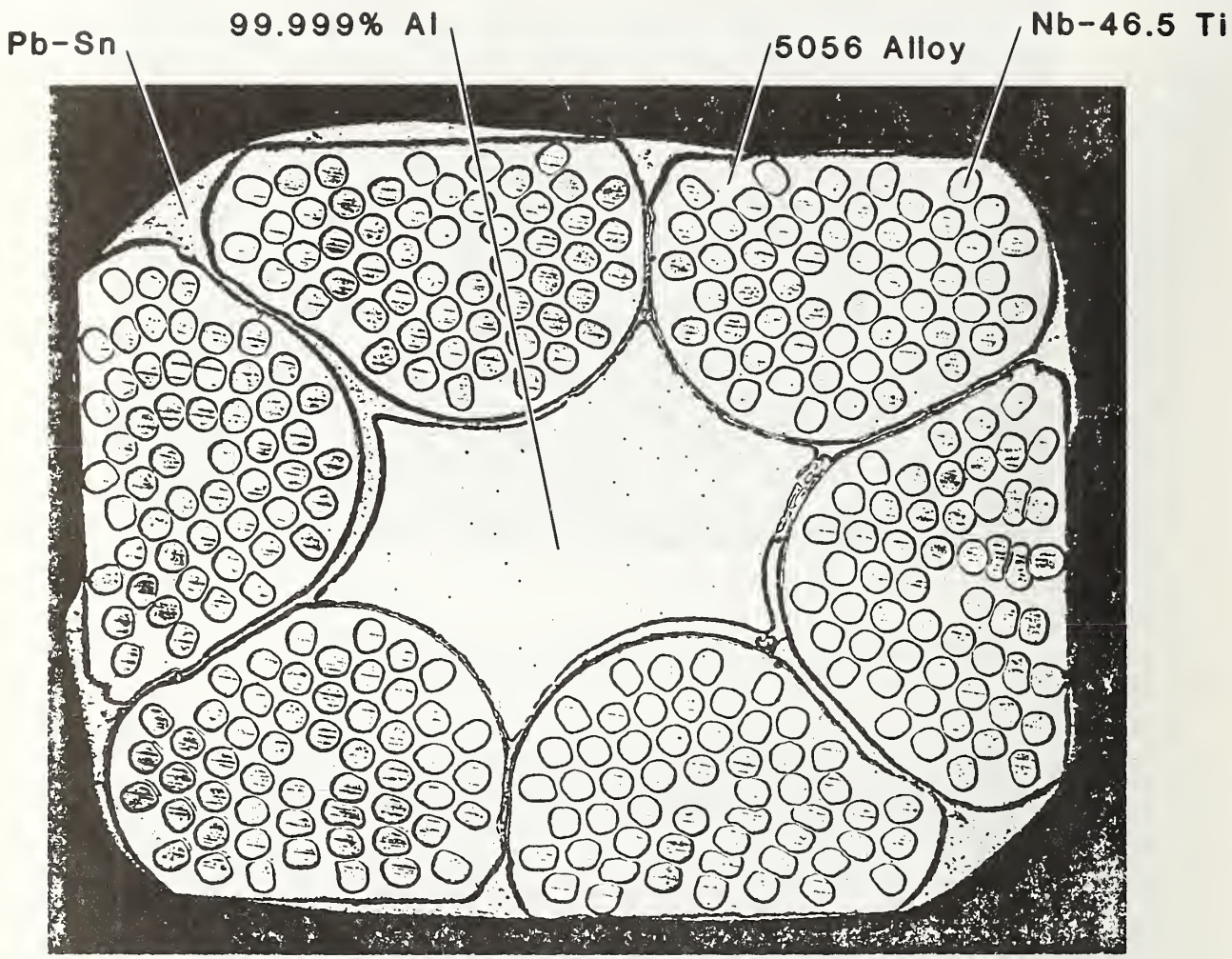

Fig. 4-2-12 Crossectional view of sample 6.

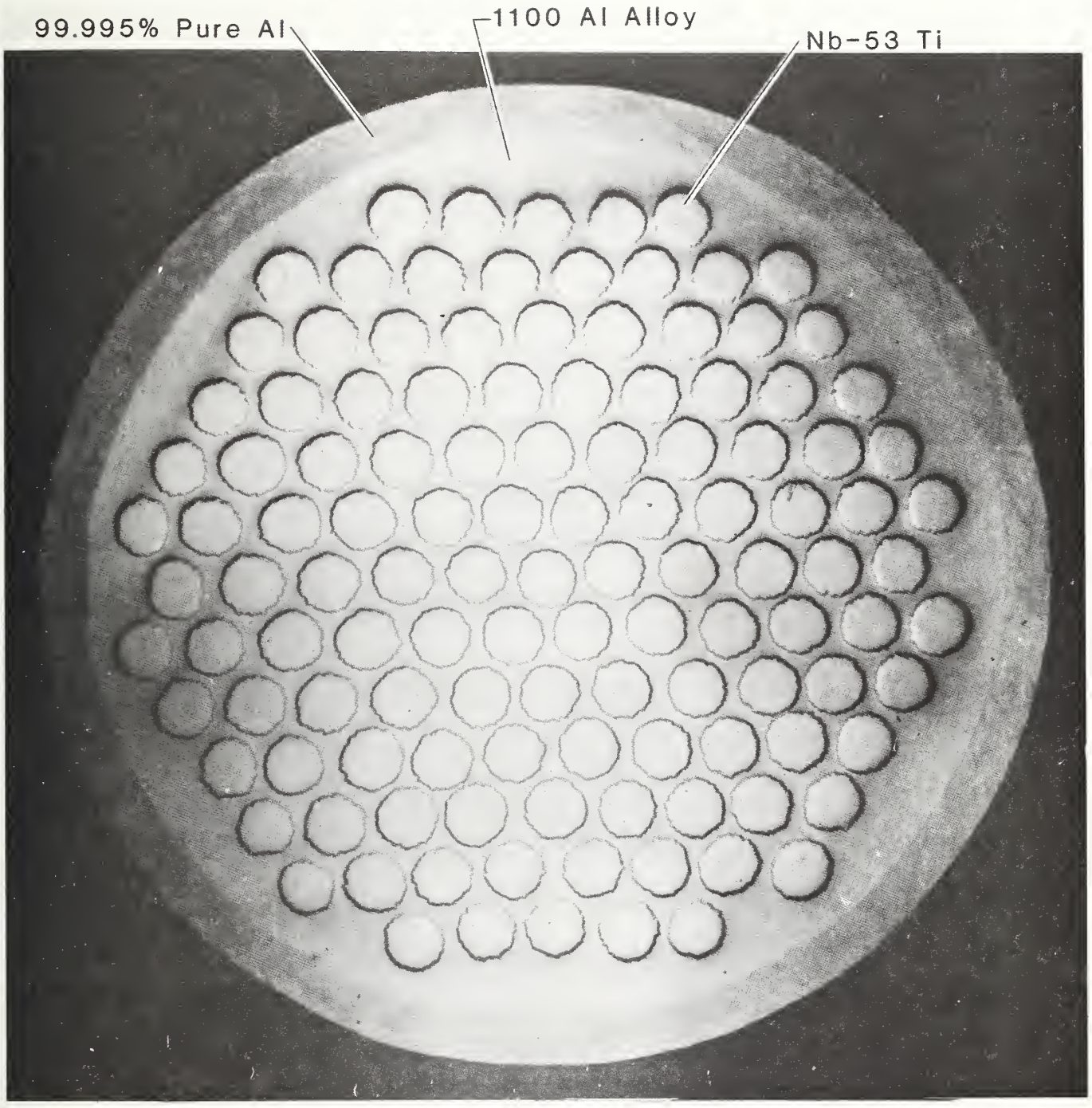

Fig. 4-2-13 Crossectional view of sample 7.

matrix by a pure aluminum matrix. The aluminum is too soft to uniformly reduce the NbTi filaments when the composite is drawn into wire (D. Koop, private communication). Consequently the first geometry studied consisted of NbTi tubes embedded in a relatively tough 5056 aluminum alloy matrix with the soft, pure aluminum stabilization material on the inside of each NbTi tube, as shown in Fig. 4-2-11a. (Further details are given in Table 4-2-1.)

Figure 4-2-14 shows a typical set of voltage-current characteristics for this specimen. The conductor was stable, but as seen in Fig. 4-2-14, it exhibited a hysteresis in its critical current characteristics depending on whether the magnetic field was being increased or decreased. This resulted from magnetic flux trapped in the tubes and indicated that self-field ac losses would be large for this tubular geometry. All subsequent data reported here were obtained with field increasing to the indicated value.

In an effort to compare the strain effects of aluminum stabilization vs. copper stabilization directly, two wires were tested under tension which were alike in every way, except one (Fig. 4-2-11a) was stabilized by high purity aluminum (RRR$\tilde{=}$5000), the other (Fig. 4-2-11b) by OFHC copper (RRR$\tilde{=}$70). Both consisted of NbTi tubes embedded in a 5056 aluminum alloy matrix with the stabilization material on the inside of the tubes. (Further details are given in Table 4-2-1.) Results for the two wires are shown in Fig. 4-2-15. As seen in Fig. 4-2-15, the strain degradation of the critical current for the two wires was identical to within 1%. The magnitude of the effect, however, was greater for this tubular geometry than for the strain effect in non-tubular NbTi copper conductors (shown in Fig. 4-2-3).

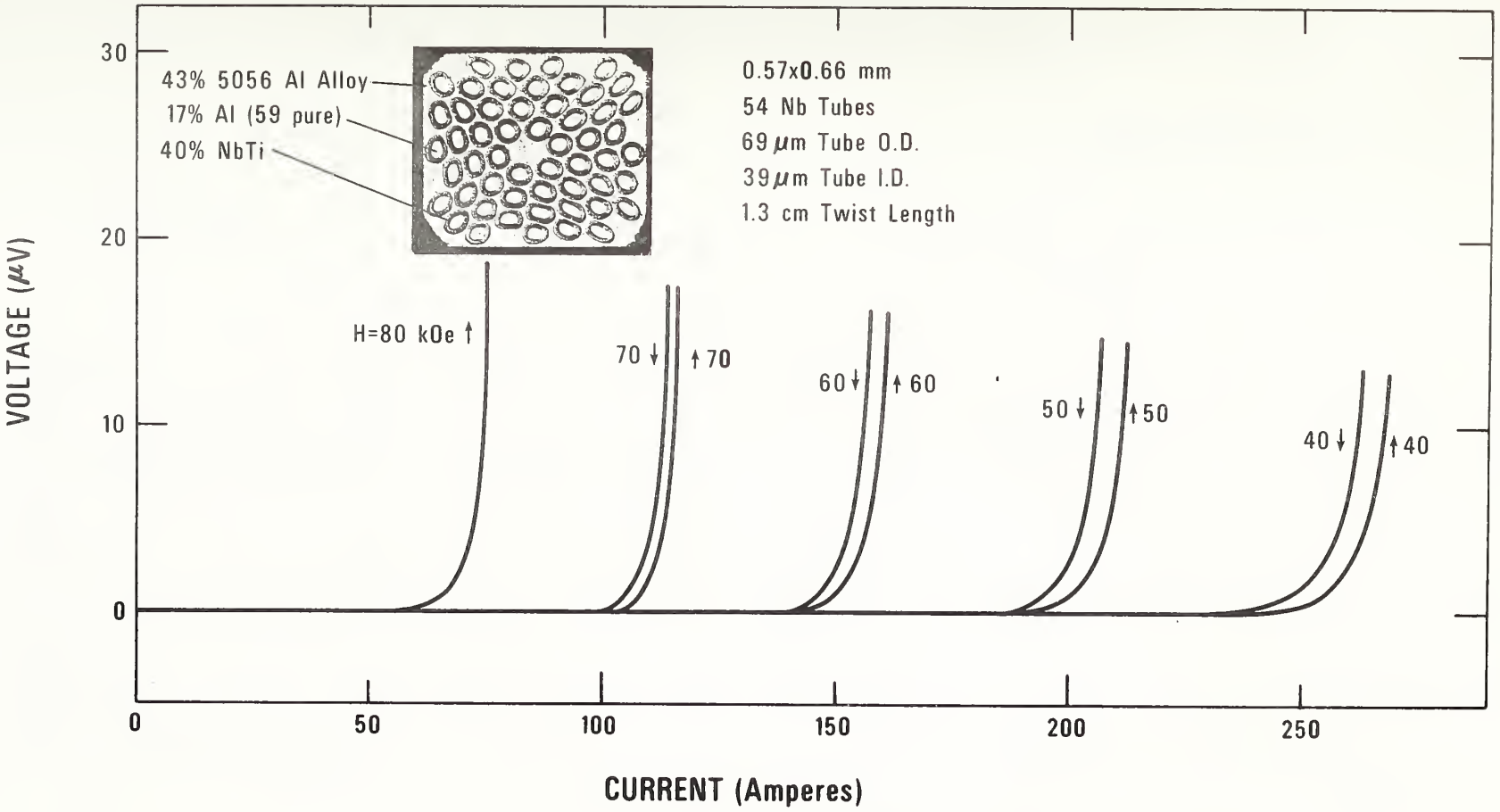

Fig. 4-2-14 Voltage-current characteristics for sample 4, at several values of magnetic field. Characteristics labeled by upward-pointing arrows indicate the field was increased to the value shown; downward-pointing arrows indicate the field was decreased to the value shown.

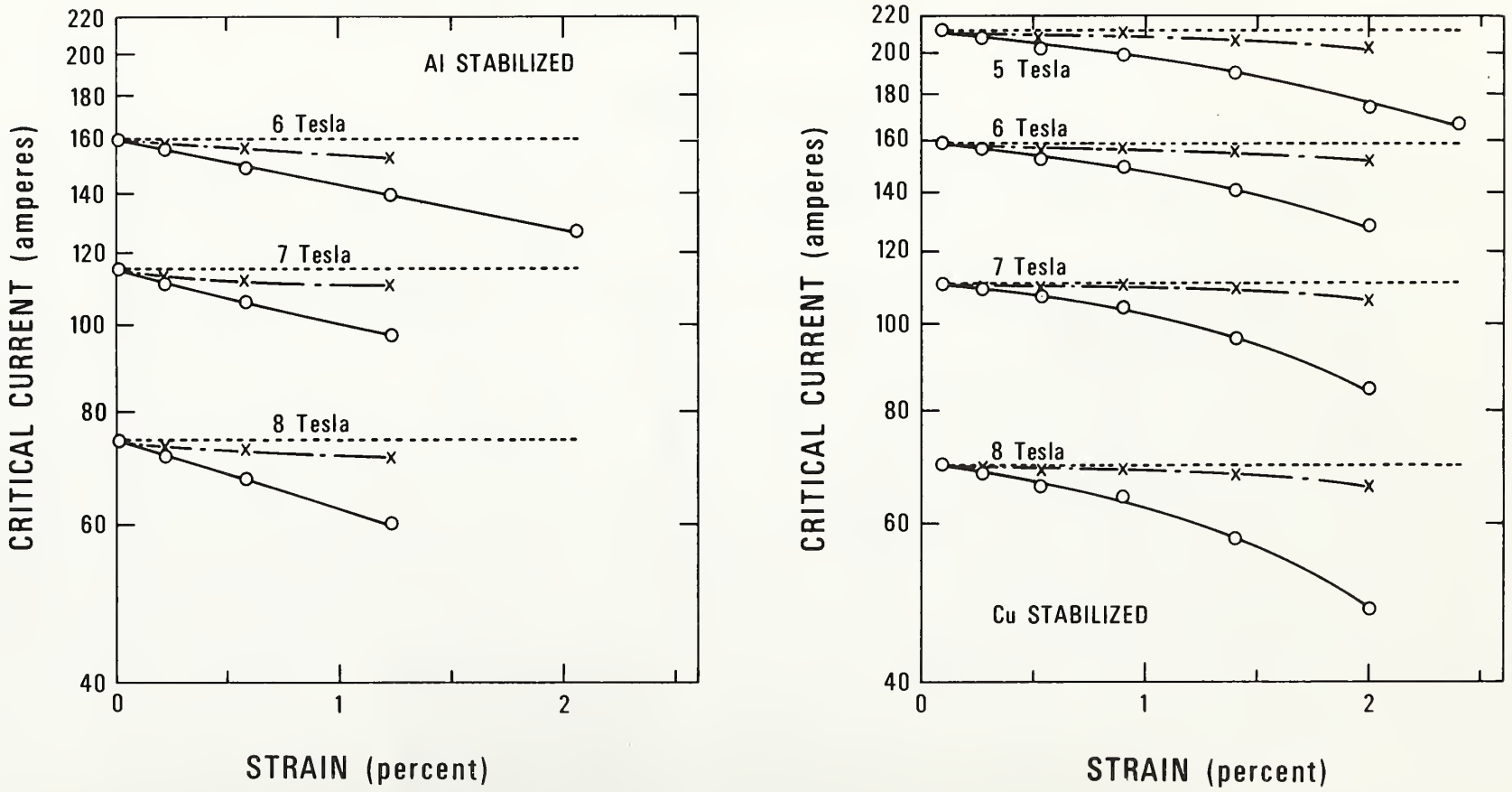

Fig. 4-2-15 Comparison of critical current vs. strain characteristics for aluminum- and copper-stabilized NbTi superconductors (samples 4 and 5).

Other problems with this geometry are:

1) the current transfer length (Appendix A.1) will be much longer than for typical NbTi copper conductors because the NbTi tubes are separated by a high-resistivity aluminum-alloy matrix.
2) The ratio of stabilizer-to-superconductor is limited to low values because only the NbTi tube cores are available for stabilization material.

Cable Geometry. To avoid the problems associated with tubes, the second geometry tested consisted of several strands of NbTi filaments in a 5056 aluminum alloy matrix. The strands were cabled with several additional strands of high-purity (5-9 grade) aluminum to provide stabil ization, see Fig. 4-2-12. The entire cable was soldered together by nickel plating the individual strands and soldering with 50/50 PbSn solder. (Sample details are given in Table 4-2-1.) Unfortunately, this cable geometry was found to be unstable, probably because of the high resistivity 5056 matrix surrounding the filaments. At 5T, only 68% of critical current could be achieved before thermal run away would occur. The full critical current could be achieved only in an isolated strand, surrounded completely with helium.

The 4K resistivity of the 5056 aluminum alloy matrix was about 1.4 $\mu\Omega$-cm, comparable to that of tin bronze used in the manufacture of multifilamentary Nb_3Sn conductor. But the filament size in this cable was about 7 times that in a typical multifilamentary Nb_3Sn wire. Thus, as far as the future direction of work is concerned, it is noted that choosing an aluminum alloy only slightly more conductive than 5056 and reducing the filament size to less than 10 microns should increase the

stability of the cable to a practical level (at least comparable to multifilamentary Nb_3Sn).

High-Conductivity Aluminum Alloy Conductor. The third type of conductor studied was fabricated much the same as commercial copper NbTi (Fig. 4 2-3a) but with the copper replaced by a higher-conductivity 1100 aluminum alloy surrounded by 4-9 purity aluminum, see Fig. 4-2-13. The 1100 alloy has a 4K resistivity considerably less than that of the 5056 alloy. The conductor was stable and had a critical current density typical of copper-stabilized NbTi. The only problem was fabrication. Only short lengths could be drawn because of breakage and necking in the NbTi filaments.

4.2.6 Aluminum Conductors: Conclusion

These data suggest that a workable method of fabricating an aluminum-stabilized conductor would be to use an aluminum-alloy matrix with a resistivity somewhat less than 5056 aluminum (e.g., 1 μΩ-cm or less) and reduce the NbTi filament diamters to the 10 μm range. Such a conductor would be both fabricable and stable (although not as stable as typical copper:NbTi multifilamentary conductors).

Perhaps the best method for utilizing the advantages of pure aluminum as a stabilizer without encountering the fabrication problems of such a soft metal is to bond the pure aluminum stabilizer to the NbTi after fabrication. With present joining technology, there is no reason why pure aluminum could not be bonded to a copper-fabricated multifilamentary NbTi core. This could be particularly advantageous in the production of cryostabilized conductors where the required amount of stabilization material is many times that actually needed to fabricate the NbTi filaments.

References

1) Superconducting Machines and Devices, Large Systems Applications (S. Foner and B. B. Schwartz, eds.), Plenum Press, New York (1974); H. Brechna, Superconducting Magnet Systems, Springer-Verlag, Munich (1973).

2) Magnetic Corporation of America and Westinghouse Electric Corporation, private communication.

4.3 MECHANISMS FOR CRITICAL-CURRENT DEGRADATION IN NbTi AND Nb_3Sn MULTIFILAMENTARY WIRES

by J. W. Ekin

Abstract

Critical currents of NbTi and Nb_3Sn multifilamentary wires have been studied in magnetic fields to 9 T as a function of mechanical load applied at 4 K. Degradation of the critical current in NbTi is limited to about 30% with the effect becoming large only at strains above ~1%. The change in critical current with strain is much larger in Nb_3Sn, commencing at strains of 0.1 to 0.3%. For both superconductors, the first 20 to 30% decrease in critical current is almost totally reversible. A number of possible explanations of the observed degradation are considered, including filament breakage, heat generation by mechanical creep, degradation of the stabilizing matrix, and defect formation in the superconductor itself. Results of experiments to test the source of degradation are reported. Evidence for microcrack damage in the Nb_3Sn reaction layer has been found and it is suggested that defect size variations on the order of a coherence length (~5 nm) can account for the reversibility of the degradation as well as low-strain enhancement effects.

4.3.1 Introduction

Recently it has been shown[1-4] that when NbTi or Nb_3Sn multifilamentary wires are uniaxially stressed at liquid helium temperatures, the critical current of these superconducting wires undergoes a nearly reversible degradation. In this paper we consider various possible sources of this degradation and report the results of several experiments to test these explanations.

A summarized comparison of the results given in Refs. 1 and 2 for NbTi and Nb_3Sn is shown in Fig. 4-3-1. As shown by the solid curve labeled NbTi, the effect in NbTi commences at about 0.5% strain and grows to about a 30% degradation as the ultimate strength of the wire is approached. The recovery curve for NbTi (dashed line in Fig. 4-3-1) shows that the critical current recovers to about 95% of its unstressed value upon load removal. That is, the effect is highly reversible; large degradation occurs only when the wire is actually under stress.

In Nb_3Sn, the degradation threshold occurs at lower strains and is dependent on reinforcement and cabling techniques used in the wires' construction. As shown by the curve labeled Nb_3Sn in Fig. 4-3-1, the effect typically starts at threshold strains in the range 0.1-0.3% depending on wire configuration and condition. The critical-current degradation is almost totally reversible up to strains about double the threshold strain. At higher strains, however, much of the damage is permanent, and recovery is only partial.

To summarize the observations on multifilamentary wires:

(1) The first 20 to 30% decrease in critical current, I_c, is almost totally reversible for both NbTi and Nb_3Sn.

(2) Total degradation before fracture is limited to about 30% in NbTi, with the effect becoming large only at strains above $\sim$1%.

(3) The change in I_c with strain is much larger in Nb_3Sn and commences at strains of 0.1-0.3% depending on wire configuration and condition.

A number of possible explanations have been suggested. Included among them are the following: simple filament breakage, reduction in

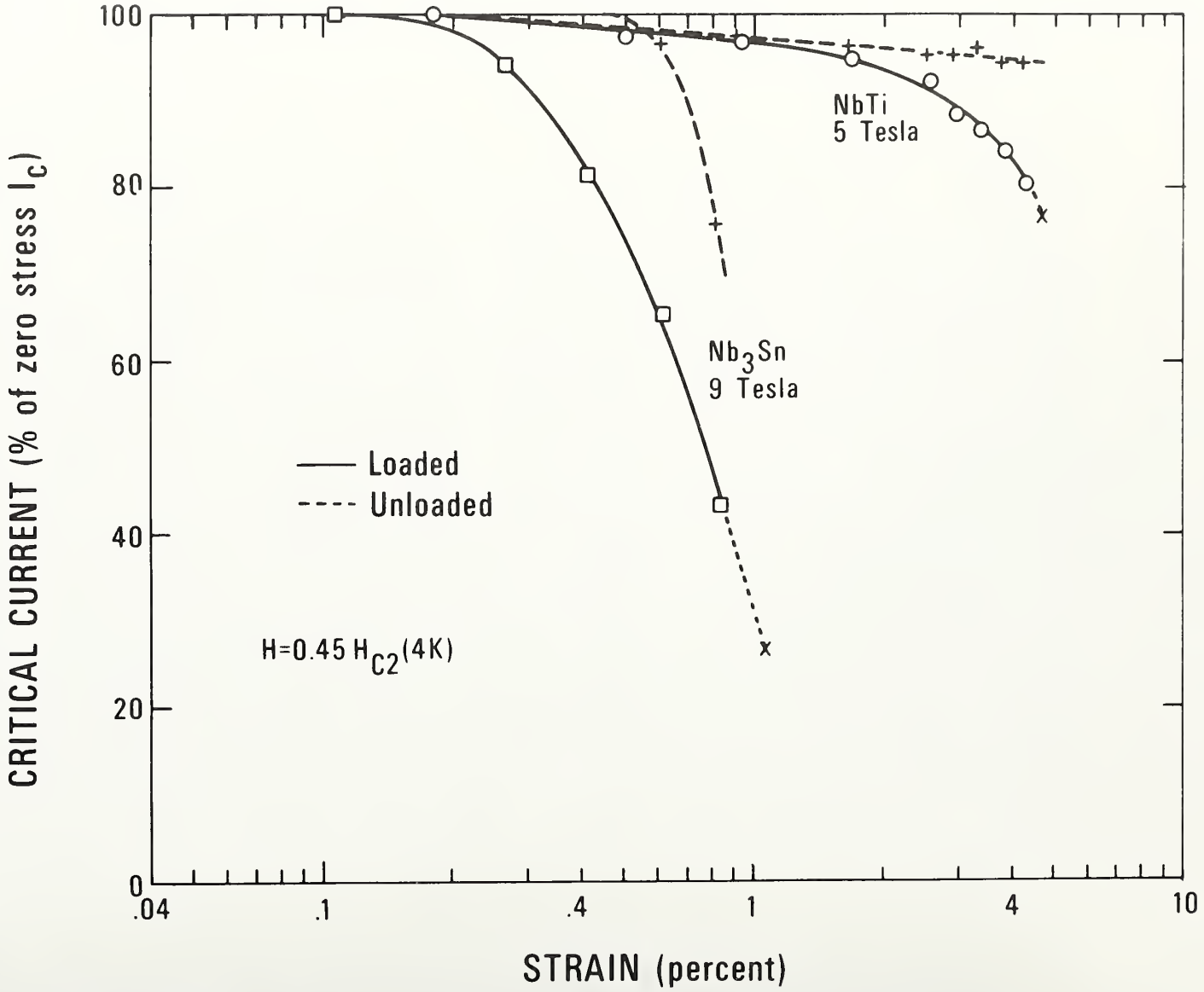

Fig. 4-3-1 Summary of critical current degradation in multifilamentary NbTi and Nb_3Sn wires. Results were obtained at comparable magnetic fields (0.45 H_{c2}) for the two materials. Dashed lines for each case indicate the critical-current recovery value after unloading.

cross-sectional area of the wire, heat generation by steady-state creep, degradation of the stabilizing matrix conductivity, stress-induced martensite formation, and microcrack formation in the superconductor. Results of experiments to test several of these explanations are presented below.

4.3.2 Mechanisms

Filament Breakage. As noted above, the first 20 to 30% decrease in I_c is almost totally reversible for both NbTi and Nb_3Sn. Significant filament breakage would not produce a reversible effect. Furthermore, SEM examination of stressed wires used in obtaining the experimental data in Fig. 4-3-1 showed the filaments to be intact after testing. However, in the irreversible, high-strain region for Nb_3Sn, cracking of the Nb_3Sn reaction layer was observed. This will be discussed in more detail in Section 3.

Area Reduction. An elastic reduction in cross-section area of the superconductor would produce a proportional increase in current density and a reversible decrease in I_c. However, the average cross-sectional area reduction for the samples shown in Fig. 4-3-1 was on the order of 1-2%, too small to account for the 30%+ effects observed.

Creep. Low temperature creep in metals is small and usually characterized by a time-varying logarithmic dependence.[5] If heat generation by slow plastic deformation of the superconductor were responsible for the decrease in I_c, then the degradation under static loading would be expected to vary with time. The I_c degradation would be largest when the load is first applied, but decreasing with time as the creep rate and rate of heat generation decrease.

To test for this, a constant bias current of 208 A was passed through a NbTi wire as shown in Fig. 4-3-2. At his current, the flux-flow voltage along a 3 cm-length of wire was less than 0.5 μV. However, upon stressing the wire to 8 x 10^8 Pa (∿80% of the ultimate stress), the critical current decreased to the point where there was a large increase in flux flow voltage to 15 μV. As shown in the insert in Fig. 4-3-2, the voltage along the wire remained constant at 15 μV over the entire test period of 2 hours. Upon unloading the wire, the voltage dropped immediately to 0.05 μV. No time-dependent changes in the critical-current degradation were observed during the two hour period.

The analysis can be carried slightly further to establish an upper limit on the temperature change in the wire. dI_c/dT for the wire was measured to be 62A/K at 4 K. This would mean the wire would have to rise 400 mK in temperature to account for the I_c degradation shown in Fig. 4-3-2. The change in voltage during the two hour test was less than 0.5 μV, which, combined with the V-I slope of 0.28 A/μV, results in the temperature change of the wire being less than 2 mK during the test. The magnitude and time invariance of the effect would thus suggest that the observed I_c degradation is not associated with a stress-induced heating effect.

Matrix Degradation. I_c degradation curves were obtained on two NbTi wires, one stabilized by high-purity aluminum. Both wires were essentially identical in every respect except for the stabilization material. The OFHC copper stabilizer had a residual resistivity ratio (RRR) of 23; the aluminum stabilizer had a RRR of 580. The stabilization material is contained inside the superconducting filaments and has an average cross section diameter of 39 μm.

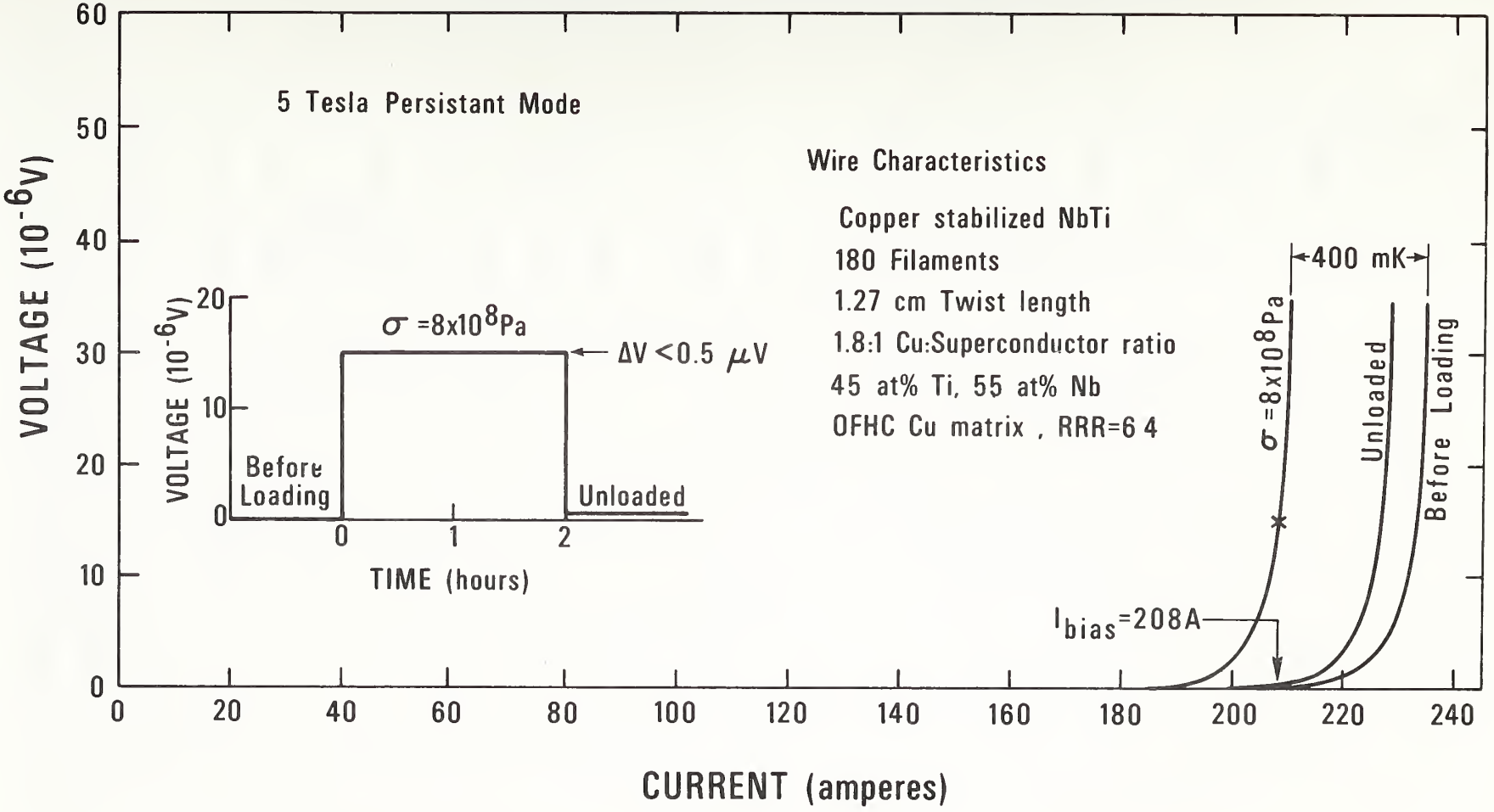

Fig. 4-3-2 Time invariance of the critical-current degradation. Voltage-current plot shows the extent of degradation in a NbTi wire at a stress of 8×10^8 Pa. Voltage-time insert indicates the constancy of the flux-flow voltage during the 2 hour test when the wire was biased at a current of 208 A.

Results for these two wires are shown in Fig. 4-3-3. A close comparison of the two sets of data shows the degradation in both wire types to be essentially identical, even though the starting RRR's for the two stabilizing materials differed by more than an order of magnitude. Moreover, a measurement of the change in RRR ($R_{293K} \div R_{T_c}$) for both wires after stressing (but kept at 77 K) showed that the RRR of the high-purity Al had decreased to less than half its initial value (RRR = 191). By contrast, stress affected the relatively impure copper much less, decreasing its already low RRR from 23 to 19. So not only was the starting RRR of each material different, but the stress-induced change in RRR during testing was very dissimilar. Yet, in spite of these differences in matrix conductivity, the I_c degradation of the two wires was essentially the same. These data suggest that the matrix is not playing major role in degradation of the critical current. (Of course, if the matrix degradation becomes too great, eventually the thermal vs. magnetic diffusivity balance is upset and the wire becomes unstable.)

It is also interesting to note the effects of stress on the superconductor cooling current, that is, the current at which a wire sample returns to the superconducting state after being driven normal (dashed lines in Fig. 4-3-4). It varied very little with stress, even under loads which degraded the critical current by more than 90%. Since this current is mainly a functin of I^2R heating in the matrix, this, too, would focus attention on the superconductor, rather than the matrix, as the source of degradation.

Magnetic-Field Dependence. The degradation effect was found to be strongly dependent on magnetic field intensity. For example, one Nb_3Sn

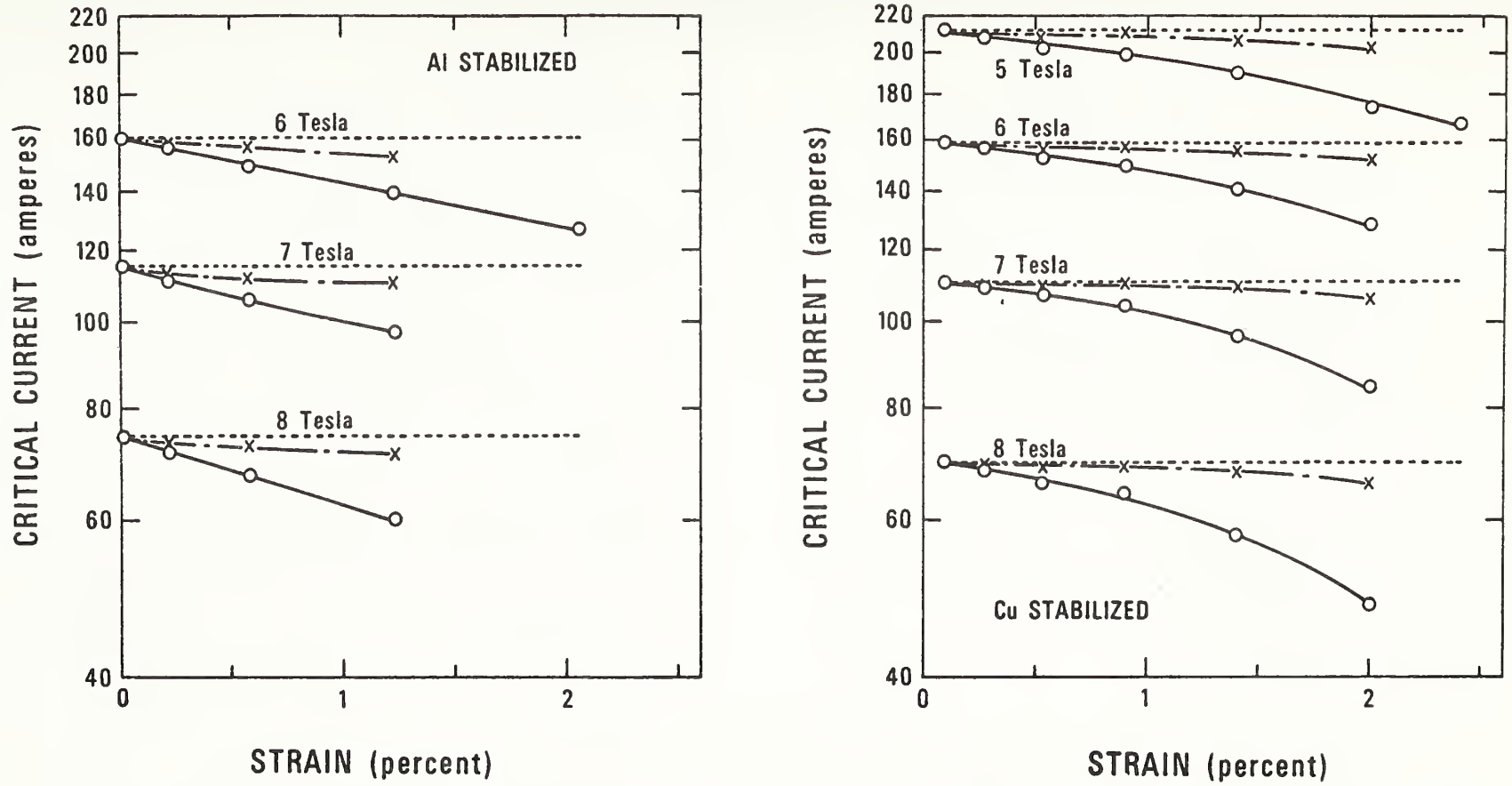

Fig. 4-3-3 Invariance of the critical-current degradation with residual resistivity ratio (RRR) of the matrix. Under stress, the RRR for the Cu-stabilizer decreased to 19, while RRR for the Al-stabilizer decreased to 191. The stabilization material for each conductor was contained within NbTi tubes (69 μm O.D., 39 μm I.D.) embedded in a 5056 aluminum alloy matrix.

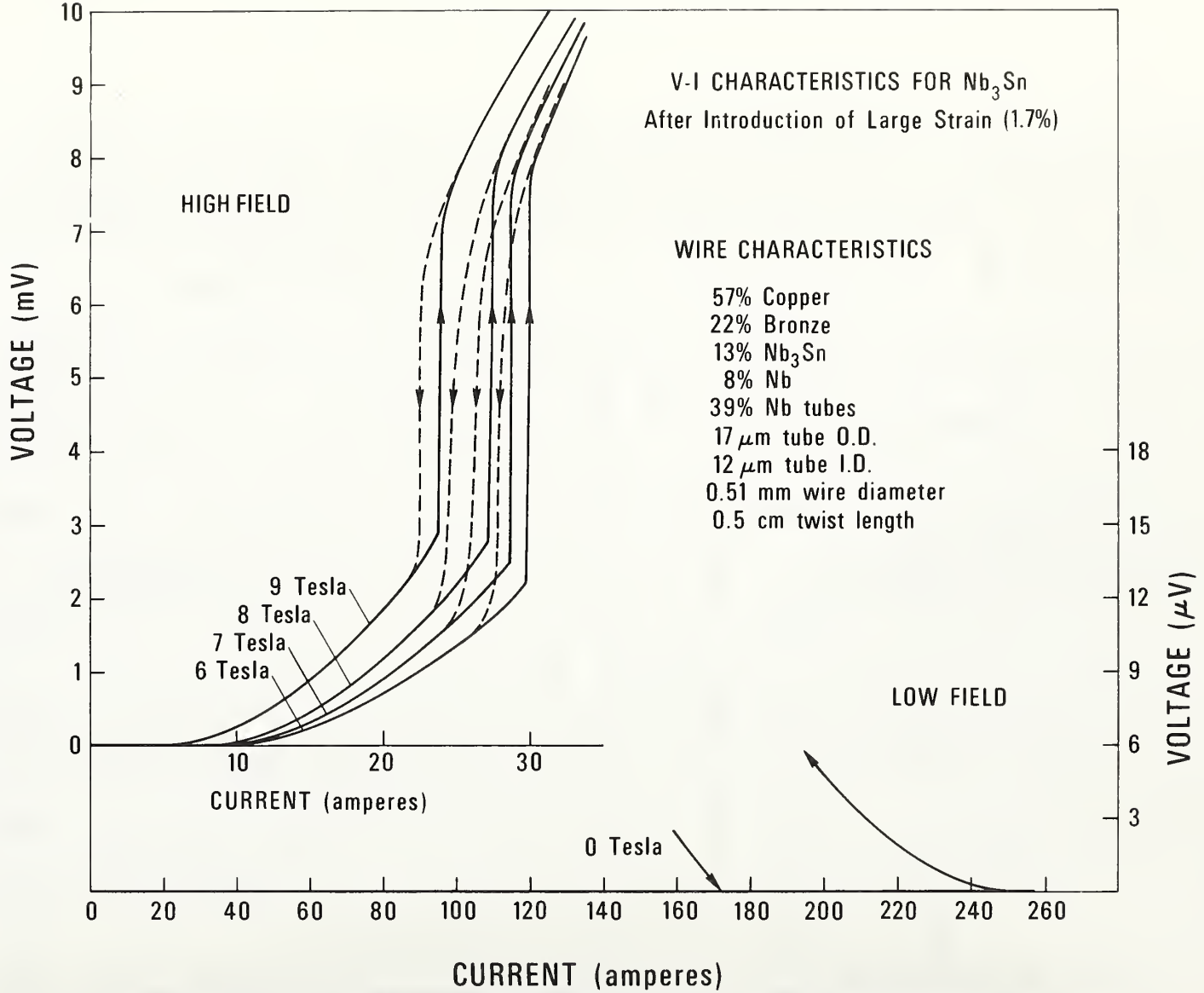

Fig. 4-3-4 Magnetic-field dependence of the critical-current degradation. Voltage-current insert shows the large resistivity (10^{-7} Ω cm) of a highly strained superconductor at high magnetic fields, compared with the very low resistivity (<10^{-13} Ω·cm) of the same wire at zero applied field. Dashed lines show the retrace curves as the wire returned to the superconducting state after being driven normal.

wire was strained to such an extent that a resistivity of more than 10^{-7} Ω cm was measured at a current of 10A in a field of 9 T; see Fig. 4-3-4. However, when the same damaged wire was tested at zero applied field, its resistivity was less than 10^{-13} Ω cm at currents up to 257 A (at which point flux instabilities drove it normal). The stress-induced resistivity is thus observed to be strongly field dependent, suggesting the effect has its origin in vortex movement within the superconductor.

4.3.3 Superconductor Degradation -- Discussion

Briefly summarizing the results thus far, I_c degradation in NbTi and Nb_3Sn does not appear to be caused by any of a number of peripheral effects associated with degradation of the stabilizing matrix, heating of the wire caused by plastic deformation of the composite conductor, elastic reduction of the crossectional area, etc. Rather, it appears to be due to stress-induced changes in the superconductor itself.

For the case of high strains in Nb_3Sn, the irreversible degradation can well be accounted for by the relatively wide ($\gtrsim$100nm) transverse cracks we have observed in highly stressed samples using SEM techniques. Enhanced current density in the regions near the crack sites will induce large flux-flow voltages along the wire at low currents, resulting in a substantial decrease in I_c. Also the associated flux-flow resistivity will be strongly field dependent as observed in the above studies.

Details of the mechanism are not so clear in NbTi, however, nor in Nb_3Sn at low strains where the degradation is reversible and I_c enhancements sometimes occur.[7] For these cases, the critical current could be affected by two general types of changes within the superconductor -- either by a shift in the intrinsic critical temperature and field, or by an alteration of the vortex-pinning structure.

Stress-induced band structure changes and/or martensitic transformations are possible and it is conceivable that these would lead to critical temperature-field properties different enough to produce the observed changes in I_c. However, the effect would have to be unusually reversible (for the martensitic transformation) and produce at least a 20% change in I_c. I_c vs. ε vs. T data (and/or direct metallurgical observation) are needed to determine the existence of such an effect.

On the other hand, rather large changes in I_c would also be produced if the vortex pinning structure of the superconductor were altered by stress. In particular, a number of observations have been made which show the critical current of hard superconductors to increase as defect size decreases.[8] Recently it has also been experimentally shown that if the defect size is made too small (small compared with the superconducting coherence length ξ), eventually I_c stops increasing and starts to precipitously decrease.[9] Maximum vortex pinning occurs when the average defect size is on the order of the vortex core size, given by the Ginzburg-Landau ξ:

$$\xi(T) = 0.85(\xi_o \ell)^{1/2}(1 - T/T_c)^{-1/2} \qquad (1)$$

Here ξ_o is the BCS coherence length and ℓ the electronic mean free path. Using measured values of H_{c2} for Nb_3Sn[10,11] and Nb45Ti[12], $\xi(4.2\ K)$ may be approximately determined using the relation:

$$\xi^2(4.2\ K) = \phi_o/2\pi H_{c2}(4.2\ K) \qquad (2)$$

In Nb-45Ti, ξ(4.2 K) is found to be on the order of 5.5 nm; in Nb_3Sn, ξ(4.2 K) is approximately 4 nm. Changes in the metallurgical structure of the superconductor on this size scale will strongly affect I_c. Thus for these two superconductors, a growth in either defect strength, or defect size to the order of 10 nm would initially enhance I_c. Further defect growth under the action of strain, however, will make the defects less effective pinning centers and I_c will decrease. I_c recovery is also possible if, upon stress removal, the defect size returns toward the $\sim$10 nm level.

This general picture of vortex-defect interactions has been presented mainly to set the size-scale for further study in this area. The size-scaling mechanism is independent of the type of defect considered. Mechanical twins, martensite platelets, cell boundaries, dislocations, and grain-boundary stress fields could all serve the purpose, provided their size varied with the amount of stress applied to the superconductor. In brittle Nb_3Sn, grain boundary damage actually develops into large-scale cracks which are readily observable. In ductile NbTi, such gross defects do not develop and direct observations of the $\sim$10 nm defect structure have not yet been obtained. However, such a change in vortex-pinning structure could account for the large scale of I_c degradation in Nb_3Sn compared with NbTi, the slight enhancement in I_c at low strain levels, the reversibility of the effect at intermediate strains, and the strong dependence on magnetic field.

4.3.4 Conclusion

In summary, the experimental evidence would suggest that the source of I_c degradation is associated with the superconductor itself, rather

than with the peripheral effects such as matrix degradation, area reduction, etc. At high strains in Nb_3Sn where the degradation is irreversible, the effect is well accounted for by $\gtrsim$100 nm cracks observed in the Nb_3Sn reaction layer. Where the degradation is mostly reversible (at lower strains in Nb_3Sn and at all strains in NbTi), the effect is most likely brought about either by a shift in the intrinsic critical temperature and field, or by an alteration of the vortex-pinning. No direct observations of reversible defect behavior have yet been obtained. However, it is suggested that defect size variations on the order of a coherence length ($\sim$5 nm) could be playing an important role in this reversible regime, explaining such effects as I_c recovery and low-strain I_c enhancement.

Acknowledgments

I am grateful to A. F. Clark, F. R. Fickett, R. P. Reed, M. Suenaga, and M. J. Superczynski for a number of stimulating discussions relating to these results.

References

1. J. W. Ekin, F. R. Fickett, and A. F. Clark, "Effect of Stress on the Critical Current of NbTi Multifilamentary Composite Wire," Proceedings of the Int. Cryogenic Materials Conference, Kingston, Ontario, 1975, Adv. in Cry. Eng., Vol. 22, pp. 449-452, Plenum, New York (1976).
2. J. W. Ekin, "Effect of Stress on the Critical Current of Nb_3Sn Multifilamentary Composite Wire," Appl. Phys. Lett. 29, 218 (1976).
3. J. W. Ekin and A. F. Clark, "Effect of Strain on the Critical Current of Nb_3Sn and NbTi Multifilamentary Composite Wires," Proceedings

of the Joint MMM-Intermad. Conf., Pittsburgh, PA (1976) (to be published by the Am. Inst. of Phys.).

4. D. S. Easton and R. E. Schwall, "Performance of Multifilamentary Nb_3Sn Under Mechanical Load", Appl. Phys. Lett. (to be published).
5. See for example, J. Weertman and J. R. Weertmann, "Mechanical Properties, Strongly Temperature Dependent" in Physical Metallurgy, edited by R. W. Cahn, North-Holland Pub. Co. (1965), Chapter 16, pp. 793-804.
6. See also J. L. McDougall, IEEE Trans. on Mag. 11, 1467 (1975).
7. E. Buehler and H. J. Levinstein, "Effect of Tensile Stress on the Transition Temperature and Current-Carrying Capacity of Nb_3Sn," Jour. Appl. Phys. 36, 3856 (1965); D. Easton, Ref. 4; T. Luhman and M. Suenaga, paper W-4 in this conference.
8. See, for example, D. Dew-Hughes, in Superconducting Machines and Devices, Large System Applications, edited by S. Foner and B. B. Schwartz, Plenum, New York (1974), Chapter 2, pp. 109.
9. J. W. Ekin, "Critical Currents in Granular Superconductors," Phys. Rev. B 12 2676 (1975).
10. G. Otto, E. Saur, and H. Wizgall, J. Low Temp. Phys. 1, 19 (1969).
11. S. Foner, E. J. McNiff, Jr., B. J. Matthias, T. H. Geballe, R. H. Willens, and Corenzwit, Phys. Lett. 31A 349 (1970).
12. B. G. Lazarev, O. N. Ovchavencko, A. A. Matsakova, V. G. Volotskaya, Zh. Eksp. Teor. Fiz. 54, 1031 (1968); Trans. Sov. Phys. JETP 27, 549 (1968).

13. D. S. Easton and C. C. Koch, "Mechanical Properties of Superconducting NbTi Composites," Proc. Intl. Cry. Mat. Conf., Kingston, Ontario, 1975, Adv. in Cry. Eng., Vol. 22, Plenum, New York (1976).

14. R. P. Reed, R. P. Mikesell, and A. F. Clark, "The Low-Temperature Tensile Behavior of Copper-Stabilized NbTi Superconducting Wire," Proc. Int. Cry. Mat. Conf., Kingston, Ontario, 1975, Adv. in Cry. Eng., Vol. 22, Plenum, New York (1976).

Current transfer in multifilamentary superconductors. I. Theory[a),b)]

J. W. Ekin

Cryogenics Division, Institute for Basic Standards, National Bureau of Standards, Boulder, Colorado 80302

(Received 21 February 1977; accepted for publication 10 January 1978)

In short-specimen critical current measurements, inadequate separation between current and voltage contacts results in a finite linear slope in the measured voltage-current characteristic at low currents. A simple approximate analytic expression is developed for estimating the magnitude of this slope from wire parameters. Current-transfer lengths are evaluated for multifilamentary NbTi and Nb_3Sn composite superconductors.

PACS numbers: 74.60.Jg, 74.70.Dg, 74.70.Lp, 85.25.+k

I. INTRODUCTION

In multifilamentary superconducting wires, there is a resistive transition from the superconducting to normal state as current through the wire is increased above the critical current [Fig. 1(a)]. This resistive transition is highly variable from wire to wire; for magnet design it must be measured in order to determine operating currents, cooling requirements, and internal heat-transfer conditions. Often this involves measurement of very low wire resistivities (10^{-12} Ω cm or less), especially when the Joule heating requirements of the magnet system are stringent.

An experimental problem in performing such measurements on *short-specimen* multifilamentary composites is that an additional voltage can be generated near the current contacts as the current penetrates the normal matrix material from the outer to the inner superconducting filaments [Fig. 1(b)]. This current-transfer voltage can be significant over surprisingly long distances from the current contacts, 10—100 wire diameters or more, depending on the particular superconductor and application. In this paper, we derive a simple approximate formula for quantitatively estimating the magnitude of current-transfer effects. This theoretical result will be compared with an experimental study of current transfer in the following paper.[1]

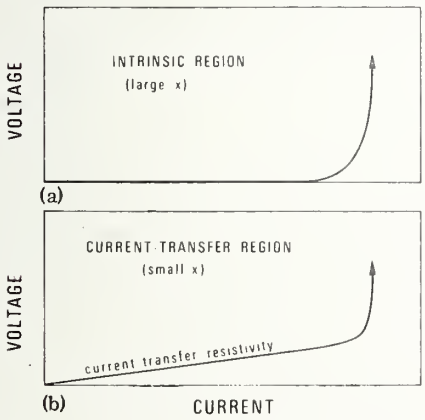

FIG. 1. Schematic representation of the superconducting composite's *V-I* characteristics in two regions: (a) far from the current contact where the wire undergoes the usual resistive transition as I approaches I_c and (b) near the current contact where the characteristic exhibits a linear region at low currents.

In Sec. II, a model first presented by Wilson[2] is used to calculate the electric field $E(x)$ along a wire due to current transfer among the filaments within the wire. In Sec. III, it is shown that for most practical purposes, the integral equation for $E(x)$ from Sec. II can be reduced to a simple analytic expression. This is then used to determine an apparent resistivity from current transfer, $\rho(x)$, and a current-transfer length x_{min}, where the latter is defined as the distance along the wire needed for $\rho(x)$ to decay to a negligible value. In Sec. IV, x_{min} is calculated for multifilamentary NbTi and Nb_3Sn. In Sec. V, the effect of current transfer on the shape of the superconductor voltage-current characteristics is discussed.

II. MODEL EQUATIONS

In this section, a model originally presented by Wilson in an unpublished lab note[2] is used to derive an integral expression for the current-transfer electric field. In Wilson's model, it is assumed that current is fed in from the outer radius of a multifilamentary superconducting composite. In particular, the transfer of current between two concentric filament rings is considered, each of mean radius r_1 and r_2 and thickness t_1 and t_2; see Fig. 2. If a current $\Delta J_1 2\pi r_1 t_1$ crosses from ring 1 to ring 2 over a distance Δx, the resulting potential difference between the two rings is

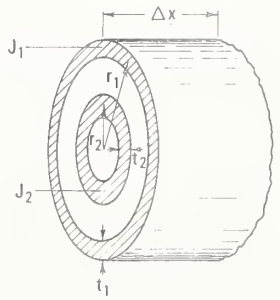

FIG. 2. Schematic representation of current transfer between two concentric rings of superconducting filaments.

[a)] Contribution of the National Bureau of Standards.

[b)] Supported by the Naval Ship Research and Development Center, Annapolis, Md and the NBS Superconducting Standards Program.

$$V_1(x) - V_2(x) = -(\Delta J_1/\Delta x) r_1 t_1 \rho_m \ln(r_1/r_2), \tag{1}$$

where ρ_m is the transverse resistivity of the matrix.

J_1 can be related to J_2 by applying the boundary conditions that the total current in the rings is constant and that at $x=\infty$ the current density in the conductor becomes uniform and equal to J_∞. This yields

$$J_1 r_1 t_1 + J_2 r_2 t_2 = J_\infty (r_1 t_1 + r_2 t_2). \tag{2}$$

Current will not penetrate to the inner ring of filaments unless the resistance of the outer superconductor filaments becomes comparable to the matrix resistance separating the filaments. This will occur when the current density J in the outer filaments approaches the critical current density. The filaments will then exhibit the usual resistive transition behavior, which for this calculation is assumed to be given by the empirical formula

$$\rho = kJ^n, \tag{3}$$

where ρ is the effective resistivity of the superconducting composite layer, J is the current density, and n is a constant representative of the material being considered (e.g., $n=30$ is typical for NbTi [2]). The proportionality constant k may be determined from a specific value of the resistivity at some arbitrary current density; for example, the effective resistivity ρ_∞ at J_∞ yields

$$k = \rho_\infty / J_\infty^n. \tag{4}$$

Using Eqs. (3) and (4), the electric field along the outer ring in the x direction can be represented by

$$\begin{aligned} E_1(x) &= -\frac{dV_1}{dx} \\ &= \rho_1(x) J_1(x) \\ &= \frac{\rho_\infty J_1(x)^{n+1}}{J_\infty^n}, \end{aligned} \tag{5}$$

and along the inner ring it is

$$\begin{aligned} E_2(x) &= -\frac{dV_2}{dx} \\ &= J_2(x)\rho_2(x) \\ &= \frac{\rho_\infty J_2(x)^{n+1}}{J_\infty^n}. \end{aligned} \tag{6}$$

Differentiating Eq. (1) with respect to x and combining with Eqs. (2), (5), and (6), there results

$$\frac{d^2 J_1}{dx^2} \frac{r_1 t_1 \rho_m}{J_\infty \rho_\infty} \ln\left(\frac{r_1}{r_2}\right) = \left(\frac{J_1}{J_\infty}\right)^{n+1} - \left(1 + \frac{r_1 t_1}{r_2 t_2} - \frac{J_1}{J_\infty}\frac{r_1 t_1}{r_2 t_2}\right)^{n+1}. \tag{7}$$

Let us define the following parameters:

$$\lambda^2 \equiv \frac{r_1 t_1 \rho_m}{\rho_\infty} \ln\left(\frac{r_1}{r_2}\right), \tag{8}$$

$$y \equiv \frac{J_1}{J_\infty}, \tag{9}$$

$$\delta \equiv \frac{r_1 t_1}{r_2 t_2}. \tag{10}$$

Then, after integrating and applying the boundary condition that $x=\infty$ when $y=1$, Eq. (7) becomes

$$\frac{x}{\lambda} = \left(\frac{n+2}{2}\right)^{1/2} \int_y^Y dy \left[y^{n+2} + \frac{1}{\delta}(1+\delta-\delta y)^{n+2} - 1 - \frac{1}{\delta}\right]^{-1/2} \tag{11}$$

where Y is the initial value of y at the current junction. Note from Eqs. (5) and (9) that the electric field along the outer cylinder is given by (the subscript 1 will be omitted for the remainder of this paper)

$$E = \rho J = \rho_\infty J_\infty (J/J_\infty)^{n+1} = E_\infty y^{n+1}, \tag{12}$$

where

$$E_\infty \equiv \rho_\infty J_\infty. \tag{13}$$

In this model, only two concentric annuli of filaments have been considered, whereas a practical superconducting composite contains many such rings. To obtain an exact solution, another integration should be carried out with respect to the radius, subjected to the boundary condition that the total current in the wire is constant. Also, the precise solution will be dependent on the initial current distribution at the current junction, which can vary considerably from apparatus to apparatus. All that is really needed, though, is some idea of the magnitude of current-transfer effects for apparatus design. For this purpose, the entire wire may be simply approximated by two cylinders of filaments, the outer one hollow and the inner one solid. Assume that they have equal cross-sectional area, in which case $\delta = 1$, $r_1/r_2 = 1 + r_2$, and $r_1 t_1 = \frac{1}{16} D^2$, where D is the overall radius of the wire. Then, Eq., (10) reduces to

$$\frac{x}{\lambda} = \frac{(n+2)^{1/2}}{2} \int_y^Y \frac{dy}{[y^{n+2} + (2-y)^{n+2} - 2]^{1/2}}, \tag{14}$$

where

$$\lambda = 0.23(\rho_m/\rho_\infty)^{1/2} D. \tag{15}$$

The above results are essentially those obtained by Wilson,[2] but involve several different assumptions. They are presented here to serve as a starting point for the derivation of a much simpler expression. In Eq. (14), we have used a different geometry for the relative size of the two rings comprising the wire, and in Eq. (11) no assumption has been made about the relative thicknesses of the two rings, which were assumed to be of equal thickness in the original derivation. In Secs. III–V, the integrals in Eqs. (11) and (14) are reduced to an analytic expression that should be useful for quick calculations of current transfer effects over most of the wire's length, without numerical integration or *a priori* knowledge of the wire's intrinsic resistivity (ρ_∞) and initial electric field (Y).

III. CURRENT-TRANSFER LENGTH

For short-specimen testing, an estimate is needed of how close to the current contacts the voltage taps

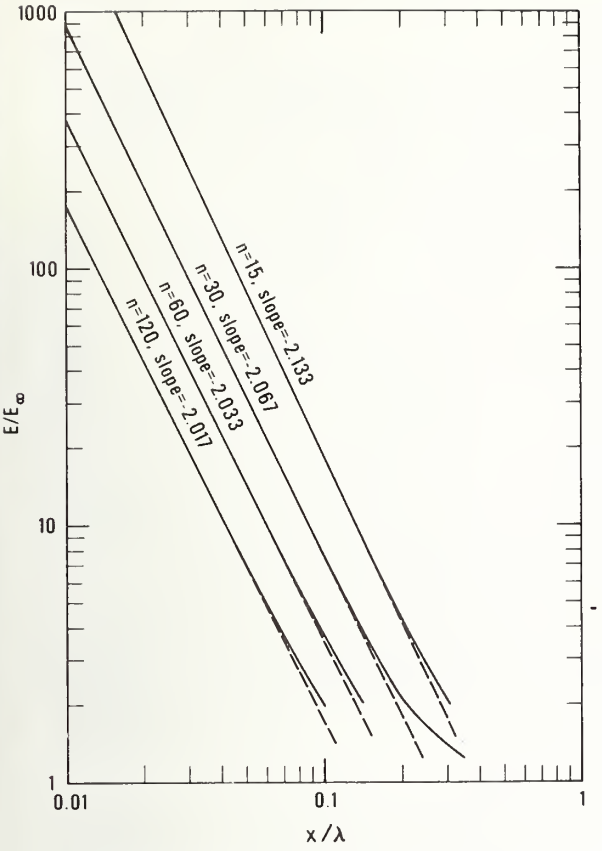

FIG. 3. Relationship between the normalized electric field from current transfer E/E_∞ and the normalized distance along the superconductor x/λ [from Eq. (17)], plotted for several values of the resistive transition parameter n [defined in Eq. (3)].

can be placed without having the current-transfer voltage interfere with measurement of the wire's intrinsic V-I characteristics. Let us denote this minimum separation as the current-transfer length x_{min}. To determine x_{min}, Eq. (14) [or alternatively Eq. (11)] has to be solved for $E(x)$. Fortunately, for most experimental situations the integral can be greatly simplified and a numerical integration avoided.

Consider the denominator of the integral in Eq. (14). For $E/E_\infty = y^{n+1} > 10$, the numerical constant (near unity) is negligible compared with the first term y^{n+2}. Furthermore, in most practical superconductors, the resistive transition is very sharp and n is large (usually 30 or more). Thus, even though $y^{n+2} \gg 1$, y is nevertheless close to unity and the middle term is a number less than unity raised to a high power. Consequently, in practice it can be neglected compared with both the first and last terms. The result is that for $E/E_\infty > 10$, Eq. (14) reduces to

$$\frac{x}{\lambda} = \frac{2}{n}\left(\frac{n+2}{2}\right)^{1/2}\left(y^{-n/2} - Y^{-n/2}\right), \tag{16}$$

or using Eq. (12),

$$\frac{x}{\lambda} = \frac{2}{n}\left(\frac{n+2}{2}\right)^{1/2}\left[(E/E_\infty)^{-n/2(n+1)} - (E/E_\infty)_{\text{initial}}^{-n/2(n+1)}\right]. \tag{17}$$

These considerations are not specific to Eq. (14) but apply to the more general integral in Eq. (11) as well (provided δ does not deviate too much from unity). Equation (11) has been evaluated numerically by Wilson for $n=30$, $(E/E_\infty)_{\text{initial}} = 10^2$ and 10^4, and several values of r_1/r_2. The difference between these specific numerical results and Eq. (17) is less than 1% for $E/E_\infty > 10$.

A graph of Eq. (17) for several values of n is shown in Fig. 3 [where we have assumed $(E/E_\infty)_{\text{initial}} \gg (E/E_\infty)$]. Also shown in this graph is the first-order correction to Eq. (17) in the region below $E/E_\infty = 10$, which we have evaluated analytically by including the constant term in the denominator of Eq. (11). The small deviation from Eq. (17) is evident at values of $E/E_\infty \gtrsim 2$. For E/E_∞ less than 2, an exact numerical integration is required. For $n=30$, where Wilson made his calculations, the numerical solution is shown. The important point, however, is that the deviation from the simple analytic form in Eq. (17) is small at all but the lowest values of E/E_∞.

Equation (17) can be simplified even further by assuming the typical case that $n \gg 1$ and $(E/E_\infty)_{\text{initial}} \gg (E/E_\infty)$. Then, we have

$$E(x)/E_\infty \cong (2/n)(\lambda/x)^2, \tag{18}$$

and taking λ from Eq. (15),

$$E(x)/E_\infty \cong (0.1/n)(\rho_m/\rho_\infty)(D/x)^2. \tag{19}$$

This result can also be expressed in terms of the effective current-transfer resistivity $\rho(x) \equiv E(x)/J(x)$. From Eqs. (12) and (13),

$$\begin{aligned} E(x)/E_\infty &= y^{n+1} \\ &= [J(x)/J_\infty][\rho(x)/\rho_\infty] \\ &= y\,\frac{\rho(x)}{\rho_\infty} \cong \frac{\rho(x)}{\rho_\infty}, \end{aligned}$$

since for $n \gg 1$, y is close to unity, even though $y^{n+1} \gg 1$. Thus, for the usual case of large n and $(E/E_\infty)_{\text{initial}} \gg E/E_\infty$, Eq. (17) reduces finally to

$$\rho(x) \cong (0.1/n)\rho_m(D/x)^2, \tag{20}$$

where n [defined in Eq. (3)] is determined by the superconductors's resistive transition, ρ_m is the transverse resistivity of the matrix, and D is the wire diameter.

It is emphasized that Eq. (20) is an approximate expression based on a simple two-cylinder model. The numerical coefficient 0.1 is dependent on the assumptions made about the initial current distribution, i.e., the size of the two cylinders. The expression should nevertheless serve to give an order-of-magnitude estimate of the current-transfer length for most practical situations.

From Eq. (20), a current-transfer length can be calculated. x_{min} is defined as the distance required for $\rho(x)$ to decay to some negligible value ρ^*. Inverting Eq. (20),

$$x_{min} = (0.1/n)^{1/2}(\rho_m/\rho^*)^{1/2}D. \tag{21}$$

The value of ρ^* will depend on the particular application. For a short-specimen apparatus, it will usually be determined by the resistivity detection limit of the

equipment. For example, if the noise in the system only permits measurement of resistivities greater than 10^{-11} Ω cm, the required separation between the current and voltage contacts may be determined from Eq. (21) by taking $\rho^* = 10^{-11}$ Ω cm. A separation greater than x_{min} is unnecessary since the specimen's resistivity could not be detected at lower levels anyway. Note also that Eq. (21) can be used to obtain some idea of the required junction length when joining two superconducting wires in a magnet. The junction must be long enough so that its resistivity is less than some acceptable level that depends on the requirements of the magnet. In this case, an estimate of the minimum junction length may be obtained from Eq. (21) by taking ρ^* to be the desired maximum resistivity of the junction.

IV. EXAMPLES

To illustrate the application of Eq. (21) to practical superconductors, the approximate current-transfer length is evaluated for multifilamentary NbTi and Nb_3Sn.

A. NbTi

The wire is assumed to consist of NbTi filaments embedded in a cold-worked "oxygen-free" copper matrix. The transverse resistivity of the matrix will consequently be about 1.4×10^{-8} Ω cm at 4 K. For NbTi, a typical value of n representing the resistive transition is $n = 30$.[2] Substituting these values in Eq. (21), the relative transfer length x_{min}/D is obtained as a function of the resistivity limit ρ^*. The results are shown in the left-hand curve in Fig. 4. Thus, for example, if the detection limit of the measurement apparatus is 10^{-12} Ω cm, a transfer length of about 7 wire diameters is needed.

B. Nb_3Sn

For Nb_3Sn wires, the wire is assumed to consist of Nb_3Sn filaments that have been reacted in a tin-bronze matrix with a residual 4 K resistivity of about 2×10^{-6} Ω cm. For the resistive transition in Nb_3Sn, a typical value for n is 60.[2] Substituting in Eq. (21), the results for the relative transfer length in a typical Nb_3Sn wire are shown by the right-hand curve in Fig. 4. From this curve, for example, it is seen that a detection limit of 10^{-12} Ω cm would require a transfer length of about 60 wire diameters.

V. VOLTAGE-CURRENT CHARACTERISTICS

Suppose the transfer length is inadequate for a particular experimental apparatus. How will this affect the apparent V-I characteristics? It is seen from Eq. (20) that the effective resistivity from current transfer is nearly independent of current magnitude. A linear V-I relationship thus would be expected, just as for a normal metal; see Fig. 1(b). Eventually at high currents, the wire's intrinsic flux-flow resistivity will dominate the current-transfer resistivity given by Eq. (20). The V-I characteristic will then deviate from its linear shape, showing the usual upturn as the critical current is approached. So, the net effect of current transfer when the transfer length is inadequate is to alter the usual flux-flow transition shown in Fig. 1(a) to that shown in Fig. 1(b). Equation (20) gives an estimate of the expected slope of the linear region.

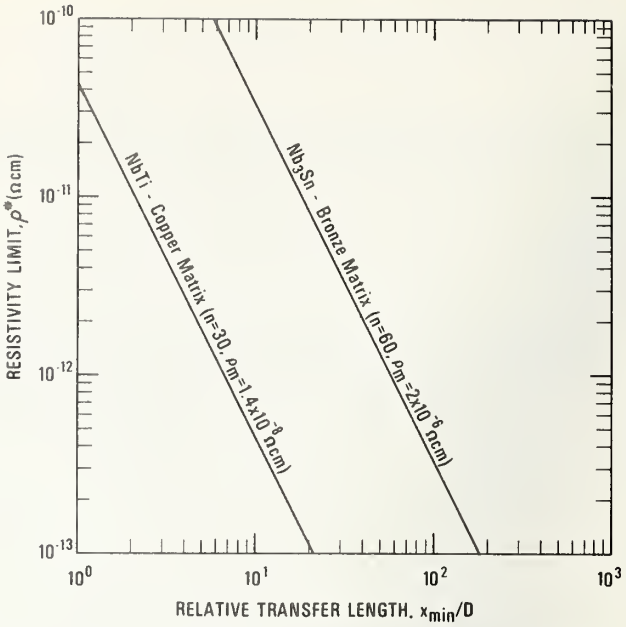

FIG. 4. Current-transfer length x_{min} for typical NbTi and Nb_3Sn multifilamentary superconductors, where D is the wire diameter and ρ^* is the resistivity limit (usually determined by the apparatus detection limit). The approximate current-transfer length for other values of n and ρ_m may be obtained from Eq. (21).

To a first approximation, intrinsic V-I data can still be obtained when measurable current-transfer effects are present. Provided the current-transfer slope does not dominate too much, the linear region can be extrapolated to high currents, and the flux-flow resistivity is taken as the difference between the measured result and this extrapolated baseline.

ACKNOWLEDGMENT

The author is grateful to Martin Wilson for helpful discussions and for communicating his lab note, Ref. 2.

[1] J. W. Ekin, A. F. Clark, and J. C. Ho, following paper, J. Appl. Phys. 49, 3410 (1978).
[2] M. N. Wilson, Rutherford Laboratory, Report SMR/1, Chilton, Oxfordshire, England, 1977 (unpublished).

Current transfer in multifilamentary superconductors. II. Experimental results[a),b)]

J. W. Ekin and A. F. Clark

Cryogenics Division, Institute for Basic Standards, National Bureau of Standards, Boulder, Colorado 80302

J. C. Ho

Physics Department, Wichita State University, Wichita, Kansas 67208
(Received 21 February 1977; accepted for publication 10 January 1978)

Measurements are reported of the current-transfer effect in a 0.58×0.68-mm NbTi (180 filament) copper-matrix wire, and in a 0.33×0.66-mm Nb_3Sn (3553 filament) bronze-matrix wire at magnetic fields from 2 to 8 T. With a voltage sensitivity of 100 nV, the effect of current transfer in the copper:NbTi wire was too small to be measured at a distance 1 cm from the current contact. In the bronze:Nb_3Sn wire, however, the effect was relatively large and resulted in voltage-current characteristics which had an extensive linear region. The slope of the linear region decreased with distance x from the current contact as $x^{-2\pm0.3}$ and reached a value of 10^{-12} Ω cm, for example, at a distance of 3 ± 0.5 cm. Both the magnitude and functional dependence of the measured current-transfer effects correspond closely to that predicted by theory.

PACS numbers: 74.60.Jg, 74.70.Dg, 74.70.Lp, 85.25.+k

I. INTRODUCTION

In this paper, experimental results will be presented which show that current transfer occurs over a length which is considerably shorter in a typical copper-matrix NbTi composite than in a similar-sized bronze-matrix Nb_3Sn composite. The approximate theoretical model presented in the preceding paper,[1] hereafter called paper I, is found to predict these results accurately.

II. EXPERIMENTAL APPARATUS

Experimentally, current penetration may be realized either by increasing the current carried by the conductor (at constant magnetic field) or by increasing the magnetic field B in order to lower the critical current density J_c (B) (with the applied current kept constant). Either method forces current transfer from the outer superconducting filaments to the inner filaments. The results reported here were obtained using the first procedure, although the data should apply approximately to the second case as well. [This is because the rate of current penetration is determined mainly by the matrix resistivity, rather than by the method for making J in the outer filaments approach $J_c(B)$; see Sec. II of paper I.]

The wire specimens were wound on a 3.8-cm-diam. Bakelite tube and inserted into a 10-T simple solenoidal magnet. The sample was mechanically held in place by wrapping it in a spiral groove cut around the circumference of the tube with a twist length of 0.42 cm (that is, the entire length of the sample was within about 3° of being perpendicular to the field). Current bus bars were soldered to the outer copper surface of the wire specimen about 3 cm from the specimen ends. 60/40 Sn-Pb solder was used, and the solder junction length was about 3 mm.

Current was supplied by a programmed 600-A current source and controlled to within 0.1%. Voltage taps were spot soldered with the same Sn-Pb solder to the specimen at several points along its length. Distance between contacts was calculated from voltage measurements obtained while the specimens were at room temperature. Voltage sensitivity for the 4 K measurements was about 100 nV.

III. SPECIMENS

Two specimens were tested. The first was a rectangular 0.58×0.68-mm NbTi:Cu (1:1.8) composite containing 180 filaments with a nominal twist length of 1.2 cm. The NbTi comprising the composite consisted of 55 wt% Nb and 45 wt% Ti, and the matrix was "oxygen-free" copper with a resistance ratio ($\rho_{293\ K}/\rho_{T_c}$) of 126.

The second specimen was a rectangular 0.33×0.66-mm Nb_3Sn:bronze composite containing 3553 filaments with a nominal filament twist length of 1.1 cm. The composite consisted of 65% bronze, ~12% Nb_3Sn, and ~5% unreacted Nb (by volume). Around the outside of the bronze – Nb_3Sn composite was an "oxygen-free" copper sheath (11% by volume), separated from the bronze by a tantalum diffusion barrier (7% by volume). The resistance ratio ($\rho_{293\ K}/\rho_{T_c}$) of the bronze matrix was 1.87, measured with the copper and tantalum removed.

From the standpoint of the present study, the major difference between the two specimens is the resistivity of the matrix material. For the NbTi composite, the entering current must penetrate an "oxygen-free" copper matrix with a 4 K residual resistivity of 1.38×10^{-8} Ω cm.[2] On the other hand, in the Nb_3Sn composite the entering current must cross copper-tantalum-bronze interfaces and then penetrate a bronze matrix with a significantly higher 4 K residual resistivity of 1.98×10^{-6} Ω cm.[2,3]

a) Contribution of the National Bureau of Standards.
b) Supported by the Naval Research and Development Center, the Air Force AeroPropulsion Laboratory, and the NBS Superconducting Standards Program.

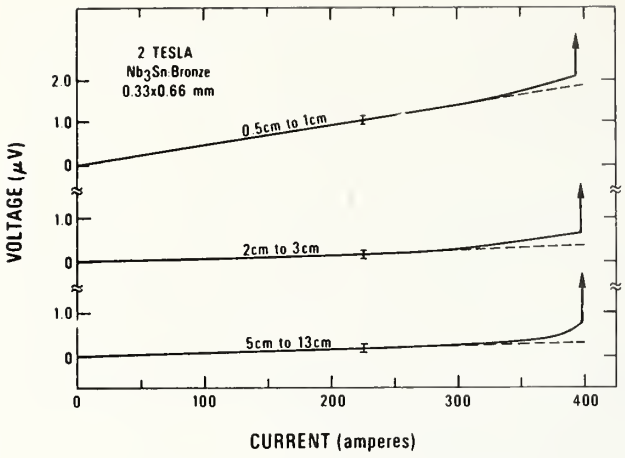

FIG. 1. Effect of current transfer on the short-specimen *V-I* characteristics. The top curve was obtained by measuring voltage between two taps located 0.5 and 1 cm from the current contact. Location of voltage taps for the middle and lowest curves are similarly indicated on the graph. Data were obtained at 2 T on a 0.33×0.66-mm Nb_3Sn bronze composite.

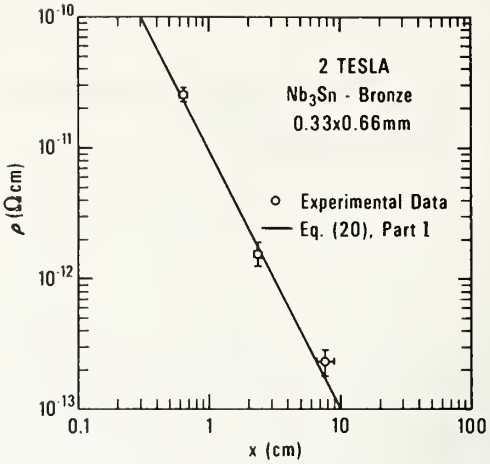

FIG. 2. Current-transfer resistivity as a function of distance x from the current contact. Data were obtained at 2 T on a 0.33×0.66-mm Nb_3Sn bronze composite. The solid line represents the theoretical result obtained by evaluating Eq. (20) of Ref. 1 using the characteristics of this specimen (i.e., an equivalent diameter D of 0.53 mm; a transverse matrix resistivity ρ_t of 1.98×10^{-6} Ω cm; $n=60$).

IV. EXPERIMENTAL RESULTS

For the NbTi specimen, we can only report an upper limit for the transfer length. For our apparatus, the voltage induced by currents in the matrix was immeasurably small, even at the voltage contact closest to the current lead. From the measurement sensitivity, we could determine that the current-transfer resistivity of this conductor dropped to less than 10^{-12} Ω cm in a distance less than 10 equivalent wire diameters, at all magnetic fields. (The equivalent wire diameter is taken to be the diameter of a round wire of equivalent cross-sectional area.)

For the Nb_3Sn specimen, however, the effective wire resistivity resulting from current transfer was significantly larger and measurable results were obtained. These are outlined below

A. *V-I* characteristics

The effect of current transfer on the *V-I* characteristics is shown in Fig. 1. The top curve represents the voltage as measured between voltage taps located 0.5 and 1 cm from the current contact. Location of the voltage taps for the middle and lowest curves are similarly indicated on the curves in Fig. 1. Note that the additional voltage generated by current flowing through the bronze matrix gives the *V-I* characteristic a finite linear slope over most of the current range. This is exactly what would be expected in the current-transfer region, based on the theoretical analysis of paper I (see Sec. V). The slope of the *V-I* characteristic in this linear region will be referred to as the *current-transfer* resistivity for the remainder of this paper. By contrast, the wire's *intrinsic flux-flow* resistivity dominates at high current levels. Here, the *V-I* characteristics show the usual nonlinear upturn as current approaches the critical current.

B. Resistivity decrease with distance

From the slope of the linear region of the *V-I* characteristics in Fig. 1, the magnitude of the current-transfer resistivity has been evaluated and plotted as a function of distance from the current contact in Fig. 2.[4] A log-log plot has been used in order to facilitate comparison with the theoretically predicted rate of decrease shown in Fig. 4 of paper I. There it is shown that the current-transfer resistivity is expected to decrease with distance from the current contact approximately as x^{-2}. In spite of the theoretical approximations involved, the data in Fig. 2 are in good agreement with this prediction. Specifically, the experimentally measured resistivity is seen to decrease with distance as $x^{-2\pm0.3}$.

Furthermore, the *absolute value* of the current-transfer resistivity predicted in paper I is in surprisingly good agreement with these data. Using Eq. (20) in Ref. 1, the theoretically expected current-transfer resistivity has been calculated for specimen II and is shown by the solid line in Fig. 2. A comparison with the experimental data shows the agreement is well within the uncertainty of the approximate calculation described in paper I.

C. Magnetic field dependence

The data presented in Fig. 2 were obtained at a magnetic field of 2 T. Similar measurements were also carried out at 4 and 8 T. All the results were essentially the same within experimental error, indicating no large magnetic field dependence. This is expected due to the relatively small magnetoresistance ($\lesssim 1\%$) of alloy materials such as Cu-Sn bronze.

For the copper : NbTi wire, on the other hand, some magnetic field dependence would be expected had we been able to measure the effect. The magnetoresistance of "oxygen-free" copper is considerably greater than bronze (30% at 2 T, 80% at 8 T), but not large enough

to permit measurement at the sensitivity level of our apparatus.

V. SUMMARY

Summarizing the experimental results, current-transfer effects have been measured in a bronze : Nb_3Sn wire specimen and were found to agree quite well with the theoretical model predictions discussed in Ref. 1. In particular, it is found that:

(1) The composite's V-I characteristics have an extensive linear region when measured by voltage taps placed near the current contact.

(2) The slope of this linear region decays with distance from the current contact as $x^{-2\pm0.3}$.

(3) The absolute magnitude of this slope agrees with that predicted by Eq. (20) of Ref. 1 to within the combined theoretical and experimental uncertainties. The magnitude of the current-transfer resistivity in other specimens with different diameters and matrix resistivities may be estimated from Eq. (20) in Ref. 1. This is only a suggested empirical procedure; the dependence on D and ρ_m have not been tested directly. However, the x dependence and absolute-value predictions of the theory from which it is derived are well substantiated by these data. Based on the evidence thus far, the procedure should provide a fairly accurate prediction of current-transfer resistivity, particularly for design of short-specimen testing apparatus and instrumentation of test coils. If current-transfer effects actually do affect the results of a particular measurement, they can be detected from the shape of the V-I characteristics (as in Fig. 1).

ACKNOWLEDGMENTS

Private communications with M. N. Wilson, D. C. Larbalestier, R. L. Powell, and F. R. Fickett are gratefully acknowledged.

[1] J. W. Ekin, preceding paper, J. Appl. Phys. 49, 3406 (1978).

[2] G. T. Meaden, *Electrical Resistance of Metals* (Plenum, New York, 1966).

[3] J. E. Magraw and D. C. Larbalestier, Rutherford Laboratory internal report SMR/14 (unpublished); F. Fickett (private communication).

[4] The average resistivity measured between two voltage contacts located at points x_1 and x_2 (x_1 closest to the current junction) is not representative of the instantaneous resistivity at a point halfway between x_1 and x_2. Rather it corresponds to a point slightly closer to x_1, due to the rapid decrease of ρ with x. In particular, the data points in Fig. 2 were plotted at a weighted point $\tilde{x}$, which we determined by iterative procedure to be $\tilde{x}^2 = x_1 x_2$. This weighting has very little effect on the data. The difference between $\tilde{x}$ and the midpoint, $\frac{1}{2}(x_1+x_2)$ is indicated by the horizontal error bars in Fig. 2.

Appendix 3

DEFINING CRITICAL CURRENT†

A. F. Clark and J. W. Ekin*

ABSTRACT

The critical current of a practical superconductor can be defined in a variety of ways such as a specific voltage level, an apparent resistivity, or even the point of the irreversible superconducting-to-normal transition. The resultant values may differ very little or be meaningless for one given condition, but when comparing superconductors under a variety of conditions, such as different magnetic fields or applied stresses, these various definitions can give apparently different behavior. This is illustrated using data on the effects of stress on the critical current behavior in wires. As part of an initial effort at the National Bureau of Standards to develop standard practices and definitions for practical superconductors, several critical current criteria are proposed and discussed.

INTRODUCTION

The transition between superconducting and normal states is a topic of more than just academic interest. Superconductivity is finding acceptance in fields such as high energy physics, power transmission and storage, rotating electrical machinery, and controlled thermonuclear fusion. Thus, practical superconductors must not only be characterized under a variety of operating conditions but their production must be monitored, design criteria established, and specifications prepared for the tons of material to be used. At the National Bureau of Standards we are attempting to develop standard definitions and practices for practical superconductors, and it is the purpose of this paper to stimulate discussion on one of the superconducting parameters, the critical current.

A variety of criteria have been used to define the current at which a practical superconductor is no longer superconducting. This is because the current-voltage (I-V) characteristic for most practical superconductors is not a step function but shows a rising voltage with current until enough heat is generated to initiate an irreversible thermal runaway. The current at this point of thermal runaway has been used as the critical current, but it is strongly dependent on the current ramping rate, the cooling medium, and the specific test configuration. It is also of little value in defining operating criteria. An experimentally easy definition is one based on a minimum detectable voltage, but it, too, depends strongly on the experimental equipment and sample configuration. A voltage level does have the advantage of being sensitive to shape changes in the I-V characteristics and usable over wide ranges of current values. Apparent resistivity is commonly used because it is intrinsic to the conductor, and a constant power criterion is sometimes used because of its applicability to heat removal.

All of these criteria and many related ones have been used in the literature with a variety of experimental conditions and make comparisons extremely difficult. In the remainder of the paper these various criteria are discussed, their effect on a sample of data will be shown, other factors are considered, and some conclusions regarding their use are presented.

Manuscript received August 17, 1976.

*Cryogenics Division, National Bureau of Standards, Boulder, Colorado 80302.
†Contribution of NBS, not subject to copyright.

THE VARIOUS CRITERIA

An idealized current-voltage characteristic is shown in Fig. 1 where, as the current is increased, an increasing amount of voltage appears across the detection probes until the heat deposited in the superconductor raises its temperature above its transition temperature. The region then transforms to the normal state with a high resistance. Ideally the critical current can be defined as[1] "that electrical current, I_c, above which an ideal superconductor abruptly transforms into the normal state . . ." However, in practical superconductors the transition is seldom abrupt and no specific point on the current axis can be identified in this manner. Superimposed on the current-voltage curve in Fig. 1 are several of the common criteria used to establish a value for the critical current. These four basic kinds of criteria and their limitations are discussed below.

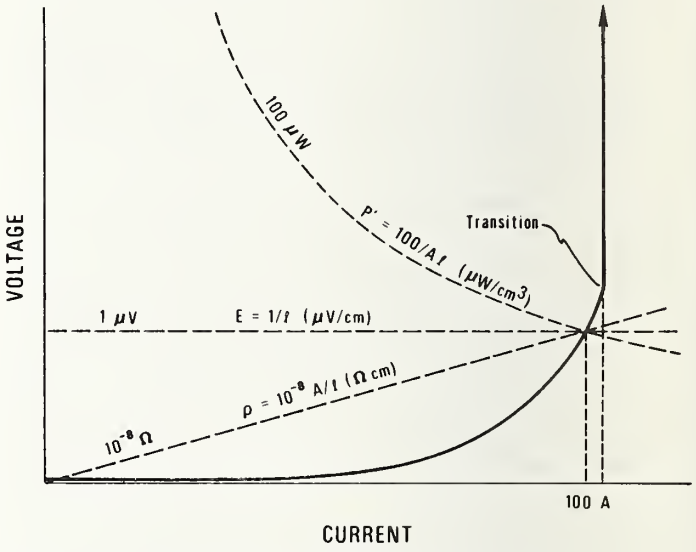

Fig. 1. The current-voltage characteristic of a practical superconductor with transition, power, electric field, and resistivity criteria for critical current.

Superconducting-to-Normal Transition

When a recorder pen slams into its stop as it flies off the chart paper, it appears to be indicating a very definitive transition. However, this point of thermal runaway on the current axis depends very strongly on the specific conductor configuration, how it is stabilized, how it is cooled, the current ramping rate, the external conditions and many more experimental parameters. Also, this transition criterion is of little value in the determination of operating currents because it must be avoided under operating conditions and gives no information about power dissipation or cooling requirements.

On the positive side, because the superconducting-to-normal transition is so readily observable and its detection requires no sensitive equipment, it is

Copyright © 1977 by The Institute of Electrical and Electronics Engineers, Inc.
Printed in U.S.A. Annals No. 701MA009

commonly used for parameterization studies. That is, in cases where the experimental conditions remain constant and only specimen variables are changed (e.g. heat treatment), the transition can provide quick comparisons. The difficulty arises on trying to compare with other work; there can be no value correspondence, only trends. This reason alone is sufficient to discourage the use of this criterion in the literature.

Voltage

A minimum detectable voltage has been traditionally used as a critical current criterion and its extension to a specified voltage level has eliminated the obvious detector dependence. It still is strongly dependent upon the experimental conditions, e.g. probe separation, and is an extrinsic property of the superconductor, depending upon the wire size, etc. A voltage criterion has the distinct advantage of being constant over a wide range of currents and, as we shall see in the example below, can be used to define critical current over the widest range of conditions.

Even further advantages are gained if the electric field, or voltage per unit length, is used. The dependence on probe separation is removed and the electric field is a property of the conductor although still not intrinsic with the material. It has also been shown by one of us[2] that the electric field in the conductor is directly relatable to the power and refrigeration requirements for a given system and thus becomes a very useful design parameter.

Resistivity

The resistivity, or resistance x(area/length), is also purely a property of the conductor and should be independent of the experimental arrangement. It still depends on the normal material-to-superconductor ratio of the specific wire configuration. (The intrinsic property of the superconductor is the "superconductor critical current density" normalized to the superconductor alone.) The resistivity can also be directly related to power requirements when multiplied by the current density, and is a useful design parameter when weight and/or size become the principal design variable (i.e. current density). The resistivity criterion has the disadvantage of not reflecting changes in the current-voltage characteristic at low current levels, and multiple values may have to be used as criteria.

Power

A power (the product of current and voltage) criterion is also insensitive at low current values, is not intrinsic to the conductor, and is very dependent on the specific configuration. Power density is, however, intrinsic to the conductor. Since the power required per unit field generated is usually the quantity of design interest, it must also be normalized by the current in order to be a design parameter. Since the superconducting-to-normal transition occurs when the heat generated can no longer be carried away (i.e. a heat transfer limit) it has also been suggested[3] that a power per unit surface area be used, particularly where cooling problems are anticipated and accurate design simulation tests are possible.

EFFECT OF CRITERIA ON DATA

As part of a program to study the effect of strain on superconductors, we have generated a family of current-voltage curves for a Nb_3Sn wire under different applied stresses as shown in Fig. 2.[4]

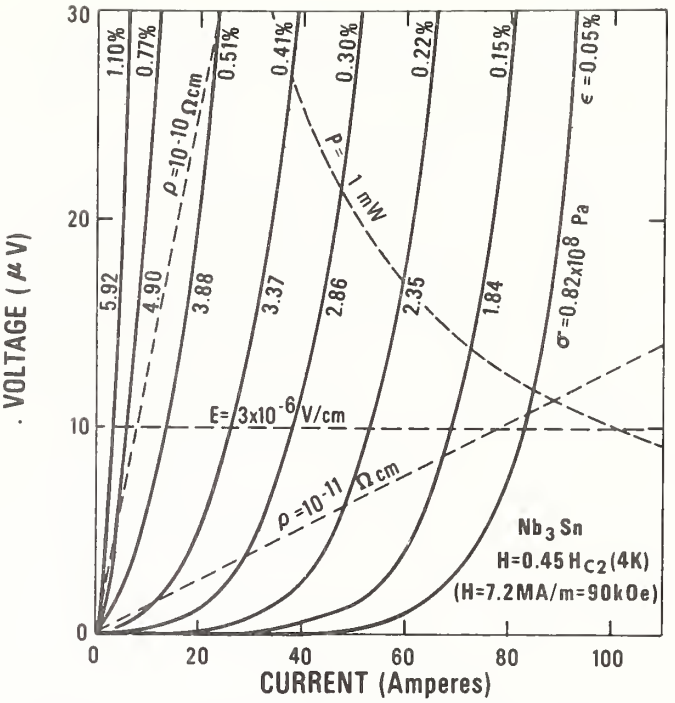

Fig. 2. The effect of stress on the current-voltage characteristic of a Nb_3Sn multifilamentary conductor.

Superimposed upon these curves are several different criteria for determining critical current values. One can see immediately how the power criterion intersects fewer of the current-voltage curves at high stresses and also how the sample's resistivity exceeds a 10^{-11} Ω cm value at high stress levels and never reaches 10^{-10} Ω cm at low stresses before going normal. All of the curves shown were reversible with current and the superconducting-to-normal transition points were taken at definite breaks in the curves (off scale in Fig. 2) where irreversibility took place.

Figure 3 shows the degradation of the critical current with applied stress utilizing transition, power, electric field, and resistivity criteria as described above. The last three criteria were picked to give similar critical current values at the lowest stress level. Note that the critical current scale is logarithmic and the degradation as determined by the different criteria varies by as much as a factor of 10. The irreversible transition values would underestimate the effect for operating conditions, the power determined values saturate and the resistivity determined values go to zero with increasing stress. Under such wide ranging conditions, the electric field determined values appear to be a good compromise, maintain sensitivity over the whole range of stress, and serve to reflect the added power dissipation requirements of a system per unit field. Conceivably there are other families of curves that would yield different results. The point to be made is that the choice of a criterion for determining critical current can dramatically affect the results of a test.

OTHER FACTORS

There are many other factors, both semantic and experimental, which we have ignored in this simple approach to the problem of defining critical current. The National Bureau of Standards will publish soon[1] a set of definitions which should alleviate some of the semantic confusion. The experimental problems are somewhat more elusive. For example, it is still undetermined how far from a current contact a voltage

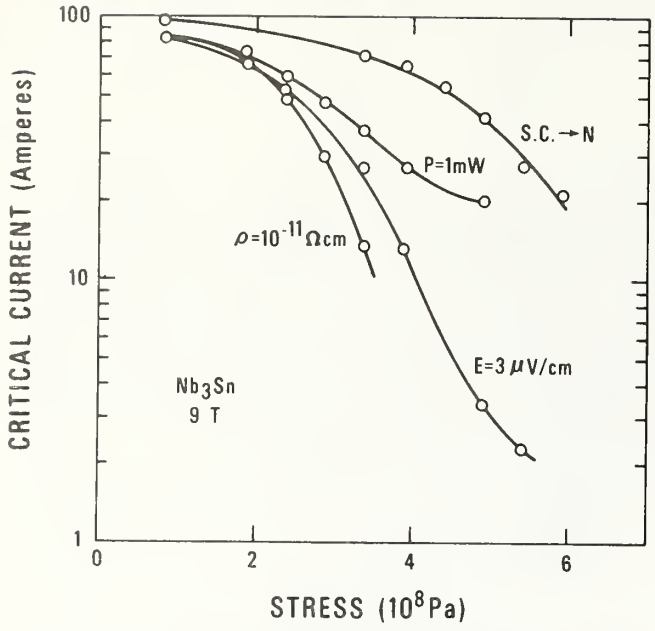

Fig. 3. The critical current of a Nb_3Sn multifilamentary conductor as a function of applied stress for various critical current criteria.

probe must be to eliminate any normal matrix resistive component due to the transfer of current into the superconductor. For that matter, the type of voltage probe, welded, soldered, or pressure, may affect the results. The mechanism of the voltage generation has not yet been clearly established much less its dependence on conductor configuration or enivronmental conditions. Current ramping rate and circuit parameters have only been mentioned and other than four-probe techniques have not. It is possible to obtain critical currents from magnetization curves[5] but only for specific configurations.

CONCLUSIONS

It has been shown that a problem in defining the critical current of practical superconductors exists. Many definitions for a variety of measurement techniques have been used and make literature comparisons extremely difficult. The electric field and resistivity criteria are the easiest to relate to both experimental conditions and system design needs. The choice of definition can dramatically affect the results of parameterization studies even when performed on a single specimen. There is a definite need to establish standard definitions and measurement techniques in this area.

ACKNOWLEDGMENTS

The authors would like to thank F. R. Fickett and R. L. Powell for helpful discussions and the latter for assistance in an accurate choice of terms. The data usedwere generated in a program sponsored by the Naval Ship Research and Development Center, Annapolis, Maryland.

REFERENCES

1. R. L. Powell, to be published, NBS report.

2. J. W. Ekin, Appl. Phys. Lett. 29, 218 (1976).

3. M. S. Walker, personal communication.

4. J. W. Ekin and A. F. Clark, Proc. Joint MMM-Intermag Conf., Pittsburgh, PA (1976), AIP Conf. Proc., to be published.

5. W. A. Fietz and W. W. Webb, Phys. Rev. 178 657 (1969).

Orthorhombic elastic constants of an NbTi/Cu composite superconductor

H. M. Ledbetter and D. T. Read*

Cryogenics Division, Institute for Basic Standards, National Bureau of Standards, Boulder, Colorado 80302
(Received 18 October 1976; accepted for publication 11 January 1977)

Elastic properties of a niobium-titanium-filament copper-matrix composite superconductor were studied experimentally at room temperature. Ultrasonic pulse and resonance measurements showed the material has orthorhombic symmetry and, therefore, nine independent elastic constants. With respect to copper, C_{11}, C_{22}, and C_{33} are about 7% lower; C_{44}, C_{55}, and C_{66} are about 15% lower; the off-diagonal elastic constants are the same; and the bulk modulus is about 5% lower. Deviations from isotropic elastic behavior are small.

PACS numbers: 62.20.Dc, 74.70.Rv, 74.30.Gn

I. INTRODUCTION

The purpose of this paper is to report a room-temperature experimental study of the elastic properties of a composite material. The study emphasizes elastic symmetry and applies familiar single-crystal methods to composites. The studied composite has unidirectional niobium-titanium (NbTi) filaments in a copper (Cu) matrix and it is designed as a superconductor for magnets. Manufacture and morphology suggest that the filament direction is an elastic-symmetry axis. Thus, the macroscopic elastic symmetry is orthorhombic, tetragonal, hexagonal, or cubic. Oblique axis systems—triclinic, monoclinic, trigonal—are excluded.

The present study shows that the studied composite is orthorhombic, but deviations from isotropy are small, and it can be referred to other coordinate axes (for example, hexagonal) without introducing large errors; advantages of this simplification are discussed in Sec. V Nevertheless, a complete set of nine orthorhombic elastic constants was determined. The elastic constants reported here may differ from those of apparently identical composites for reasons discussed in Secs. III C and V F.

Experimentally, two dynamic methods were used: pulse and resonance. Most measurements were made by a pulse method; 18 ultrasonic wave velocities were measured along the orthorhombic ⟨100⟩ and ⟨110⟩ directions. Resonance experiments were done for two reasons: to look for dispersion, the variation of sound-velocity with frequency, and to confirm the off-diagonal elastic constants.

II. WAVE MOTION IN ORTHORHOMBIC MEDIA

Usual crystallographic notations for vectors and elastic constants are used in this paper. Since all components of the studied composite are polycrystalline, the symmetries discussed here are strictly macroscopic. The filament direction of the composite is designated [001], and the principal directions perpendicular to the filaments are [100] and [010]. These directions are indicated in Fig. 1.

As stated above, the studied material has orthorhombic symmetry, and, therefore, nine independent elastic constants. These are displayed in Eq. (1) in the Voigt contracted notation in matrix form.

$$C_{ij}=\begin{bmatrix} C_{11} & C_{12} & C_{13} & 0 & 0 & 0 \\ & C_{22} & C_{23} & 0 & 0 & 0 \\ & & C_{33} & 0 & 0 & 0 \\ & & & C_{44} & 0 & 0 \\ & & & & C_{55} & 0 \\ & & & & & C_{66} \end{bmatrix}, \tag{1}$$

where the matrix is symmetrical about its main diagonal. The Christoffel equations, which relate the elastic constants to the plane monochromatic phase velocities, are[1]

$$(C_{ijkl}n_jn_k-\rho v^2\delta_{il})p_l=0, \tag{2}$$

where C_{ijkl} is the fourth-rank elastic-stiffness tensor, n is the wave-propagation direction, ρ is the mass density, v is the wave velocity, δ_{il} is the Kronecker delta,

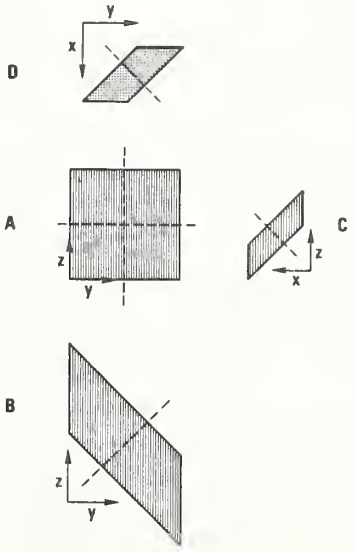

FIG. 1. Schematic geometries of four pulse specimens. Filaments along [001] are indicated by striping. The wave-propagation directions (indicated by dashed lines) and displacement vectors are given in Table I. The x, y, and z axes are equivalent to the [100], [010], and [001] axes that are used in the text and tables.

Copyright © 1977 American Institute of Physics

and p is the displacement vector. It is easy to show that the resulting secular equation is diagonal for the [100], [010], and [001] directions; that is, waves traveling along ⟨100⟩ directions are pure modes. Their velocities are determined by C_{11}, C_{55}, C_{66}; C_{22}, C_{44}, C_{66}; and C_{33}, C_{44}, C_{55}, respectively. Thus, all diagonal elastic constants, C_{ii}, can be determined by propagating waves in ⟨100⟩ directions. For each direction there is one longitudinal wave and there are two shear waves; the three waves are polarized mutually orthogonally. Thus, checks on each of the three shear elastic constants, C_{44}, C_{55}, and C_{66}, are available. The off-diagonal elastic constants C_{12}, C_{13}, and C_{23} must be determined by measurements where the n vectors are oblique to ⟨100⟩ directions.

In general, waves traveling along lower-symmetry directions are not pure modes.[2] For $\mathbf{n}=\langle 110\rangle$, there is a single pure mode whose velocity is determined by $\frac{1}{2}(C_{55}+C_{66})$, $\frac{1}{2}(C_{44}+C_{66})$, and $\frac{1}{2}(C_{44}+C_{55})$ for the [011], [101], and [110] directions, respectively. These provide additional checks on the three C_{ii} shear constants measured along ⟨100⟩ directions. The two impure modes that propagate along each ⟨110⟩ direction can be determined from the Christoffel equations.

The ⟨011⟩ propagation-direction case is now outlined. The Kelvin-Christoffel elastic stiffnesses

$$\Gamma_{il}=C_{ijkl}n_j n_k \tag{3}$$

are for the case $\mathbf{n}=(1/\sqrt{2})\,[011]$:

$$\Gamma_{il}=\tfrac{1}{2}\begin{bmatrix} C_{55}+C_{66} & 0 & 0 \\ 0 & C_{22}+C_{44} & C_{23}+C_{44} \\ 0 & C_{23}+C_{44} & C_{33}+C_{44} \end{bmatrix}. \tag{4}$$

Thus, one solution is

$$\rho v^2=\tfrac{1}{2}(C_{55}+C_{66}), \tag{5}$$

a torsion mode. And the remaining two roots are

$$\rho v^2=\tfrac{1}{2}\{C_{22}+C_{33}\pm[(C_{22}-C_{33})^2 + 4(C_{23}+C_{44})^2]^{1/2}\}+C_{44}. \tag{6}$$

Experimentally, ρv^2 is measured and C_{23} is unknown. Thus, by rearrangement,

$$C_{23}=\pm\{[2\rho v^2-\tfrac{1}{2}(C_{22}+C_{33}+2C_{44})]^2 - \tfrac{1}{4}(C_{33}-C_{22})^2\}^{1/2}-C_{44}. \tag{7}$$

The spurious second value of C_{23} from this equation can be discarded on physical grounds. Similarly, [101] and [110] planes can be used to determine C_{13} and C_{12}, respectively. For these cases

$$C_{13}=\pm\{[2\rho v^2-\tfrac{1}{2}(C_{11}+C_{33}+2C_{55})]^2 - \tfrac{1}{4}(C_{33}-C_{11})^2\}^{1/2}-C_{55} \tag{8}$$

and

$$C_{12}=\pm\{[2\rho v^2-\tfrac{1}{2}(C_{11}+C_{33}+2C_{66})]^2 - \tfrac{1}{4}(C_{22}-C_{11})^2\}^{1/2}-C_{66}. \tag{9}$$

Further details on the problem of wave propagation in orthorhombic media were given by Musgrave.[3]

III. EXPERIMENTAL

A. Material

The samples used in this study were cut from a short section of a Kryo 210 superconductor. (A trade name is used to describe the studied material; its use is not an NBS endorsement of the product.) This is a copper-matrix niobium-titanium-filament composite material. The Cu/NbTi volume ratio is 6:1, and the bar contains 2640 filaments with a twist each 7.6 cm. The filament distribution is shown in Fig. 2. The sample obtained for this study was about 20 cm long, 1.0 cm wide, and 0.5 thick. Four samples were cut for ultrasonic pulse measurements, one with its surfaces perpendicular to the symmetry axes of the material and three with the largest surface oriented at 45° to two symmetry axes. Sample geometries are shown in Fig. 1. Samples were studied in the as-received condition, that is, optimized by the manufacturer for use as a superconductor. The thermal and mechanical treatments that optimize such superconductors were described by McIntürff and Chase.[4] The specimen with {100} surfaces was 0.5 ×1.0×1.0 cm, while the three off-axis specimens had thicknesses of 5, 3, and 2 mm. All specimens were ground sufficiently flat and parallel for ultrasonic study.

B. Procedures

Eighteen ultrasonic-wave modes were studied in these four specimens at room temperature. Quartz-crystal transducers either 9.5 or 6.4 mm in diameter with fundamental resonance frequencies between 5 and 10 MHz were bonded to one specimen surface with phenyl salicylate (salol). Ultrasonic pulses were generated and detected in the transducer using an electronic apparatus described previously.[5] The time interval between the arrival of selected pulses from the ultrasonic echo train was measured using an oscilloscope with a delaying time base calibrated against a precision time-mark

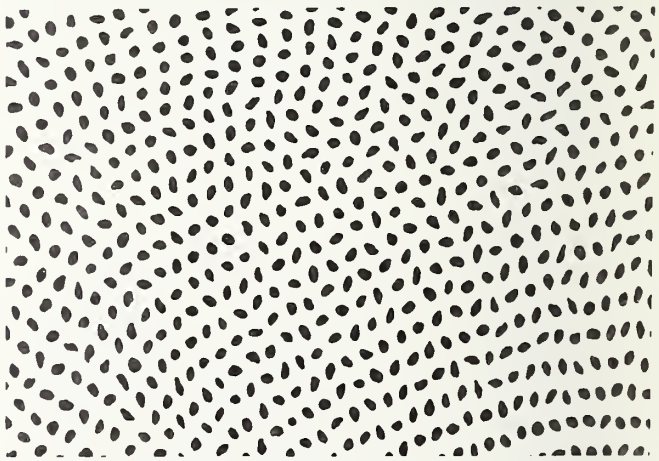

FIG. 2. Photomicrograph showing distribution of filaments. Plane of photo is perpendicular to filaments. Width shown corresponds to 4.3 mm in specimen. Vertical direction is $x=[100]$ and horizontal direction is $y=[010]$.

TABLE I. Room-temperature elastic constants C_{ij} for a NbTi/Cu composite with macroscopic orthorhombic symmetry. The wave-front normal is denoted by **n** and the displacement direction by **p**. Both ρv^2 and C_{ij} have units of 10^{11} N/m^2.

Specimen	Measurement number	n	p	ρv_l^2	ρv_t^2	C_{ij}	Derived C_{ij}
A	1	100	100	1.834		C_{11}	$C_{11}=1.834\pm0.005$
	2		010		0.404	C_{66}	$C_{66}=0.414\pm0.007$
	3		001		0.407	C_{55}	$C_{55}=0.407\pm0.011$
	4	010	010	1.878		C_{22}	$C_{22}=1.878\pm0.015$
	5		100		0.413	C_{66}	
	6		001		0.413	C_{44}	$C_{44}=0.416\pm0.003$
	7	001	001	1.880		C_{33}	$C_{33}=1.880\pm0.002$
	8		100		0.414	C_{55}	
	9		010		0.419	C_{44}	
B	10	011	011[a]	1.713		$\frac{1}{2}[C_{22}+C_{33}\pm[(C_{22}-C_{33})^2+4(C_{23}+C_{44})^2]^{1/2}]+C_{44}$	$(C_{23}=0.715)$[b]
	11		$0\bar{1}1$[a]		0.419		$C_{23}=1.041\pm0.040$
	12		100		0.407	$\frac{1}{2}(C_{55}+C_{66})$	
C	13	101	101[a]	1.740		$\frac{1}{2}[C_{11}+C_{33}\pm[(C_{11}-C_{33})^2+4(C_{13}+C_{55})^2]^{1/2}]+C_{55}$	$(C_{13}=0.809)$[b]
	14		$\bar{1}01$[a]		0.409		$C_{13}=1.039\pm0.040$
	15		010		0.408	$\frac{1}{2}(C_{44}+C_{66})$	
D	16	110	110[a]	1.744		$\frac{1}{2}[C_{11}+C_{22}\pm[(C_{11}-C_{22})^2+4(C_{12}+C_{66})^2]^{1/2}]+C_{66}$	$(C_{12}=0.804)$[b]
	17		$1\bar{1}0$[a]		0.400		$C_{12}=1.056\pm0.040$
	18		001		0.394	$\frac{1}{2}(C_{44}+C_{55})$	

[a]Impure modes.

[b]Values discarded for reasons discussed in text.

generator. The ultrasonic echo patterns obtained in this study were of good quality. They had between 3 and 30 well-defined echoes.

Using the velocity v of the ultrasonic wave (obtained from the transit time and the path length) and the specimen mass density ρ, the room-temperature elastic constants were calculated from

$$C=\rho v^2, \tag{10}$$

a simplified form of Eq. (2), where C is a combination of the C_{ij}'s depending on the mode. Results derived from Eq. (2) for the 18 modes studied here are given in Table I.

Resonant-bar elastic-constant measurements were performed on two other specimens at room temperature. These specimens were 4.8-mm-diam cylinders with lengths of 1.9 and 3.1 cm prepared with filaments along the specimen axis. In the resonant-bar technique, the sample is excited into longitudinal or torsional resonance by an attached quartz-crystal driver of appropriate mode and frequency. Resonance is detected using a quartz gauge crystal attached to the driver. The driver, gauge, and specimen form a composite oscillator. The appropriate elastic constant of the specimen can be calculated from the resonant frequency of the composite oscillator, the specimen density, and known properties of the driver and gauge crystals. Since the composite-oscillator resonant frequency is often tens of kilohertz, this technique is sometimes called a kilohertz technique, but it is called a composite-oscillator technique in the literature.[6] No correction was made for specimen geometry. According to the well-known formulas of Rayleigh, in this case, the correction multiplier is 1.003 for Young's moduli and 1.000 for torsional moduli.

C. Uncertainties

Experimental uncertainties of the elastic constants are discussed in two parts: imprecision and systematic error. Imprecisions affect many conclusions of the study; systematic errors do not; they affect only the C_{ij}'s themselves.

Bounds on the C_{ij}'s in Table I are imprecisions expressed as $\pm\sigma$, where σ is the standard deviation based on a normal distribution. For the diagonal C_{ij}'s, these imprecisions are based on two to five pure-mode measurements. Imprecisions of the nondiagonal C_{ij}'s depend both on these values and on an assumed imprecision of 0.005 in the quasitransverse values of ρv^2. Sources of imprecision include deviations of specimens from flat and parallel, specimen-length mismeasurements, specimen-to-specimen bond variations, transit-time mismeasurement, and, for this material, specimen inhomogeneity.

There are two principal systematic errors, one arising from the mass density and one from the transducer-bond coupling to the specimen. Maximum error in the mass density is estimated to be less than 0.15%. Transit-time error due to the ultrasonic wave traveling through the transducer and the coupling agent is estimated to be less than 1%; and, when corrected for, increases the ρv^2 values. Thus, the overall uncertainty in the C_{ij}'s is estimated to be less than $\pm1.5\%$.

A possible source of sample-to-sample variation in the elastic constants of any composite material is its thermal-mechanical treatment, which may vary considerably for the type of material reported on here. For example, for copper, elastic-constant differences up to 10% have been reported for annealed and deformed specimens.[7] Such variations can also occur in copper-base composites. Residual stresses of the order of the yield strength may occur in the composite, but simple

TABLE II. Elastic compliances of a NbTi/Cu composite measured by a resonance method at room temperature. Units are 10^{-11} m^2/N.

S_{ij}	Observed	Calculated from C_{ij}'s
S_{33}	0.873 ± 0.009	0.878 ± 0.073 from quasishear modes (0.692 from quasilongitudinal modes)
$\frac{1}{2}(S_{44}+S_{55})$	2.398 ± 0.024	2.430 ± 0.041

computations show that these would change the elastic constants by less than 1%.

IV. RESULTS

Results of the study are displayed in Tables I—II. In Table I the observed room-temperature values of ρv^2 are given for the 18 measurement modes. Table I also contains expressions for ρv^2 in terms of the C_{ij}'s. These expressions were derived from the Christoffel equations. When a plus-minus sign occurs, the plus sign corresponds to the longitudinal mode and the minus sign corresponds to the transverse mode. Estimated errors for the derived elastic constants are also in Table I. The basis for estimating these errors was described above.

Results of the resonance studies are in Table II. S_{33} is the reciprocal Young's modulus along the filament direction and $\frac{1}{2}(S_{44}+S_{55})$ is the reciprocal torsion (or shear) modulus around that direction.

The elastic compliances, S_{ij}'s, are given in Table III along with a summary of the C_{ij} data. The S_{ij}'s were determined by inverting the C_{ij} matrix displayed in Eq. (1) and substituting the C_{ij} values from Table I. Except for S_{44}, S_{55}, and S_{66}, which are simple reciprocals of the corresponding C_{ij}'s, errors in the S_{ij}'s are larger than those in the C_{ij}'s because of error accumulation.

The practical elastic constants (E = Young's modulus, G = shear modulus, and ν = Poisson's ratio) are given in Table IV. These parameters are related to the S_{ij}'s as

TABLE III. Room-temperature elastic stiffnesses C_{ij} and elastic compliances S_{ij} of a NbTi/Cu composite and copper. C_{ij} units are 10^{11} N/m^2 and S_{ij} units are 10^{-11} m^2/N. Values in parentheses are derived from $2C_{44}=C_{11}-C_{12}$ and $S_{44}=2(S_{11}-S_{12})$.

	Composite		Copper[a]	
ij	C_{ij}	S_{ij}	C_{ij}	S_{ij}
11	1.834	0.924	2.006	0.780
22	1.878	0.894		
33	1.880	0.879		
44	0.416	2.404	0.477	2.096
55	0.407	2.457		
66	0.414	2.415		
12	1.056	−0.341	(1.052)	(−0.268)
13	1.039	−0.322		
23	1.041	−0.307		

[a]Reference 7.

displayed in the matrix equation

$$S_{ij}=\begin{bmatrix} 1/E_{11} & -\nu_{21}/E_{22} & -\nu_{31}/E_{33} & 0 & 0 & 0 \\ & 1/E_{22} & -\nu_{32}/E_{33} & 0 & 0 & 0 \\ & & 1/E_{33} & 0 & 0 & 0 \\ & & & 1/G_{44} & 0 & 0 \\ & & & & 1/G_{55} & 0 \\ & & & & & 1/G_{66} \end{bmatrix}, \tag{11}$$

where the S_{ij} matrix is symmetrical about its main diagonal and the Poisson ratios are defined by

$$\nu_{ij}=-S_{ij}/S_{ii} \text{ (no sum)}. \tag{12}$$

V. DISCUSSION

A. Symmetry

On the basis of its internal and external geometry, the composite appears to be orthorhombic. If an object has three mutually perpendicular twofold axes, then it belongs to the orthorhombic symmetry system. These rotation axes are labeled x, y, and z in Figs. 1 and 2. Other possible symmetry systems can be excluded. Triclinic has no symmetry axis. Monoclinic has a single

TABLE IV. Practical elastic constants: E = Young's modulus, G = shear modulus, ν = Poisson's ratio for NbTi/Cu composite in different coordinate systems at room temperature. Units are 10^{11} N/m^2, except ν's, which are dimensionless.

Elastic constant	Orthorhombic basis	Tetragonal basis	Hexagonal basis	Isotropic basis	Copper[a] values	Static results[b] (hexagonal basis)
E_{11}	1.082	1.100	1.100	1.112	1.282	1.22
E_{22}	1.119					
E_{33}	1.138	1.138	1.138			1.19
G_{44}	0.416	0.411	0.411	0.412	0.477	0.448
G_{55}	0.407					
G_{66}	0.414	0.414	(0.398)[c]			(0.431)[c]
ν_{21}	0.381	0.381	0.381			0.415
ν_{31}	0.365	0.357	0.357			0.347
ν_{32}	0.349					

[a]Reference 7.
[b]Reference 8.
[c]Quantities in parentheses are derived from given data using $G_{66}=E_{11}/2(1+\nu_{12})$.

TABLE V. Checks for various symmetries for NbTi/Cu composite. For hexagonal and cubic cases, relationships (1), (2), and (3) also hold. For an isotropic case, all eight relationships must hold, either (4) or (8) is redundant.

Symmetry system	Relationships	Ratio of LHS/RHS for NbTi/Cu
Tetragonal	(1) $C_{22}=C_{11}$	1.024 ± 0.020
	(2) $C_{55}=C_{44}$	0.978 ± 0.014
	(3) $C_{23}=C_{13}$	1.002 ± 0.040
Hexagonal	(4) $C_{66}=\frac{1}{2}(C_{11}-C_{12})$	1.064 ± 0.020
Cubic	(5) $C_{33}=C_{11}$	1.025 ± 0.007
	(6) $C_{12}=C_{13}$	1.016 ± 0.040
	(7) $C_{66}=C_{55}$	1.017 ± 0.018
Isotropic	(8) $C_{44}=\frac{1}{2}(C_{11}-C_{12})$	1.069 ± 0.016

twofold axis. Trigonal has a single threefold axis. Clearly, these three systems are less symmetrical than the composite.

Orthorhombic symmetry includes four other symmetry systems: tetragonal, hexagonal, cubic, and isotropic. Relationships among the C_{ij}'s for these systems are given in Table V together with tests of the relationships. Clearly, from Table V, none of the higher-symmetry systems can be used to describe exactly the observed C_{ij}'s, but the deviations are small for any of these four symmetry choices. The advantage of describing an object by its highest symmetry is that there are fewer independent elastic constants: six for tetragonal, five for hexagonal, three for cubic, and two for isotropic. Thus, measurements and calculations are simplified to various degrees. In Table IV, present orthorhombic results are also expressed in higher-symmetry coordinates to facilitate comparisons with other studies. When necessary, elastic constants were simply averaged.

B. Off-diagonal elastic constants

The off-diagonal ($i \neq j$) elastic constants are more difficult to determine and almost always have higher uncertainties than the diagonal ($i=j$) elastic constants. This problem is reflected in the present study in Table I. The problem arises because the off-diagonal elastic constants are not related simply to any pure mode of mechanical deformation. This is best shown in the S_{ij} matrix displayed in Eq. (11). All the diagonal S_{ij}'s are related reciprocally to either a Young's modulus or to a shear modulus; but all the off-diagonal S_{ij}'s are related to a Young's modulus and a Poisson's ratio, which is in turn determined by two other elastic constants, as shown in Eq. (12).

In the present study, another difficulty arose in determining the off-diagonal elastic constants. As shown in Table I, different values of the off-diagonal C_{ij}'s were obtained depending on whether the observed ρv_l^2 or the observed ρv_t^2 was substituted into the appropriate C_{ij} expression given in the table. For example, in the [011] direction the quasitransverse datum gave $C_{23}=0.715$, while the quasilongitudinal datum gave $C_{23}=1.041$. The C_{12} and C_{13} cases are similar. On the basis of small imprecisions of the measurements and on the basis of the correctness of the value of the third (pure shear) mode, it seemed that the off-diagonal terms should be less uncertain than this and that one of two values was perhaps correct.

To resolve this uncertainty in the off-diagonal elastic constants, an independent experiment was done: some of the S_{ij}'s were determined by a resonance method. Dilatational and shear modes were measured on a cylindrical specimen with filaments along the cylinder axis. Results shown in Table II for the torsional mode $\frac{1}{2}(S_{44}+S_{55})$ agree exactly with the value calculated from the C_{ij}'s. (The S_{ij}'s are computed from the C_{ij}'s by inverting the C_{ij} matrix). Similarly, exact agreement is also obtained for the dilatational mode S_{33} if the C_{ij} data from quasitransverse modes rather than quasilongitudinal modes are used. Thus, it was concluded that the quasitransverse velocity data are both correct and consistent with other data. However, the quasilongitudinal wave velocities are low by about 5%. This slowing can be interpreted as a longer path length in the specimen due to interactions between the quasilongitudinal waves and internal boundaries due to the presence of filaments.

C. Comparison with copper

It is useful to compare the elastic constants of the composite with those of the matrix material, unalloyed copper,[7] to determine the effects of the filaments. Comparative data are shown in Table IV. Both the Young's moduli and the shear moduli of the composite are about 15% lower than those of copper. The compressibility,

$$K=\tfrac{1}{9}\sum_{i,j=1,3} S_{ij}, \tag{13}$$

of the composite is about 5% higher. The off-diagonal C_{ij}'s are identical to the value for copper, within 1%. This result may be accidental since it has no obvious physical interpretation.

D. Comparison with previous studies

The elastic constants of this composite were measured by Sun and Gray[8] using static methods, assuming hexagonal symmetry, and their results are shown in Table IV. Considering the higher inaccuracies usually associated with static methods, the agreement between the two sets of data is surprisingly good. The static Young's and shear moduli are up to 9% higher than the values reported here. The largest discrepancy is in ν_{21} and is due probably to error accumulation in the computed static value. Possibly, the differences in the two data sets are real, but this cannot be decided without knowing the uncertainties of the static values. A real difference is unlikely because, ignoring dispersion effects, dynamic elastic moduli are almost always higher than static elastic moduli, and the opposite effect is observed in this case.

E. Dispersion

No dispersion effects were observed, either in the limited 5—10-MHz region that was studied or in com-

paring the MHz pulse data with the 60-kHz resonance data. By dispersion is meant the dependence of sound velocity on frequency. Dispersive effects have been reported in many composite materials; they are usually due to either relaxation or resonance effects. Their absence here is attributed to assumed coherent interfaces between the filaments and the matrix and to the small difference in acoustic impedance between the filaments and the matrix. Absence of dispersion is also consistent with the well-defined echo patterns that were obtained.

F. Relationship to similar composites

Elastic-property data have not been reported for NbTi/Cu composites with different ratios of NbTi or with different thermal-mechanical treatments. The present data can be applied to other NbTi/Cu composites through predictive schemes that relate the elastic constants of a composite to those of its components. Using the values of the NbTi elastic constants given by Sun and Gray[8] and formulas summarized by them, it follows that the present material obeys *approximately* simple rules of mixtures. Thus, similar composites would also be expected to follow these rules approximately. The present study is a useful guide to the elastic properties of any NbTi/Cu composite, but it is a source of exact elastic data only for the particular material studied. Even when the filament matrix volume ratio is adjusted for, several other variables remain that can affect elastic properties. These include the state of mechanical deformation (the number and distribution of lattice defects), composition of the NbTi filaments, preferred orientations in either the filaments or the matrix, and degree of coherency of the filament-matrix interfaces.

G. Low-temperature elastic constants

Since this composite is intended for use as a superconductor, its low-temperature elastic properties are important. Studies down to liquid-helium temperature are underway in our laboratory and results will be reported subsequently. Preliminary results are that the composite behaves on cooling *approximately* like unalloyed copper; but the magnitudes of the elastic constant changes are slightly different and there are some anomalous effects that are both reproducible and reversible.

VI. CONCLUSIONS

The chief results and conclusions of this study are as follows:

(1) Ultrasonic (5—10 MHz) waves, both dilatational and shear, can be propagated in an NbTi/Cu composite in directions parallel, perpendicular, and oblique to the filaments.

(2) Except as noted below, usual single-crystal elasticity techniques could be used to establish the complete set of elastic constants of the composite.

(3) Longitudinal waves propagated obliquely to ⟨100⟩ directions have velocities about 5% lower than expected. Obliquely propagated shear waves travel at their expected velocities.

(4) The studied composite has orthorhombic symmetry and, therefore, nine independent elastic constants; but the deviations from isotropy are small.

(5) Compared to copper, the C_{ij}'s $(i=j)$ of the composite are lower by about 7% for C_{11}, C_{22}, and C_{33}, and by about 15% for C_{44}, C_{55}, and C_{66}; but the C_{ij}'s $(i\neq j)$ are about the same. The composite's compressibility is about 5% higher than copper's.

(6) The present dynamic results agree reasonably well with existing static measurements.

(7) Advantages of combining pulse-echo measurements and resonance measurements were found.

(8) No dispersion, change of velocity with frequency, was observed.

ACKNOWLEDGMENTS

This study was supported by the Advanced Research Projects Agency of the U.S. Department of Defense. G.A. Miranda of Los Alamos kindly contributed a photomicrograph of the studied material. W.H. Gray of Oak Ridge National Laboratory contributed a critical reading of the manuscript.

*NRC-NBS Postdoctoral Research Associate, 1975—1976.

[1]L.D. Landau and E.M. Lifshitz, *Theory of Elasticity* (Pergamon, London, 1959), p. 104.
[2]J.R. Neighbors and G.E. Schacher, J. Appl. Phys. 38, 5366—5375 (1967).
[3]M.J.P. Musgrave, *Crystal Acoustics* (Holden-Day, San Francisco, 1970), p. 117—123.
[4]A.D. McInturff and G.G. Chase, J. Appl. Phys. 44, 2378—2384 (1973).
[5]E.R. Naimon, W.F. Weston, and H.M. Ledbetter, Cryogenics 14, 246—249 (1974).
[6]J. Marx, Rev. Sci. Instrum. 22, 503—509 (1951).
[7]H.M. Ledbetter and E.R. Naimon, J. Phys. Chem. Ref. Data 3, 897—935 (1974).
[8]C.T. Sun and W.H. Gray, Sixth Symposium on Engineering Problems of Fusion Research, San Diego, Calif., 1975 (unpublished); W.H. Gray and C.T. Sun, Oak Ridge National Lab. Report TM-5331, 1976 (unpublished).

Temperature dependence of the elastic constants of an NbTi/Cu superconducting composite

D.T. READ and H.M. LEDBETTER

Low-temperature elastic properties are reported for a commercial superconducting composite consisting of niobium-titanium filaments in a copper matrix. Both an ultrasonic (10 MHz) pulse-superposition technique and a composite-oscillator (100 kHz) technique were used. Seven of the composite's nine independent elastic constants were determined between 76 and 300 K; Young's modulus along the filament axis and a shear modulus perpendicular to that axis were determined between 4 and 300 K; all showed irregular temperature behaviour.

Superconducting composites consisting of niobium/titanium filaments in a copper matrix are now available commercially for applications in which high electrical-current density must be obtained in high magnetic fields. Current-carrying capacity of these conductors can be degraded by very small strains, which may arise from the large forces to which components containing these conductors are often subjected. Reinforcing materials for strain relief consume valuable space in a cooled volume; cool-down costs and fabrication are further disadvantages of excess reinforcement. Thus, mechanical design of large components containing superconductors must be optimized. Elastic constants of such conductors are useful for two reasons: for computing the recoverable deflections due to applied loads, and for computing thermoelastic stresses due to either temperature changes or differential thermal contractions. Also elastic constants provide a valuable characterization of a material. For composites, accurate elastic data provide key tests for theories that relate macroscopic elastic properties to the elastic properties of the constituents.

The particular NbTi/Cu composite reported here has orthorhombic symmetry, and the room temperature values of all nine independent elastic constants, the C_{ij}'s have been reported previously.[1] The present study determined the temperature dependences to 77 K of seven elastic constants: C_{11}, C_{22}, C_{33}, C_{55}, C_{66}, E_{33}, and $2/(S_{44} + S_{55})$, where E_{33} is Young's modulus along the filament axis and $2/(S_{44} + S_{55})$ is the torsion modulus about that axis. Two elastic constants, E_{33} and C_{66}, were determined to 4 K. The temperature dependences of the other elastic constants, such as C_{12} and C_{13}, were not determined because they are measured indirectly and they have larger errors. Symmetries discussed here are strictly macroscopic. The filament direction of the composite is designated [001], and the principal directions perpendicular to the filaments are [100] and [010]. These directions are indicated in Fig. 1.

Cryogenics Division, Institute for Basic Standards, National Bureau of Standards, Boulder, Colorado, USA.

EXPERIMENTAL

Material

Specimens were cut from a sample bar of a commercially available multifilamentary superconductor, a copper matrix, niobium/titanium-filament composite. The sample obtained for this study was about 200 mm long, 10 mm wide, and 5 mm thick. The material was studied in the as-received condition. Thermal and mechanical manufacturing treatments of such superconductors have been described by Critchlow, Gregory, and Zeitlin.[2] The Cu/NbTi volume ratio of the conductor is 6 : 1, and the bar contains 2640 filaments with a twist pitch of 76 mm. The NbTi filaments contain 45% by weight of titanium. Four specimens were cut for ultrasonic pulse measurements, one with its surfaces perpendicular to the symmetry axes of the material and three with their largest surface oriented at 45° to two symmetry axes. Specimen geometries are shown in Fig. 1. The specimen with {100} surfaces was 5 mm by 10 mm by 10 mm, while the three off-axis specimens had thicknesses of 5 mm, 3mm, and 2 mm. All four specimens were ground sufficiently flat and parallel for ultrasonic study. Two composite-oscillator specimens were prepared. These were right circular cylinders 4.8 mm in diameter and 31 mm and 19 mm long for the extensional and torsional measurements, respectively.

Procedures

The temperature dependences of five of the elastic stiffnesses, C_{11}, C_{22}, C_{33}, C_{55}, and C_{66}, were measured using a pulse-superposition technique in which the ratio of the ultrasonic velocity, v, at low temperatures to its value at room temperature was measured every five degrees between room temperature and the lowest temperature obtained during each cooling. These ratios of sound velocities were used to compute the temperature dependence of the appropriate elastic constant, C, from $C = \rho v^2$ where ρ is the specimen's mass density. Each specimen was cooled by enclosing it in a chamber and lowering it gradually into the

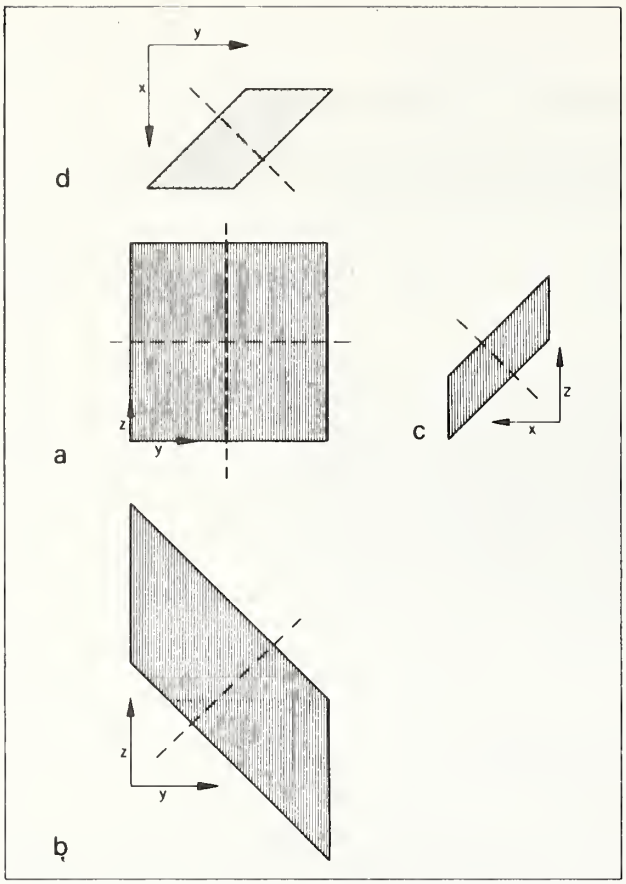

Fig. 1 Schematic geometries of four pulse specimens; filaments along [001] are indicated by striping. In specimen a, waves were propagated along the [100], and [010] directions; in b along [011]; in c along [101]; and in d along [110]

ullage of a Dewar containing either liquid nitrogen of liquid helium. The low temperature apparatus and techniques have been described previously.[3]

The temperature dependence of the Young's modulus and the torsional modulus were measured using a composite-oscillator technique. Briefly, the resonant frequency is measured of a composite oscillator consisting of a specimen, a quartz crystal driver, and a quartz crystal gauge. This composite oscillator is also cooled by insertion into a chamber and lowering into the ullage of a Dewar. The resonant frequency of the specimen is computed from the resonant frequency of the composite oscillator, the masses and geometries of the specimen and the quartz crystals, and resonant frequencies of the gauge and quartz crystals. From its resonant frequency, the elastic constant of the sample can be computed simply. The apparatus and techniques used in such measurements have been described previously.[4]

Errors

Errors in the reported low temperature moduli arise from errors in the measured ultrasonic transit times, the resonance frequencies, and the temperature. Relative transit time errors are estimated to be about $\pm 1 \times 10^{-5}$; relative resonance frequency errors are estimated to be $\pm 1 \times 10^{-4}$. Modulus errors due to temperature mismeasurement are estimated to be much less than one percent.

Systematic errors are the major sources of uncertainties in the present results. Sources of these are: errors in the room temperature modulus values, changes of the specimen density and length with temperature, variation of the Cu/NbTi ratio across the cross sections of the specimens, and errors arising from the twist pitch of the filaments in the superconductor. Errors in the room temperature moduli were reported previously.[1] These errors are ± 1.5%, and they are the source of almost all the uncertainty in the low temperature moduli. Due to cancellation of lengths in the density and velocity in the relationships used to compute the moduli, each low temperature modulus has an error equal to the length change of the specimen between room temperature and the measurement temperature. The maximum thermal contraction modulus error can be estimated by assuming copper's expansivity; this gives a maximum thermal contraction error, at 4 K, of 0.3%. The sound waves used in this study traversed only part of the cross-section of the composite superconductor. The Cu/NbTi ratio varied over the cross-section of the specimen; no filaments occur at the centre or at the perimeter of the conductor. The variation of the ultrasonic velocity across the specimen was determined by making velocity measurements with a transducer positioned either at the centre of the specimen or off-centre. Both longitudinal-wave and shear-wave velocities were checked, and no significant differences were found. This lack of dependence of ultrasonic velocity on position indicated that the specimens could be considered homogeneous units; the microscopic basis for this behaviour was not studied. An equation derived by Whitney[5] was used to compute the effect of twist pitch of the fibres on the Young's modulus, and it was found to be about 0.03%. This value is useful as a qualitative estimate of the effect of twist pitch on all the moduli; it shows that twist pitch errors are negligible in specimens

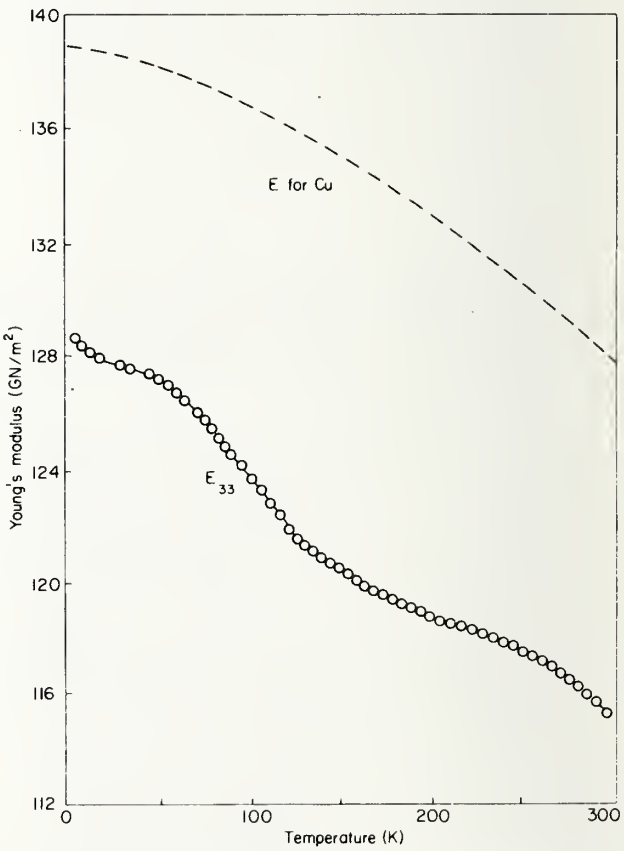

Fig. 2 The variation with temperature of the Young's modulus of an NbTi/Cu composite along [001] compared with the Young's modulus behaviour of polycrystalline copper

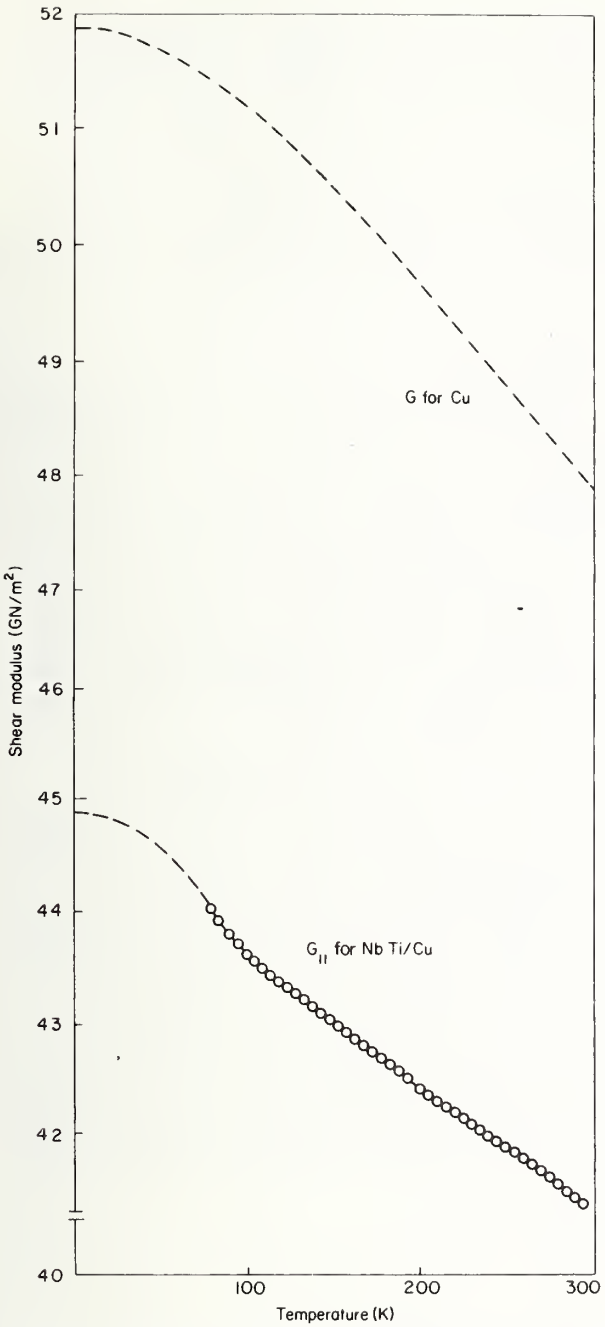

Fig. 3 The variation with temperature of the shear, or torsional, modulus of an NbTi/Cu composite around the [001], or filament, axis compared with the shear modulus behaviour of polycrystalline copper

shorter than one twist length. Thus, the total uncertainty of the reported moduli values is estimated to be ± 2%.

RESULTS

The measured value of E_{33} (Young's modulus along the filament direction) is shown in Fig. 2; Young's modulus, E, of polycrystalline copper is shown for comparison. The copper values were obtained from the single-crystal data of Overton and Gaffney[6] using the arithmetic average of the Hashin-Shtrikman bounds. The composite's Young's modulus is about ten percent lower than copper's, and it increases about ten percent during cooling from room temperature to 4 K. Irregularities in the composite's temperature behaviour are significant deviations from the temperature dependence of Young's modulus of typical materials; the upturn in the curve below 20 K is believed to be real.

The values of $2/(S_{44} + S_{55})$, the modulus of torsion about the filament axis, is shown in Fig. 3. Shown also is the torsional or shear modulus, G, of copper. It is clear that the temperature behaviour of $2/(S_{44} + S_{55})$ differs from that of E_{33}, and that its relationship to the torsional modulus of copper is nearly the same as the relationship of E_{33} to the Young's modulus of copper. The dashed part of the curve is an extrapolation based on the usual behaviour of elastic constants at low temperatures and the behaviour of the elastic constants of this composite that were measured to 4 K. The extrapolation represents probable behaviour based on available data, but other behaviour is possible.

The Poisson ratios that relate the strain along the filament axis (produced by a stress along that axis) to the strains perpendicular to the axis were found to be 0.366 and 0.349 along the x and y axes respectively, at room temperature.[1] The temperature dependences of these ratios are not easily measured by dynamic techniques, and they were not measured in this study. However, since Poisson's ratio for copper decreases by two percent on cooling from 300 to 4 K, a similar change would be expected for the composite's Poisson's ratio.

The elastic stiffness coefficients, the C_{ij}'s, are given in Table 1. Although C_{11}, C_{22} and C_{33} were all measured, the data for C_{22} practically coincide with those for C_{33}, so only C_{11} and C_{33}, normalized separately to their 300 K values are shown in Fig. 4 together with the longitudinal modulus, C_l, of copper. The dashed curves are extrapolations. Again, these

Table 1. Elastic constants of an NbTi/Cu composite and polycrystalline copper at selected temperatures in units of 10^{11} N/m², except ν, which is dimensionless; numbers in parentheses are based on extrapolated data

	300 K	200 K	100 K	0 K
NbTi/Cu composite:				
E_{33}	1.138	1.189	1.238	1.287
$G_{\parallel}$	0.417	0.427	0.445	(0.454)
ν_{31}	0.365	–	–	–
ν_{32}	0.349	–	–	–
C_{11}	1.834	1.865	1.908	(1.915)
C_{22}	1.878	1.911	1.952	(1.957)
C_{33}	1.880	1.919	1.965	(1.983)
C_{55}	0.407	0.418	0.436	(0.442)
C_{66}	0.414	0.425	0.442	0.456
Polycrystalline copper[a]:				
E	1.282	1.329	1.369	1.386
G	0.477	0.496	0.512	0.519
ν	0.344	0.341	0.339	0.338
C_l	2.006	2.053	2.093	2.111
C_t	0.477	0.495	0.511	0.518

[a] Reference 6, single crystal data converted using arithmetic average of Hashin-Shtrikman bounds

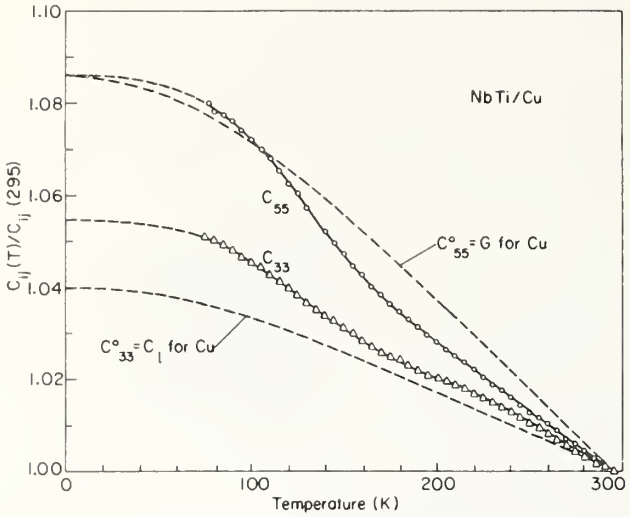

Fig. 4 The temperature variation of the longitudinal elastic stiffnesses of an NbTi/Cu composite in the [100] and [001] directions compared with the temperature dependence of longitudinal elastic modulus of polycrystalline copper

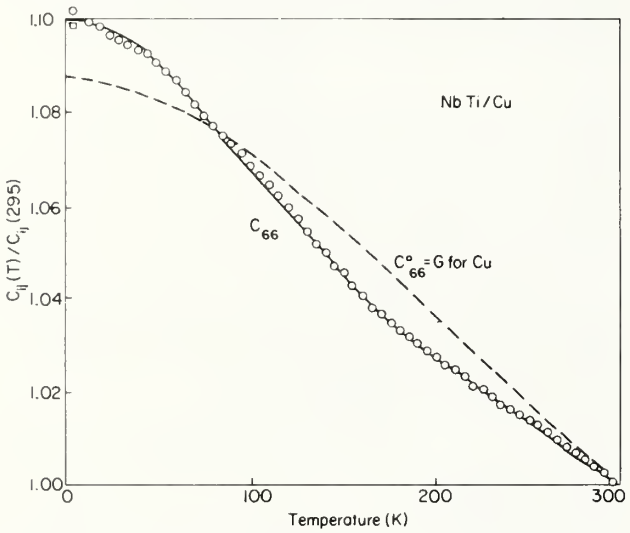

Fig. 5 The temperature dependence of the shear modulus of an NbTi/Cu composite compared to the behaviour of the shear modulus of polycrystalline copper; C_{66} corresponds to the shear resistance on a (100) plane in a [010] direction, or a (010) plane in a [100] direction

elastic constants are about seven percent lower than those of copper, and they increase about five percent on cooling. As in the case of the practical elastic constants, irregularities in the C_{ij}'s are observed during cooling.

The temperature dependence of C_{66}, normalized to 300 K, is shown in Fig. 5. C_{55} was measured between 300 and 76 K; the resulting data nearly coincide with those for C_{66} and they are not shown. C_{55} and C_{66} for the composite are about 14% lower than the value for copper, and they increase about 10% on cooling. They also exhibit irregular temperature behaviour. The datum point shown as an open square at 4 K in Fig. 5 represents an absolute, rather than a relative, elastic constant measurement; it confirms the overall elastic constant change due to cooling.

C_{33} and C_{55}, a longitudinal and a transverse stiffness of the composite material, are shown in Fig. 6 together with C_l, and C_t, the longitudinal and transverse moduli of polycrystalline copper. In both copper and the composite, the transverse (shear) moduli have stronger temperature dependences than the longitudinal moduli. Surprisingly, the temperature dependences of both the transverse and longitudinal moduli of the composite are between those of the two copper moduli. Based on simple rule-of-mixture arguments it follows from Fig. 6 that the shear modulus of NbTi must increase with decreasing temperature in a way similar to that of copper, but the longitudinal modulus of NbTi must increase considerably more than that of copper if stress effects from differential thermal contraction are small.

DISCUSSION

In a previous study,[1] it was shown that the room temperature elastic constants of an Nb Ti/Cu composite can be predicted approximately from a rule of mixtures from the known elastic constants of copper and NbTi. It was also shown that the observed values of the practical elastic constants E_{33} and $2/(S_{44}+S_{55})$ were consistent with the measured values of the elastic stiffnesses, the C_{ij}'s.

Rules of mixtures could not be used to predict the temperature dependence of the composite material studied here because the temperature dependences of the elastic constants of the NbTi alloy have not been reported. An attempt to obtain such data failed.[7]

Weston[8] reported the temperature dependences of the elastic constants fo an NbTi/Cu fibreglass/epoxy coil composite. Although that composite included fibreglass and epoxy, the temperature dependence of its elastic constants reflects that of NbTi/Cu because the stiffness of the fibreglass epoxy is low and it constitutes only about one quarter of the total volume. The sign and magnitude of the temperature dependences observed by Weston were about the same as those reported here. For most of the elastic constants, Weston reported very small deviations from the usual temperature behaviour of ordinary materials, but, in the Young's modulus along the filaments, Weston found a large deviation from usual temperature behaviour. However, none of the elastic constants of the coil composite studied by Weston showed the type of irregularities observed in the present study.

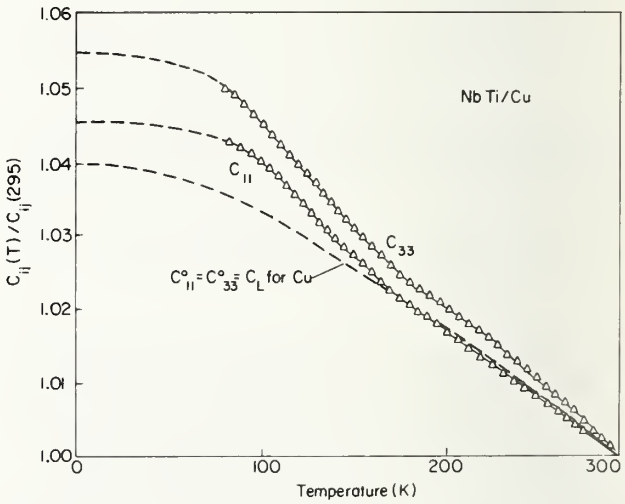

Fig. 6 Comparison of a longitudinal and a shear elastic constant of the composite; C_{33} is measured in the [001] direction, along the filament axis; C_{55} corresponds to the shear resistance on a (100) plane in a [001] direction or of a (001) plane in a [001] direction; values for copper are s'.own for comparison

The observed increase in all the elastic stiffnesses of about ten percent on cooling from 295 K to 4 K is expected for this material. Elastic constants of most metals increase between five and fifteen percent on cooling to zero temperature;[9] the polycrystalline longitudinal modulus C_1 of copper increases four percent on cooling.

As shown in Figs 2–6, all the measured elastic constants reported here have irregular temperature dependences compared to copper. Experimental evidence for these irregularities is strong: they occur in seven different measured elastic constants; they were observed on measurements made during both heating and cooling; and they occurred in repeated experiments. These irregularities are probably insignificant from the viewpoint of engineering design because of the relatively small deviations from regular behaviour.

The cause of these irregularities is uncertain. Two hypotheses can be suggested. First, since elastic constants are changed by stress, the irregularities may arise from internal stress changes due to differential thermal contraction during cooling. Second, the irregularities may arise from similar irregularities in the temperature dependences of the elastic constants of the NbTi filaments. Similar irregularities have been observed in niobium and in other transition metals, where they are ascribed to the electronic structure,[10, 11] and in a niobium/zirconium alloy, where they are attributed to the formation of omega phase.[12]

CONCLUSIONS

The following principal results and conclusions emerge from the present study. The Young's modulus along the filaments, E_{33}, increases 12% on cooling from 300 to 4 K, compared to 8% for copper. The extrapolated torsional modulus around the filaments, $G_{\parallel}$, increases 9% on cooling, the same as copper. The extrapolated elastic stiffnesses C_{11}, C_{22} and C_{33} increase by 5% on cooling, compared to 4% for copper. The shear elastic constants C_{55} and C_{66} increase 10% on cooling, compared to 9% for copper. All measured elastic constants have irregular temperature dependences.

ACKNOWLEDGEMENTS

This study was supported by the Advanced Research Projects Agency of the US Department of Defense. Dr D.A. Colling of Magnetic Corporation of America, the manufacturer of the composite, made valuable comments on the manuscript.

References

1 **Ledbetter, H.M. and Read, D.T.** *J Appl Phys* (in press)
2 **Critchlow, P.R., Gregory, E. and Zeitlin, B.** *Cryogenics* **11** (1971) pp 3–10
3 **Naimon, E.R., Weston, W.F. and Ledbetter, H.M.** *Cryogenics* **14** (1974) pp 246–249
4 **Marx, J.** *J Sci Instrum* **22** (1951) pp 503–509
5 **Whitney, J.M.** *Textile Res J* **36** (1966) p 765
6 **Overton, W.C. and Gaffney, J.** *Phys Rev* **98** (1955) pp 969–977
7 **Reid, C.N., Routbort, J.L. and Maynard, R.A.** *J Appl Phys* **44** (1973) pp 1398–1399
8 **Weston, W.F.** *J Appl Phys* **46** (1975) pp 4458–4465
9 **Hearmon, R.F.S.** in *Numerical data and functional relationships in science and technology, Group III, vol 1,* edited by K.H. Hellwege and A.M. Hellwege (Springer-Verlag, Berlin, 1969)
10 **Carroll, K.J.** *J Appl Phys* **36** (1965) pp 3689–3690
11 **Featherston, F.H. and Neighbors, J.R.** *Phys Rev* **130** (1963) pp 1324–1333
12 **Goasdue, C., Ho, P.S. and Sass, S.L.** *Acta Met* **20** (1972) pp 725–733

NBS-114A (REV. 9-78)

U.S. DEPT. OF COMM. BIBLIOGRAPHIC DATA SHEET	1. PUBLICATION OR REPORT NO. NBSIR 80-1633	2. Gov't. Accession No.	3. Recipient's Accession No.

4. TITLE AND SUBTITLE

Material Studies for Superconducting Machinery Coil Composites

5. Publication Date

June 1980

6. Performing Organization Code

7. AUTHOR(S)

J. W. Ekin, M. B. Kasen, D. T. Read, R. E. Schramm, R. L. Tobler, and A. F. Clark

8. Performing Organ. Report No.

9. PERFORMING ORGANIZATION NAME AND ADDRESS

NATIONAL BUREAU OF STANDARDS
DEPARTMENT OF COMMERCE
WASHINGTON, DC 20234

10. Project/Task/Work Unit No.

11. Contract/Grant No.

12. SPONSORING ORGANIZATION NAME AND COMPLETE ADDRESS *(Street, City, State, ZIP)*

Annapolis Laboratory
David W. Taylor Naval Ship Research & Development Center
Annapolis, Maryland 21402

13. Type of Report & Period Covered

14. Sponsoring Agency Code

15. SUPPLEMENTARY NOTES

☐ Document describes a computer program; SF-185, FIPS Software Summary, is attached.

16. ABSTRACT *(A 200-word or less factual summary of most significant information. If document includes a significant bibliography or literature survey, mention it here.)*

The physical properties of a superconducting coil composite are studied to accurately predict the coil behavior under operating conditions. Emphasized in this third interim report are studies on the effect of stress and strain on the critical current of superconducting wires. The report also includes data on several fiberglass/epoxy support structures for the coil and its dewar. Preliminary results are also given for the effect of stress on small superconducting composite rings used to model the full sized coil behavior. A summary of the program results to date is included.

17. KEY WORDS *(six to twelve entries; alphabetical order; capitalize only the first letter of the first key word unless a proper name; separated by semicolons)*

Critical current; fiberglass/epoxy composite; mechanical properties; niobium-tin; niobium-titanium; strain; superconducting coil composite; superconducting wire.

18. AVAILABILITY

☒ Unlimited

☐ For Official Distribution. Do Not Release to NTIS

☐ Order From Sup. of Doc., U.S. Government Printing Office, Washington, DC 20402, SD Stock No. SN003-003-

☒ Order From National Technical Information Service (NTIS), Springfield, VA. 22161

19. SECURITY CLASS (THIS REPORT)

UNCLASSIFIED

21. NO. OF PRINTED PAGES

164

20. SECURITY CLASS (THIS PAGE)

UNCLASSIFIED

22. Price

$11.00

USCOMM-DC

☆ U. S. GOVERNMENT PRINTING OFFICE 1980 - 677-096/1253 Reg. 8